UCL Chemical Engineering Doctoral Thesis

Thermal Investigations of Electrochemical Devices

James B. Robinson

2016

A thesis submitted for the partial fulfilment of the
requirements for the degree of Doctor of Philosophy
at University College London

Department of Chemical Engineering
University College London
Torrington Place
London
WC1E 7JE

I, James Brendan Robinson, confirm that the work presented in this thesis is my own.

Where information has been derived from other sources, I confirm that this has been indicated in the thesis.

_____   _____
Signature   Date

Abstract

Electrochemical devices are amongst the most promising systems for renewable and clean energy; despite this there are a number of challenges which have both hindered widespread commercialisation and resulted in safety concerns. Common amongst all electrochemical devices is the importance of temperature and thermal management. Here, the thermal properties of components and devices are examined using infrared thermal imaging, and complimentary techniques, to improve both the fundamental understanding and safety of a number of electrochemical systems, with a focus on fuel cells and batteries.

A study investigating the stress distribution in solid oxide fuel cell anodes under imposed non-uniform temperature conditions is described, highlighting the potential for combining infrared imaging with complimentary techniques; in this instance, X-ray diffraction. This study is expanded to show the potential impact of the results on finite element analysis.

Thermal imaging is combined with X-ray microtomography in order to describe the surface temperature effects associated with discharging a cylindrical Li-ion battery. Here the internal structure of the cell is seen to have a major impact on the temperature variation observed.

Advanced thermal imaging techniques are described with a diagnostic entitled electro-thermal impedance spectroscopy, in addition to the first reported use of lock-in thermography on a Li-ion battery.

The impact of the work is highlighted, where appropriate detailing the potential incorporation of the diagnostic and experimental techniques in novel areas, whilst also considering the relevance to existing methodologies and mechanisms.

Acknowledgments

I would firstly like to thank Prof. Dan Brett for providing me with the opportunity to study within UCL and allowing me enough academic freedom to discover a plethora of techniques, technologies and curiosities. I must also express sincere gratitude to Dr. Paul Shearing for giving me the chance to conduct the experiments at Diamond, in addition to facilitating a large number of the collaborative efforts I have been able to partake in.

For their assistance before, during and after the experiments conducted at Diamond, I would like to acknowledge Dr. Christina Reinhard, Prof. Peter Lee, Dr. Ralph Clague and Dr. David Eastwood, who has also provided assistance in the tomographic work in this thesis. Thanks too must go to Jay, Tom and Toby for their help in designing the furnace used in the 'Diamond work'. I would also like to thank all the members of the EIL with whom I have collaborated particularly Quentin, Mozhdeh and Ishanka.

To the guys I grew up with I'm looking forward to seeing you in the Orchard soon. To all my family especially my parents and Ian - thanks for all the help and encouragement.

Dave, Erik, Rhod, Vidal, Tom, Donal, Dami, Len and Phil, the nights spent discussing science have been some of the most enjoyable times I've had – the mornings less so; despite this it would not have been half as fun without you all, so cheers for the laughs!

All back home who've helped me get to this point are also due particular thanks, especially those I met at UCD who provided me with the basics to successfully submit a thesis – both scientifically and otherwise.

Publications and Presentations

Primary Research Papers

Robinson J.B., Darr, J.A., Eastwood D.S., Hinds G., Lee P.D., Shearing P.R., Taiwo O.O., Brett D.J.L., Non-uniform temperature distribution in Li-ion batteries during discharge – A combined thermal imaging, X-ray micro-tomography and electrochemical impedance approach, J. Power Sources, 252, 2014, pp. 51-57

Robinson J.B., Brown L.D., Jervis J.R., Taiwo O.O., Millichamp J., Mason T., Neville T., Eastwood D.S., Reinhard C., Lee P.D., Brett D.J.L., Shearing P.R., A novel high temperature furnace for combined in situ synchrotron radiation X-ray diffraction and infrared thermal imaging to investigate the effects of thermal gradients upon the structure of ceramic materials, J. Synch. Rad., 21 (5), 2014, pp. 1134-1139

Robinson J.B., Brown L.D., Jervis J.R., Taiwo O.O., Heenan T.M.M., Millichamp J., Mason T., Neville T., Eastwood D.S., Reinhard C., Lee P.D., Brett D.J.L., Shearing P.R, The Effect of Thermal Gradients on Stress in Solid Oxide Fuel Cell Anodes, J. Power Sources, 288, 2015, pp. 473-481

Robinson J.B., Engebretsen E., Brown L.D., Clague R., Eastwood D.S., Reinhard C., Lee P.D., Brett D.J.L., Shearing P.R, Thermal Gradients in Solid Oxide Fuel Cell Anodes: X-Ray Diffraction, Thermal Imaging and Model Prediction, ECS Trans., 68 (1), 2015, pp. 1053-1067

Robinson J.B., Engebretsen E., Finegan D.P., Hinds G., Shearing P.R., Brett D.J.L., Detection of Internal Defects in Lithium-Ion

Batteries Using Lock-In Thermography, ECS Electrochem. Letters, 4 (9), 2015, pp. A106-A109

Robinson J.B., Shearing P.R., Brett D.J.L., Thermal Imaging of Electrochemical Power Systems: A Review, J. Imaging, 2 (2), 2016

Other Research Papers

Noorkami M., Robinson J.B., Meyer Q., Obeisun O.A., Fraga E.S., Reisch T., Shearing P.R., Brett D.J.L., Effect of temperature uncertainty on polymer electrolyte fuel cell performance, Int. J. Hydrogen Energy, 39 (3), 2014, pp. 1439-1448

Dedigama I., Angeli P., Ayers K., Robinson J.B., Shearing P.R., Tsaoulidis D., Brett D.J.L, In situ diagnostic techniques for characterisation of polymer electrolyte membrane water electrolysers – Flow visualisation and electrochemical impedance spectroscopy, Int. J. Hydrogen Energy, 39 (9), 2014, pp. 4468-4482

Meyer Q., Ashton S., Curnick O., Reisch T., Adcock P., Ronaszegi K., Robinson J.B., Brett D.J.L., Dead-ended anode polymer electrolyte fuel cell stack operation using electrochemical impedance spectroscopy, off-gas analysis and thermal imaging, J. Power Sources,, 254, 2014, pp. 1-9

Obeisun O.A., Meyer Q., Robinson J.B., Gibbs C.W., Kucernak A.R., Shearing P.R., Brett D.J.L., Development of Open-Cathode Polymer Electrolyte Fuel Cells Using Printed Circuit Board Flow-Field Plates: Flow Geometry Characterisation, Int. J. Hydrogen Energy, 39 (32), 2014 pp. 18326-18336

Obeisun O.A., Meyer Q., Robinson J.B., Gibbs C.W., Kucernak A.R., Shearing P.R., Brett D.J.L., Advanced Diagnostics Applied to a Self-Breathing Fuel Cell Using Printed Circuit Board Technology, ECS Transactions, 61 (27), pp. 249-258

Finegan D.P., Scheel M., Robinson J.B., Tjaden B., Hunt I., Di Michiel M., Offer G.J., Hinds G., Brett D.J.L., Shearing P.R., In-

operando high-speed tomography of lithium-ion batteries during thermal runaway, Nature Comms., 6 (6924), 2015

Meyer Q., Ronaszegi K., Robinson J.B., Noorkami M., Curnick O., Ashton S., Danelyan A., Reisch T., Adcock P., Kraume R., Shearing P.R., Brett D.J.L., Combined current and temperature mapping in an air-cooled, open cathode polymer electrolyte fuel cell under steady-state and dynamic conditions, J. Power Sources, 297, 2015, pp. 315-322

Obeisun O.A., Meyer Q., Engebretsen E., Finegan D.P., Robinson J.B., Hinds G., Shearing P.R., Brett D.J.L., Study of water accumulation dynamics in the channels of an open-cathode fuel cell through electro-thermal characterisation and droplet visualisation. Int. J. Hydrogen Energy, 40 (46), 2015, pp, 16786-16976

Engebretsen E.C., Obeisun O.A., Robinson J.B., Mason T., Finegan D., Shearing P.R., Barrass S., Hinds G., Brett D.J.L., Electrothermal impedance spectroscopy applied to an open-cathode polymer electrolyte fuel cell, J. Power Sources, 302, 2015, pp. 210-214

Finegan D.P., Tudicso E., Scheel M., Robinson J.B, Taiwo O.O., Eastwood D., Lee P.D., Di Michel M., Bay B., Hall S., Hinds G., Brett D.J.L., Shearing P.R., Quantifying bulk electrode strain and material displacement within commercial lithium batteries via high-speed *operando* tomography and digital volume correlation, Advanced Science, 3 (3), 2016

Research & Public Engagement Awards

2013 – Robinson J.B., Finegan D.P., Fast tomographic imaging of lithium ion batteries, The STFC Futures Early Career Award, (shared)

2014 – UCell – UCL Fuel Cells, 'Green Futures', The STFC Futures Early Career Award, (shared)

2015 – Rooke Scholarship, UCL Department of Chemical Engineering

Conference Presentations

Robinson J.B., Shearing P.R., Brett D.J.L., Combined Thermal Imaging and X-ray Diffraction of Solid Oxide Fuel Cells at Operating Temperature with Thermal Gradients, The Hydrogen and Fuel Cell Researcher Conference, H2FC SuperGEN, University of Birmingham, 2013

Robinson J.B., Shearing P.R., Brett D.J.L., Investigating the Effect of Thermal Gradients on Stress in SOFC Anodes Using Combined Synchrotron Radiation and Thermal Imaging, STFC Early Career Researchers Conference, The Coseners House, 2015

Robinson J.B., Engebretsen E., Brown L.D., Clague R., Eastwood D.S., Reinhard C., Lee P.D., Brett D.J.L., Shearing P.R, Thermal Gradients in Solid Oxide Fuel Cell Anodes: X-Ray Diffraction, Thermal Imaging and Model Prediction, ECS with SOFC XIV, Glasgow, 2015

Table of Contents

List of Figures

List of Tables

List of Equations

Research Aims, Motivation and Challenges

Despite the increasing adoption of electrochemical power systems, the challenges associated with the development of sustainable, economic and safe technologies are myriad. A key parameter to ensure all of the above criteria are met is the thermal performance of the relevant system; whether through optimisation of performance or failure mitigation, the understanding of the temperature transients and distributions in electrochemical power systems is of paramount importance in designing and producing systems. Furthermore, understanding the implications of these thermal effects on the structural or mechanical integrity of individual cells or systems can aid the development of sustainable technologies. Clearly with such wide scope and research opportunities this thesis cannot adequately cover the entire field; rather it is divided into relevant self-contained studies which serve to build upon the previously reported work in the area and lay the foundations for future work. In order to serve as a guide to the reader the chapters which follow are outlined below.

Chapter one is intended as an introduction to the fundamentals of electrochemical power systems; this chapter also introduces the concept of infrared thermography in some detail. A subsequent literature survey in chapter two assesses the current state of the art in the field of thermography with respect to electrochemical power

systems, highlighting the seminal works upon which the research outlined in this thesis has built.

Chapter three discusses the experimental methodology utilised when conducting the experiments reported here. As the experimental conditions varied depending on the temperature and indeed location of the research being conducted this chapter is intended to give the fundamentals of operating and framing a thermal imaging camera; with a particular focus on the importance of correctly calculating accurate emissivity values in order to obtain absolute temperature values. X-ray and focussed ion beam techniques which have been used in producing this thesis are discussed, with the fundamentals of electrochemical impedance spectroscopy also detailed.

Chapter four discusses a study of Li-ion batteries which investigates temperature variations inherent in a cell due to the design. The thermal imaging results are supplemented with electrochemical impedance spectroscopy and X-ray microtomography to show the results are not the result of cell failure and therefore must be considered when designing multi-cell battery packs and thermal management systems.

Chapter five focusses upon experiments designed to investigate the effect of temperature variation on solid oxide fuel cell anodes. The

chapter initially describes the design of the experiment, including a novel furnace, before the results are discussed. A subsequent finite element analysis is performed to highlight the results and demonstrate the potential impact of the work in cell design.

Chapter six highlights the first reported use of lock-in thermography in Li-ion cells which enables internal defects, in this case pockets of gas generated from degraded electrolyte, to be detected using thermal imaging techniques.

Chapter seven discusses the use of frequency domain measurements to investigate responses in Li-ion cells in the context of an emerging area known as electrothermal impedance spectroscopy.

Finally, Chapter eight summarises the results detailed in this thesis while chapter nine discusses the potential for future work in the field, highlighting research opportunities for novel experiments building on the work conducted in this thesis and suggesting potential avenues which may yield interesting results.

The overall aim of the thesis as outlined in the chapters detailed above is to demonstrate the effective gains that can be (and indeed have been) made through the utilisation of infrared imaging as a tool

to understand thermal variations. Additionally this thesis demonstrates the applicability of coupling infrared imaging with complimentary techniques to understand in greater depth not only the effect of phenomena but also the root causes.

The thesis has been structured to highlight these coupled experiments by first describing *ex-situ* analysis of Li-ion batteries in the form of electrochemical impedance spectroscopy and computed tomography before describing sequential analysis of fuel cells using X-ray diffraction and thermal imaging. The final results chapters describe *in operando* experiments using advanced mathematical concepts to evaluate the potential of infrared imaging as a diagnostic tool to understand the failure of cells and as a tool to inform potential safety strategies pertaining to Li-ion cells.

1 Introduction

The last century has seen a tremendous rise in global population, increase in worldwide industrialisation and significant technological advancement; however, in order to sustain these developments it is imperative to identify, improve and commercialise new, high efficiency, clean power systems. Atmospheric CO_2 trends, as measured at the Mauna Loa observatory for example, have seen an increase of over 25% in the last fifty years alone – which is indicative of global climate change, widely attributed to the burning of fossil fuels associated with both transport and grid scale power generation. In an effort to mitigate against these effects governmental limits on CO_2 emissions have been enshrined in law, providing a pathway for novel technology to replace the historically dominant fossil fuel dominated power generation systems. This has been further exacerbated in recent times by increasingly volatile fossil fuel prices and concerns over energy security. Additionally, the miniaturisation of technology has increased the requirement for compact power systems to power increasingly energy intensive devices.

These driving factors have dramatically increased the research into electrochemical power systems, which are both highly efficient and environmentally friendly. These devices, which include power generation in the form of fuel cells and power storage via battery technology and electrolysis, have recently been implemented in

commercial systems. Li-ion batteries were amongst the first widely commercialised systems with rapid development in the technology enabling the incorporation of systems in portable devices such as laptop computers and mobile phones. Recent developments have seen both Li-ion cells and low temperature fuel cells entering the automotive market powering both fully electric and hybridised vehicles; examples of which include Tesla's fleet of battery electric vehicles and the 2015 release of the Toyota Mirai which is powered using polymer electrolyte membrane fuel cells (PEMFCs). Portable power generation has also seen commercialisation through a number of hydrogen powered mobile phone rechargers developed by Horizon (China) and Intelligent Energy (UK). Domestic power generation has also seen developments in fuel cell technology with both PEMFC and solid oxide fuel cell (SOFC) technology being deployed in combined heat and power (CHP) systems across the world. This localised strategy enables the efficiency of power and heat generation to be increased from 40–50% to in excess of 80% [1].

Despite the successes in commercialisation highlighted above there is still significant scope for improvement in both the fundamental understanding and engineering of these devices. Temperature plays a key role in increasing the efficiency, safety and long term stability of electrochemical power systems and as such is an area which has been intensively studied. Despite this, much of the research has

been limited spatially, through the use of single or multiple thermocouples, or hampered by difficulty in gaining access to sufficient information to fully quantify the dynamics of the processes occurring within these systems. This thesis aims to improve the understanding of the thermal behaviour of electrochemical power systems, whilst also employing thermal techniques to both improve the fundamental understanding of the devices and develop novel methodologies to enable the *in situ* monitoring of systems. Through this work it is hoped that the widespread commercialisation of electrochemical devices can be aided; improving the safety, efficiency and viability of these technologies.

1.1 Electrochemical Power Systems

Electrochemical power systems are used in a wide range of sustainable power generation and storage applications due to the high electrical efficiencies and low carbon emissions which typify such devices. Broadly, these power systems can be divided into fuel cells and batteries; however, these assignments encompass a significantly larger subset of classifications governed by the materials of construction, operating temperature and the fundamental mechanisms which generate electricity. Common to all electrochemical power devices is the fact that chemical energy is converted directly to electrical energy, negating the intermediate mechanical and thermal steps required by conventional combustion

techniques. This direct conversion ensures that the efficiency of electrochemical power systems is not limited by the Carnot cycle [2] and also governs the mechanisms of energy loss within the cells. Rather than a combination of thermal, kinetic and acoustic energy, electrochemical power systems dissipate waste energy primarily via thermal mechanisms. This review will focus primarily on Li-ion batteries (LIB) and on polymer electrolyte membrane (PEMFC) and solid oxide fuel cells (SOFC); allowing the description of the most commonly studied electrochemical devices within two distinct temperature windows – temperatures below 120 °C for both LIB and PEMFC and those above 600 °C for SOFC. The reason for these temperature windows is different in all cases; for instance, the 600 °C lower limit is imposed due to the poor ionic conductivity of the solid ceramic electrolytes typically used in SOFCs [3, 4]. However, in the case of LIBs, exceeding this temperature limit can result in cell decomposition [5-8] which can in turn lead to catastrophic failure of the devices [9-11]. The importance of temperature for operational and safety reasons on both fuel cells and batteries can be seen in the varied and abundant literature produced to model the thermal characteristics and behaviour of these devices, in addition to an ever increasing quantity of experimental reports. These models, which range from simple one-dimensional thermal models to highly complex three-dimensional coupled thermal and electrochemical analyses, show that irrespective of device, non-uniform temperature

distributions can be present during operation; often resulting in operational issues for the devices in question. This review will attempt to outline the key works describing the use of thermal imaging, whilst also outlining potential opportunities for further work in this area.

1.1.1 Fuel Cells

Fuel cells are a widely researched energy conversion device first developed in the mid-19th century by Sir William Grove [12] and can be distinguished from batteries as they require a continuous flow of fuel through the cell. These devices generate electricity by facilitating electrochemical reactions; at one electrode a stream is reduced, and a second stream is oxidised at the other electrode. The reaction, which occurs within regions known as triple phase boundaries at these electrodes [13], is dependent upon the type of fuel cell operated. Between the two electrodes, the anode and cathode, is an electrolyte which promotes the passage of ions formed during the reaction. This configuration is common to all fuel cell types, which are distinguished by the materials used in the construction of a cell, a choice determined by the operating temperature of a cell and the fuel source being utilised.

Fuel cells can be broadly categorised into two classes based upon their operating temperature; low temperature fuel cells which operate

below 200 °C and high temperature fuel cells whose operating temperature can exceed 1000 °C. A summary of the types of fuel cells and their respective operating temperatures is shown in Table 1. Due to the wide range of operating temperatures, the method of thermal management can vary; however, in all cases the importance of a uniform and repeatable temperature distribution is paramount to avoid cell degradation and failure.

Table 1 Types of fuel cell adapted from [12].

	PEMFC	PAFC	AFC	MCFC	SOFC
Electrolyte	Nafion	H_3PO_4	KOH	Molten Carbonate	Ceramic
Charge Carrier	H^+	H^+	OH^-	CO_3^{2-}	O^{2-}
Operating Temperature	80 °C	200 °C	>220 °C	650 °C	600-1000 °C
Fuels used	H_2, MeOH	H_2	H_2	H_2, CH_4	H_2, CH_4, CO
Electrical Efficiency (LHV)	40–50%	40–50%	50–55%	50–60%	50–60%
Applications	Portable Electronic, Space	Stationary Power	Space, Defence	Stationary Power, Heat Generation	Stationary Power, Heat Generation

A fuel cell is subject to a range of polarisations (or overpotentials) during its operation which manifest as heat given off the system. These polarisations are well defined and widely available in a range of textbooks and literature and, as such, only a brief summary will be provided here. The polarisations are all dependent upon the current

drawn from the cell at a given time and are often shown by a polarisation curve which shows how the operating voltage changes with current (or current density). A typical polarisation curve is shown in Figure 1 developed using a fundamental one-dimensional PEMFC model outlined by O'Hayre [12].
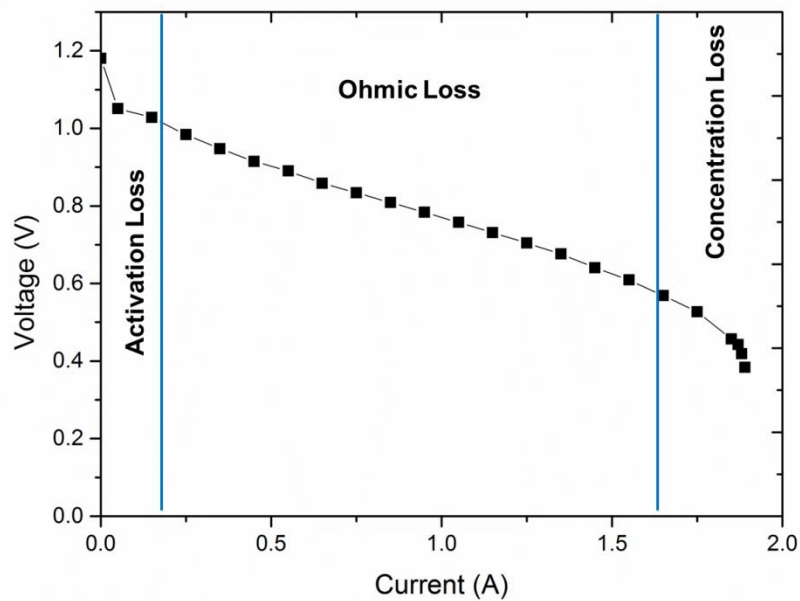
Figure 1 - Typical polarisation curve for a PEMFC highlighting the activation, Ohmic and concentration loss regions.

This curve is a measure of the deviation from the thermodynamic voltage available from a given electrochemical reaction; for instance, the traditional hydrogen-oxygen reaction common throughout the history of fuel cell research.

$$H_2 + \frac{1}{2}O_2 \leftrightarrow H_2O$$
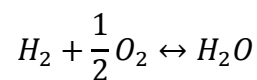
(1) Hydrogen–Oxygen Reaction Equation

This reaction is composed of two half-cell reactions, namely the hydrogen oxidation reaction (HOR) and the oxygen reduction reaction (ORR).

$$H_2 \leftrightarrow 2H^+ + 2e^-$$
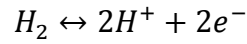
(2) Hydrogen Oxidation Reaction

$$\frac{1}{2}O_2 + 2H^+ + 2e^- \leftrightarrow H_2O$$
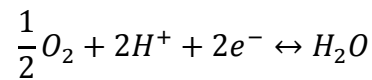
(3) Oxygen Reduction Reaction

The thermodynamic or open circuit voltage (E_{OCV}) for this reaction is given by the Nernst equation, which accounts for operating conditions such as fuel and oxidant inlet concentration (a^{v_i}) and operating temperature (T) and is shown in Equation 4, where E^0 represents the theoretical voltage of the reaction, R refers to the universal gas constant, $\dot{n}_e$ the number of electrons involved in the reaction and F is Faraday's constant.

$$E_{OCV} = E^0 - \frac{RT}{\dot{n}_e F} ln \frac{\prod a_{products}^{v_i}}{\prod a_{reactants}^{v_i}}$$

(4) Nernst Equation

The thermodynamic voltage available from a fuel cell is dependent upon a range of factors including the fuel utilised, temperature of operation and the stoichiometry and utilisation of the reactants provided. Assuming constant operating conditions (and non-deteriorating structural components), the drop in voltage seen in Figure 3 is attributable to a number of polarisations based upon three

regions on the polarisation curve: the activation polarisation (η_{act}),
Ohmic polarisation (η_{Ohmic}) and concentration polarisation (η_{conc}).
Knowing these losses at a given operating current and the open
circuit voltage (E_{OCV}) the operating voltage of a cell can be calculated
according to Equation 5.

$$E(i) = E_{OCV} - \eta_{act} - \eta_{Ohmic} - \eta_{conc}$$

(5) Effective Voltage including Polarisation Losses

These polarisations can be subdivided into those which occur at the
electrodes of the device, the anode and the cathode respectively,
and within the electrolyte.

The activation polarisation is a voltage loss brought about during the
start-up phase of operation with a fuel cell. The activation polarisation
is typically assigned to both the cathode and anode in SOFC
modelling [14], while when considering PEM fuel cells the activation
polarisation is typically governed by the kinetics of the ORR [15]. The
activation polarisation is normally modelled using the Butler-Volmer
equation shown below.

$$i = i_0 \left[exp\left(\frac{\alpha_{rct} \dot{n}_e F \eta_{act}}{RT} \right) - exp\left(\frac{-(1 - \alpha_{rct}) \dot{n}_e F \eta_{act}}{RT} \right) \right]$$

(6) Butler–Volmer Equation

The structure of the equation is such that there is both a forward and
reverse reaction rate describing the reduction and oxidation reaction

respectively with the reactant charge transfer coefficient (α_{rct}) governing the magnitude of the activation polarisation.

The activation polarisation can be further modelled using a number of simplifications. At low current densities it is often assumed that the activation overpotential is a linear function of the current drawn. However, as further current is drawn this model begins to break down. If it is assumed that the magnitude of the activation polarisation is significantly higher at one of the electrodes a logarithmic model known as the Tafel equation can be used; this is shown in Equation 7 [16].

$$\eta_{act} = \frac{RT}{\alpha_{rct}F} ln\left(\frac{i}{i_0}\right)$$

(7) Activation losses occurring within a fuel cell system as described by the Tafel equation

In the special case that the rates of the oxidation and reduction reaction are equal (given by α_{rct}=0.5) a hyperbolic function is used to describe the activation polarisation.

$$i = 2i_0 \, sinh\left(\frac{\dot{n}_e F \eta_{act}}{2RT}\right)$$

(8) Modified Butler–Volmer Reaction for the case α=0.5

Given the structure of the equations above, it is clear that the operating temperature has a significant impact upon the loss incurred at a given current. It must be noted that due to the number of constants included in each of the equations (i_0, α_{rct}, n, F, R), the

temperature and operating current are the only variables which can be controlled to minimise the activation polarisation; in addition, the exchange current; given by i_0 in Equations 7 and 8 is also temperature dependent and is modelled using an Arrhenius type equation [17]. The exchange current density; given by the current present at an electrode under open circuit conditions, is a key factor in the development of novel fuel cell catalysts as it is inherent to a given electrode.

Ohmic polarisation is caused by a resistance to the flow of the ions generated at the relevant electrode of fuel cells. Ohmic polarisation is largely dictated by losses through the electrolyte with a small percentage of the Ohmic polarisation contributed by the anode and cathode. The Ohmic polarisation of any cell is therefore, in the main, a function of the material used for the electrolyte, temperature and the thickness achieved during fabrication. A typical model for the Ohmic resistance (R) of a cell is given in Equation 9 taken from Leah *et al.* [18]. From the structure of the equation it is evident that in addition to a constant resistance the thickness (τ) and the ionic conductivity (σ) of the electrolyte play a role in the operational Ohmic resistance observed.

$$R_{ohm} = \frac{\tau_{electrolyte}}{\sigma_{electrolyte}} + R_{constant}$$

(9) Model for Ohmic Resistance in a Fuel Cell

Ohmic polarisation (η_{ohmic}) is given by the product of the Ohmic resistance and the magnitude of the current (i) being drawn from the cell, as shown below.

$$\eta_{ohmic} = iR_{ohm}$$

(10) Ohmic Polarisation in a Fuel Cell

Due to the structure of Equation 10 it is evident that an increase in current (or current density) will result in increased Ohmic polarisations. Additionally, the above equations contain a temperature dependence in the form of the electrical conductivity (σ); this dependence on temperature is highlighted for two SOFC electrolytes in Figure 2.
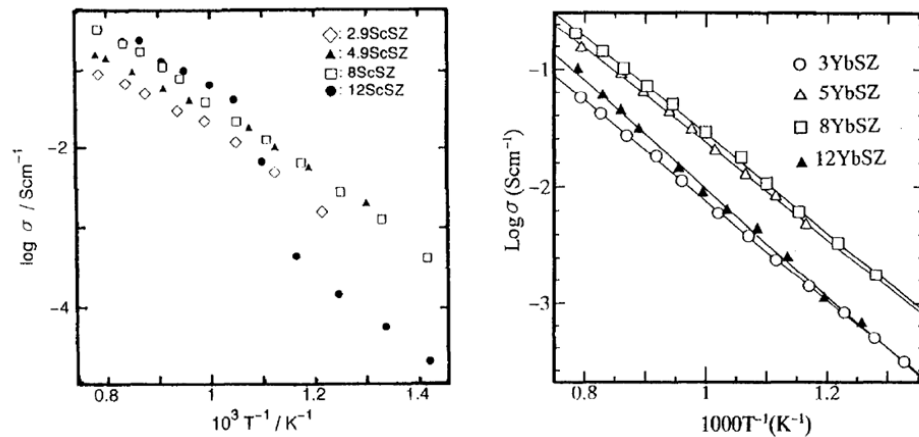
Figure 2 - Temperature dependence of the electrical conductivity of scandia (left) and ytterbia stabilized zirconia (right) from [19].

Given this temperature dependence, it is evident from both Equations 9 and 10 and Figure 2 that two defining factors in the design of an SOFC electrolyte, for a given material, are the thickness and the operating temperature.

Concentration polarisations arise from the fact that the reactions which take place within a fuel cell do so at the triple phase boundary (TPB). The TPB is the name given to the region which contains high ionic and electronic conductivity in addition to the presence of reactant gases; typically located at the interface of the electrolyte and catalyst particles [13]. The losses termed concentration polarisation arise from the diffusive characteristics of the oxidant, or fuel through the cathode, or anode, and is consequently a function of the electrode structure [20] which is a major contributor to the magnitude of concentration polarisations [21, 22].

Concentration polarisations ultimately lead to a limiting current within a cell due to depletion of reactants at the TPB; a full derivation of the model is given by Chan *et al.* [2] with the final equations developed shown below in generalised terms.

$$\eta_{conc,anode} = -\frac{RT}{\dot{n}_e F} ln \left[\frac{\left(1 - \frac{RT}{\dot{n}_e F}\right)\left(\frac{l_a}{D_{a(eff)}p_{H_2}}\right)i}{\left(1 + \frac{RT}{\dot{n}_e F}\right)\left(\frac{l_a}{D_{a(eff)}p_{H_2O}}\right)i} \right]$$

(11) Anode side concentration polarisation model

$$\eta_{conc,cathode} = -\frac{RT}{\dot{n}_e F} \left[\frac{\left(\frac{p_c}{\delta_{O_2}}\right) - \left(\left(\frac{p_c}{\delta_{O_2}}\right) - p_{O_2}\right) exp\left[\left(\frac{RT}{\dot{n}_e F}\right)\left(\delta_{O_2} l_c / D_{a(eff)} p_c\right)i\right]}{p_{O_2}} \right]$$

(12) Cathode side concentration polarisation model

The structure of the above equations highlights the importance of the cathode structure in minimising the concentration polarisation. The

inclusion of the δ_{O_2} term, which incorporates a range of structural properties such as tortuosity and voidage, by developing an effective diffusivity ($D_{a(eff)}$) term which accounts for the porous structure of the electrode and the thickness (l_c) of the cathode within the exponent, exposes the cathodic concentration polarisation to the effects of these parameters in a more severe fashion than the structure of the anodic polarisation in Equation 11 [2]. These dependences can be alleviated through intelligent fuel cell design, enabling the performance to be maximised. By tailoring the microstructural characteristics of the electrodes, the porosity and tortuosity can be improved, aiding the flow of reactants to and from the electrodes. The macrostructural characteristics of the device can also be adapted to aid performance; this is seen particularly in the design of SOFC cathodes which are typically manufactured to be thinner than the anode to improve the concentration polarisations observed.

Similarly to the activation and Ohmic polarisations, an increase in current being withdrawn results in an increased concentration polarisation, thus a balance must be made when operating a cell. In short, a cell cannot be operated at a high voltage and current, nor a low current and voltage and so a choice must be made as to the prime operating point for a given cell and requirement. This operating point is typically obtained by finding a suitable balance

between the maximum of the polarisation curve and a curve which describes the power of the cell at a given current, known as a power curve. A sample power curve is shown in addition to polarisation curve in Figure 3.
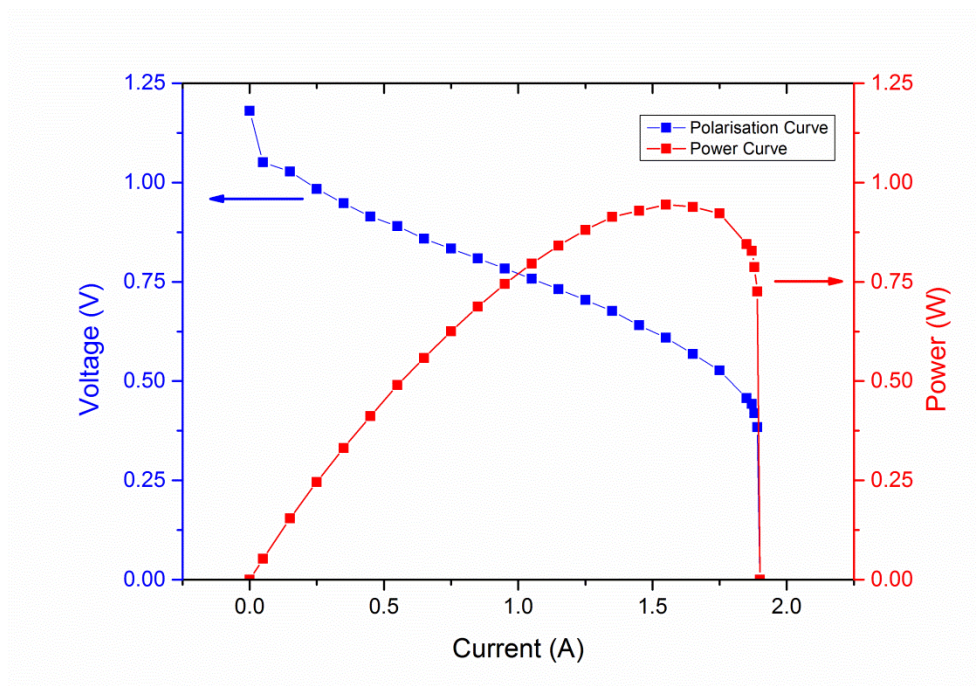
Figure 3 - Modelled polarisation and power curves for a PEMFC.

By optimising the operation of a system between the ideal location on the polarisation curve and power curve, a stable voltage can be obtained delivering relatively high power. In the system described in Figure 3 if one were to operate at the peak power, a slight increase in current may result in a drastic voltage drop by entering the concentration polarisation region resulting in degradation of the catalyst in the fuel cell. Similarly operating the fuel cell in the activation polarisation region will result in severe voltage changes as a result of small changes in current; therefore, fuel cells are typically

operated within the 'Ohmic region' to allow for stable and reliable operation that is a trade-off between power delivery and efficiency.

1.1.1.1. Polymer Electrolyte Membrane Fuel Cells

As the name suggests, the PEMFC utilises a polymeric membrane to separate the anode and cathode, this membrane is composed of a solid polymeric material, which allows for the transport of H^+ ions from the anode to cathode. The membrane is well described for this operation; however, it does limit the operating temperature of the cell to approximately 100 °C. While this has implications for operation due to increased polarisations when compared to higher temperature operations, the use of catalysts can greatly mitigate these losses. The main area of research over the last few decades has been to increase the operating temperatures towards 200 °C while avoiding the challenges associated with maintaining hydration in the membrane. Low temperature operation gives a PEMFC a quick start up time, with the membrane electrode assembly (MEA) providing a compact and high power density unit, which allows for its use in portable applications [23]. The MEA consists of a polymer electrolyte, often Nafion, supported by two porous carbon layers which are coated in a catalyst to form the electrodes of the assembly. A schematic of a typical PEM MEA is shown in Figure 4.
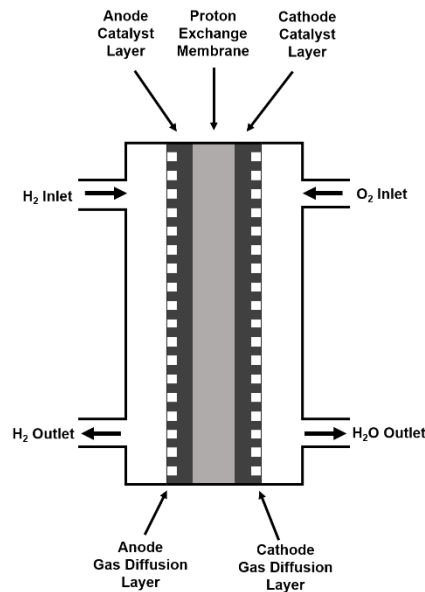
Figure 4 - Typical PEM membrane electrode assembly, adapted from [24].

As the mobile ion within a PEMFC system is the H^+ ion, the waste product (i.e., H_2O) is formed at the cathode. The fact that the mobile ion is not an oxidising ion reduces the number of potential fuels when compared to SOFC's; indeed, the only fuel that can be used within a PEMFC is a proton donator, typically this is hydrogen. PEMFC have a number of disadvantages when compared other types of fuel cell, not least the relative lack of resistance to impurities.

The use of hydrogen as a fuel can be problematic for PEMFC's as hydrogen is typically formed from reformed hydrocarbons and will contain trace amounts of H_2S and CO, which have been reported to be detrimental to the operation of PEMFC's. Quantities as low as 10 ppm of CO in the fuel stream can reduce cell performance [24]. The effect of these contaminants have been reported to be reduced at

higher temperatures by Zhang *et al.* who also demonstrate improved performance of PEMFC's due to reduced polarisations [25]. These performance implications have led to a drive to increase the operating temperature of PEMFC's; however, the challenges associated with this desire are not insignificant, mainly due to the components of the MEA itself. As the membrane is typically aqueous based polymer membrane dehydration can be a significant issue at higher operating temperatures which in turn causes degradation in the conductivity of the membrane.

The conductivity of the polymeric membrane is highly dependent upon the relative humidity of the gases within the cell with increased humidity increasing the ionic conductivity; however, in increasing the humidity the fuel is diluted. In addition, excessive humidity can lead to flooding of the electrodes, resulting in performance limitations. The main areas of research has been in improving the membranes used within PEM cells, improving catalysts and on modelling of PEM cells to improve water management and optimise performance. The development of membranes which can operate at higher temperatures has been highly reported with the use of acid-base membranes being reported to be amongst the most promising areas of development [26], such membranes have been demonstrated to operate at temperatures up to 180 °C, which significantly improve PEM fuel cell kinetics thus reducing the corresponding polarisations.

However, problems have been reported with the start-up of such cells as the proton conductivity of membranes is reduced at low temperatures, and more research is required in order to optimize cell design and compatible materials.

The most common catalyst used in PEMFCs is Pt based; however, this has obvious cost implications; as such a large amount of research has been conducted into producing lower cost alternatives. The reduction of cost associated with such a development could be a key factor in the viability of PEMFCs. The cost reduction requirements is starkly illustrated by the 2020 target set by the US DOE which targets an operating cost of \$40 kW^{-1} for a system operating at 60% peak efficiency for 5,000 hours [27].

1.1.1.2. Solid Oxide Fuel Cells

The SOFC is a fuel cell which operates at significantly higher temperatures than the PEMFC with two broad classes of SOFC being defined; the Intermediate Temperature (IT) SOFC in the range 500–750 °C and the High Temperature (HT) SOFC in the range 750–1000 °C [28]. SOFCs are manufactured using a solid ceramic electrolyte which allows for the transport of O^{2-} ions from the cathode to the anode. Significant research has been undertaken into the material selection for the anode and cathode, while the electrolyte has also attracted significant attention over the course of the last 20

years. In contrast to the PEMFC, the use of an oxide ion conducting membrane results in the chemical products being formed at the anode. The mechanism of operation also enables a much wider range of fuels to be exploited. Indeed SOFCs have been heavily researched using methane as the fuel of operation; enabling such devices to be used in conjunction with existing infrastructure. Typical SOFC design targets include an operating lifetime of 10^5 hours; whilst the ceramic components are also required to be relatively simple to fabricate and demonstrate sufficient mechanical strength to prevent fracture during this timeframe.

The anode is situated in a very harsh environment within the SOFC as it exposed to both high temperatures and an oxidizing environment. The anode must be porous to enable diffusion of fuels and exhaust gases to and from the TPBs; where the fuel gas can interact with both the electrolyte to receive ions and an electrically conductive pathway to donate electrons [13]. A schematic view as to the nature of a TPB is shown in Figure 5.
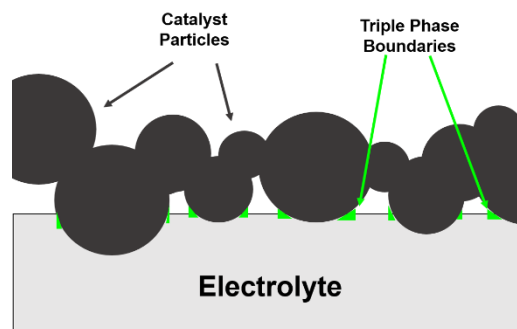
Figure 5 – Simplified schematic illustrating the nature of triple phase boundaries showing the TPB areas (green) where the electrolyte, catalyst and gas phases are mutually in contact, adapted from [13].

Given this aggressive environment, it is imperative that the anode is chemically passive towards the electrolyte, so as to not result in the formation of unwanted by-products. The anode must also catalyse the oxidation of the fuel while not encouraging side reactions, which may reduce the efficiency of the cell [29]. In addition, if hydrocarbon fuels are to be used, the anode must not lose activity in the presence of carbonaceous deposits or other impurities, such as sulphur compounds, in the fuel.

Typically, Ni / ceramic cermets are used for the anode as Ni is an effective catalyst at the elevated temperatures associated with SOFC operation, with the ceramic portion of the mixture providing the ionic (typically an oxide ion) conductivity. The anode must also be thermally compatible with the other components of the fuel cell; i.e. it must expand and contract in a similar fashion to the other components (electrolyte and interconnect) to ensure fractures or delamination do not occur due to thermally induced stresses [30].

The cathode has similar requirements to the anode in that it too must be thermally compatible with the electrolyte and interconnect. It must also display a high degree of electrical conductivity and it must be chemically passive towards the other components to ensure no solid state reactions occur. The cathode must allow for the passage of ions to the electrolyte and must also be stable in the reducing

environment. Historically cathodes have been produced using a lanthanum based oxides [30]; however, the drive for lower operating temperatures have seen increased interest in 'next-generation' cathodes [31].

The electrolyte used in a SOFC must be both chemically and thermally compatible with both the anode and cathode; however, unlike the electrodes, the electrolyte must not exhibit electrical conductivity. The electrolyte must also be gas tight so to ensure the oxidant and fuel are not in contact, which will result in a significant drop in electrical potential of the cell [32]. An electrolyte that is electrically conductive will cause a short circuit in the cell and result in significantly impaired performance. The electrolyte must conduct the relevant ions; be they the traditional O^{2-} or a proton, similar to the PEMFC. For high temperature operation, the electrolyte most commonly used is yttria stabilised zirconia (YSZ) [33]; however, efforts to lower operating temperature has led to gadolinium doped ceria (GDC) being developed as an electrolyte; however, the electrical conductivity of GDC is higher than that of YSZ, thus further research it being undertaken to improve the electrolyte for intermediate temperature SOFCs operating between 500–700 °C.

To increase the voltage and power generated by SOFC systems, cells are stacked together using an electrically conductive interconnect. This layer is typically designed to have a minimum

electrical conductivity of 1 S cm^{-1} and be both thermally and chemically compatible with the both electrodes [32]. In addition, it is vital that the interconnect is gas tight to ensure the fuel and oxidant do not mix prior to reaction. One of the key driving forces behind the push for lower temperature SOFCs is the choice of material for the interconnect, above 800 °C ceramic interconnects are preferred as metal alloys tend to be oxidised [34]; however, below this temperature metal alloys provide a much higher electrical conductivity. Coupled with this, metallic elements are easier to fabricate and are more cost effective as they do not contain expensive rare earth elements [35].

1.1.2 Li-Ion Batteries

Li-ion batteries have had a transformative effect on portable electronics since they were first commercialised by Sony in 1991; however, these devices are being employed in increasingly compact and power intensive environments, including in power trains for automotive applications [36-38]. Recent high profile incidents [39, 40] and safety concerns have resulted in a wide array of safety componentry and other safeguards being built into battery packs; it has also led to significant research into improved cell designs. However, these additional components add to the economic cost of systems, whilst reducing both the volumetric and gravimetric power density. As such, recent attention has turned to improving thermal

management of Li-ion systems [41]; by enhancing thermal homogeneity the volume and weight of battery packs can be improved, whilst also prolonging the life of devices.

Li-ion batteries are constructed from three distinct layers, a graphitic anode, an aqueous electrolyte and a Li based cathode which varies in chemistry which typically is used to identify the cell type. The electronic current is enabled by the transfer of Li^+ ions across the electrolyte from the cathode at which point it intercalates within the graphite anode. As this process is occurring, electrons are transported through current collecting layers within the cell and passed across an external circuit before recombining with the Li^+ ions. As such, the generation of heat in a battery is a complex sum of entropic and Ohmic contributions associated with the reactions and the flow of current within the cell [42, 43]. This results in significant temperature variations both within the cell and between internal and surface regions [44, 45]. Despite this the surface temperature of a battery can be related to the internal temperatures using a variety of techniques [46, 47], and is of course vital in the thermal management of systems [48, 49].

1.2 Heat Generation in Electrochemical Devices

Heat generation in electrochemical systems is a complex phenomenon involving the operating voltage, current, size of cell and

material of construction, amongst other factors. The sources of heat in a single cell, be it a fuel cell or battery, are comprised of reversible and irreversible components, with the reactants involved having a bearing upon both aspects. As such, the mechanisms of heat generation for both a simple fuel cell system and a Li-ion cell will be detailed using a generalised terminology with $\dot{n}_e$ representing the number of electrons liberated. In the simplest PEMFC case operating using a hydrogen fuel, two electrons are involved in the reaction, whilst four are present in the case of an SOFC under the same circumstances; this however may vary if the fuel cell is operated using a different fuel. In contrast Li-ion cells involve a single electron transferred during the reaction irrespective of the materials used at either the anode or cathode.

In any electrochemical system the heat generation is governed by two terms [50] – the reversible entropic heat generation (Q_{rev}) and the irreversible heat attributable to Ohmic heating and to losses incurred to facilitate the reactions in the activation region (Q_{irrev}) with the total heat generation (Q_{tot}) given by:

$$Q_{tot} = Q_{rev} + Q_{irrev}$$

(13) Total heat generation in a simple electrochemical system [50]

The reversible heat, which is dependent upon both the entropic change of the total reaction (ΔS), can be derived from thermodynamics for a given temperature (T) and operating current

(i). Additionally, the number of electrons transferred ($\dot{n}_e$) has a bearing upon the total reversible heat. The total reversible heat generated is given in Equation 14:

$$Q_{rev} = (-T\Delta S)\dot{n}_A = (-T\Delta S)\frac{i}{\dot{n}_e F}$$

(14) Reversible heat generation in a simple electrochemical system

The irreversible heat generation, which is related to the Gibbs free energy of the system (ΔG), can then be given by a function of the operating current the operating potential (E_{op}) and the enthalpy of the system (ΔH).

$$Q_{irrev} = \left(-\frac{\Delta G}{\dot{n}_e F} - E_{op}\right) \cdot i = \left(-\frac{\Delta H - T\Delta S}{\dot{n}_e F} - E_{op}\right) \cdot i$$

(15) Irreversible heat generation in an electrochemical

With the total heat generation finally given by:

$$Q_{tot} = (-T\Delta S)\frac{i}{\dot{n}_e F} + \left(-\frac{\Delta H - T\Delta S}{\dot{n}_e F} - E_{op}\right) \cdot i$$

(16) Total heat generation in an electrochemical system

As mentioned previously, this heat generation is solely due to the reactions occurring within the system and as such does not consider external sources of heating or cooling, which in turn, will affect the overall heat generation rate due to the inclusion of these terms in the final equation; in addition to the effect of temperature on both the entropic and enthalpic terms.

1.3 Infrared Thermography

Infrared (IR) thermography is a non-contact technique which can be used to investigate the surface temperature of objects. This technique, which is often referred to as thermal imaging, relies on the measurement of emitted infrared radiation which can be detected either by quantum or physical mechanisms. By arranging arrays of detectors (known as focal plane arrays), two-dimensional thermal 'maps' or thermograms can be developed and analysed with high spatial, thermal and temporal resolution. These individual images can subsequently be compiled into films to examine 'dynamic' or transient processes, or to investigate the stability of systems.

Infrared radiation was first discovered by Sir William Herschel in 1800 and falls between the upper wavelengths of visible light and microwaves on the electromagnetic spectrum between approximately 0.8 μm – 1 mm [51]. All objects with a temperature above 0 K have an infra-red emission profile. The wavelength (λ) of emitted thermal radiation is described by Planck's law of thermal radiation which is shown in Equation 17 which describes the relationship between the temperature of a blackbody (T) and the radiant flux emitted per unit surface area of the same blackbody (M_v):

$$M_v(T) = \frac{2\pi h \lambda^3}{c^2} \frac{1}{e^{\frac{h\lambda}{kT}} - 1}$$

(17) Planck's Law of thermal radiation from [51]
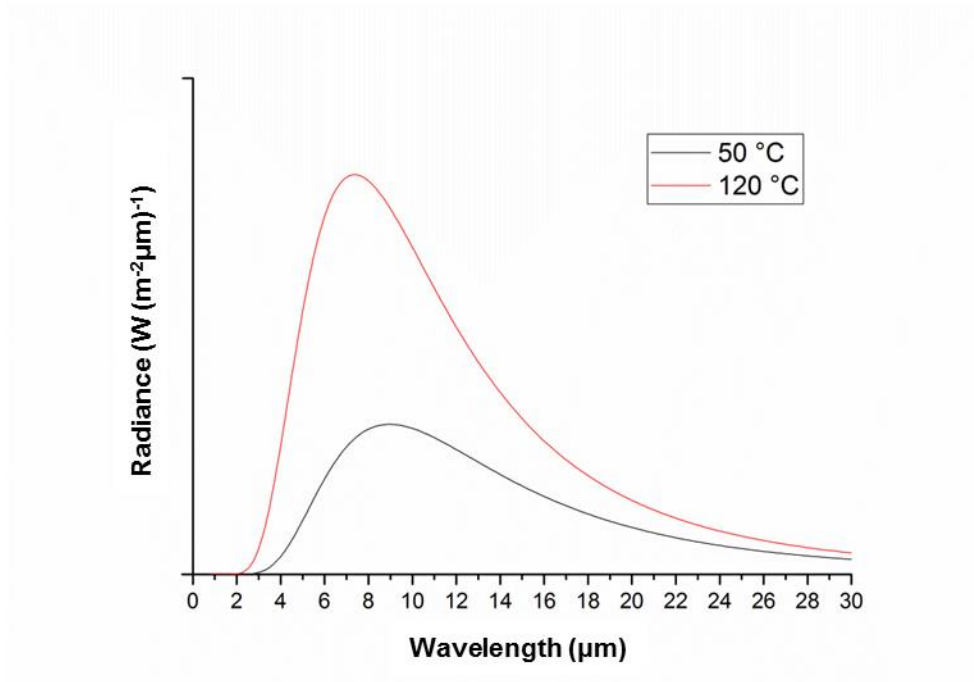
Figure 6 - Radiance emitted by a blackbody in thermal equilibrium at temperatures relevant to Li-ion batteries (50 °C) and polymer electrolyte membrane fuel cells (120 °C).

Figure 6 illustrates the dependence of emitted radiation on wavelength, with a higher temperature resulting in an increased quantity of emitted radiation. However, a spectral dependence is also observed from Figure 6; it is apparent that the peak wavelength of emitted radiation is heavily dependent on the temperature of objects with a lower peak wavelength being emitted at increased temperatures. This phenomenon can be observed in everyday life when objects become hot and emit radiation at wavelengths which correspond to the visible spectrum. Whilst emission spectra continue over a wide range of wavelengths (often extending beyond the 1 mm limit of infrared) the majority of these emission bands at temperatures exceeding -50 °C can be discounted due to the shape of the

emission distribution functions. Due to the positive skew within the spectral distribution function the majority of emitted radiation is emitted at wavelengths below 30 µm, with the peak located at significantly lower wavelengths. Indeed the peak wavelength (λ_{max}) may be simply calculated by simplifying Planck's law, resulting in Wien's displacement law.

$$\lambda_{max}(\mu m) = \frac{2897.8}{T(K)}$$

(18) Peak wavelength as given by Weins displacement law from [51]

Using Wien's displacement law it is possible to calculate the peak emission wavelength of a blackbody at any temperature. The peak wavelength of emitted thermal radiation from a blackbody as a function of temperature is highlighted in Figure 7.
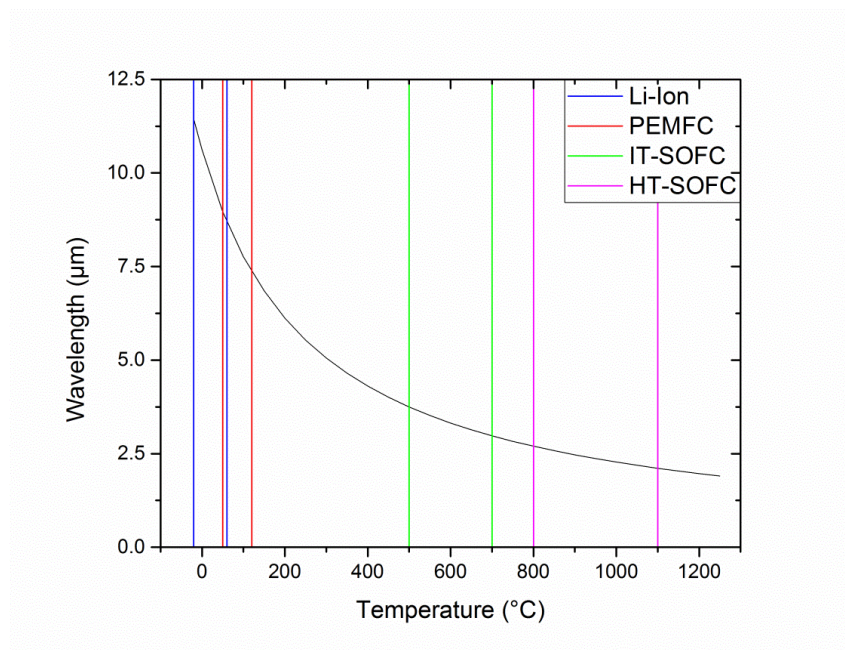
Figure 7 - Peak wavelength of emitted thermal radiation from a blackbody as a function of temperature indicating the approximate temperature range of a number of relevant electrothermal devices.

It is evident from Figure 7 that the peak emission wavelength for any electrochemical device operating within recommended temperatures is between 2.5–11 μm. Indeed Figure 7 indicates that two main emission bands exist for the peak wavelength of electrochemical devices, namely 2.5–4 μm and 7.5–11 μm. However, these emission bands are only valid for so-called 'blackbody' emitters or 'blackbodies'. Blackbodies are objects which absorb all electromagnetic radiation which strikes it, in turn re-emitting this radiation. Whilst blackbodies can be produced (typically using cavities [51]) it is rare that an object will exhibit blackbody behaviour. In order to take account of this a factor referred to as emissivity is employed. This quantity which is derived from Kirchoff's law of thermal radiation employs the first law of thermodynamics by positing that any incident radiation (J_{Tot}) must be either absorbed (J_A), reflected (J_R) or transmitted (J_T); this can be described mathematically as:

$$J_{Tot} = J_A + J_R + J_T$$

(19) Conservation of energy applied to an incident radiation flux

By taking the total incident radiation as a common factor, ratios may be defined for absorptivity (α), transmittivity (ρ) and reflectivity (τ):

$$\alpha + \rho + \tau = 1$$

(20) Equivalence of absorptivity, transmittivity and reflectivity

In turn, absorbed radiation must be reemitted, resulting in a further equivalence and the definition of emissivity (ε):

$$\varepsilon = \alpha$$

(21) Relationship between emissivity and absorptivity

By definition (and thermodynamics) the emissivity of an object cannot exceed unity, indeed the vast majority of surfaces reflect a proportion of the incident radiation resulting in an emissivity below unity. Additionally a given material may have a variable emissivity as a result of a wide range of conditions that can affect the value – including surface condition, temperature, geometry of the object and indeed the wavelength of incident light [52]. A surface which has a constant emissivity over all wavelengths is referred to as a greybody; however, emissive deviations can occur across short spectral ranges; in this instance the body is referred to as a spectral emitter. Sample emissivity values are shown in Figure 8 over an emission band of 0.1–10 µm.
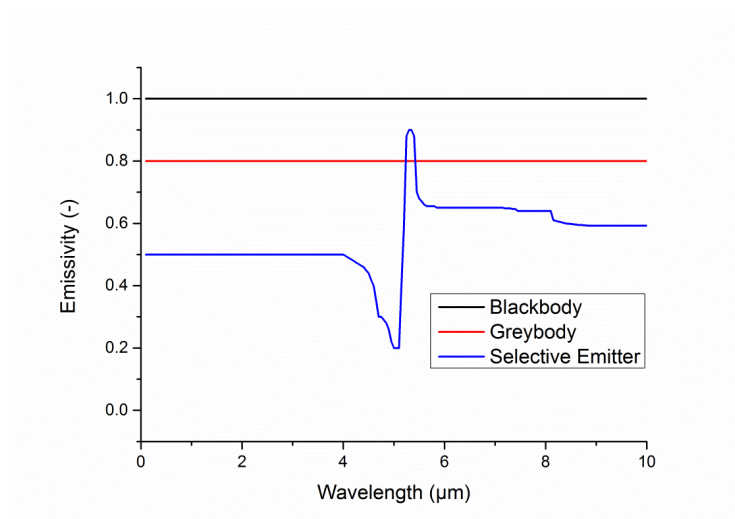
Figure 8 - Sample emissivity values for a blackbody, greybody and spectral emitter.

Recalling that the emission spectrum emitted by an object is dependent on the temperature of the object, it is evident that the emissivity may also be significantly dependent on temperature. This is of most concern when dealing in spatially or temporally variable thermal measurements. In this instance it is important that thorough and correct calibration procedures have been followed in order to obtain valid measurements, these calibration methods are dealt with in Section 3.1.1.

The spectral dependence of emissivity is also matched by transmittivity variations in materials. For instance, the atmosphere exhibits significant transmittivity variations throughout the infrared spectrum. Atmospheric transmission is shown in Figure 9 for the spectral range 0.1–14 µm.
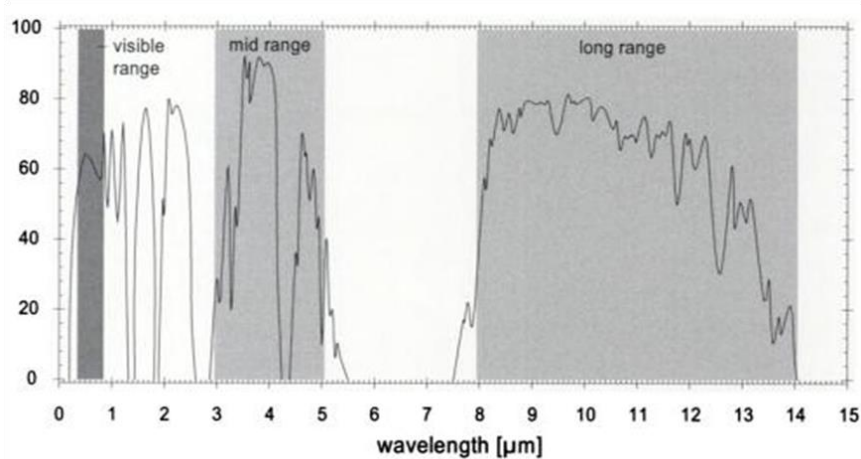
Figure 9 - Atmospheric transmission at 20 °C and 100% relative humidity at a distance of 6000 ft taken from [53].

The transmittivity of the atmosphere seen in Figure 9 is heavily dependent on a number of factors including the relative humidity of

the air, CO_2 and O_3 concentrations any particulate matter and the distance of measurement [54] and thus is usually subsumed under surface emissivity measurements; however, under certain circumstances, for instance long distance measurements, this must be considered due to potential variations between the object and objective. In addition to potential atmospheric concerns the objective angle must be considered when viewing objects. Whilst blackbodies emit equal amounts of radiation in all directions, real surfaces can show angular emissivity deviations; however, usually the emissivity of an object is approximately constant between an objective angle range of 0–45° [51]. This consideration is most important when considering non-uniform planes which may result in measurements of features which are at grazing angles to the objective; potentially resulting in misleading results.

The surface condition of an object is often the most important factor in obtaining accurate thermal measurements. While a low emissivity is not an insurmountable obstacle in obtaining a true temperature value the scope for errors in the measurement increases greatly. As such, the surface of an object is often treated with a highly emissive material (often a matte black paint). The surface coating process which is detailed in Section 3.1.1 enables a uniform spatial emissivity to be calculated. Additionally, due to the homogeneous spatial distribution, statistically relevant calculations can be made to

establish the emissivity of the object over the relevant temperature (and wavelength spectrum) which is important due to the shape of the distribution functions arising from Planck's law.

In order to measure surface temperatures a detector must be used which is activated within the spectral range of interest. Three main emission band regions are viable for infrared measurement due to this atmospheric transmission; the near-infrared (NIR) region located up to 1.4 µm, mid-range from 3–5 µm and long-range region above 8 µm [55]. The region of measurement will largely depend on the temperature of interest (as seen in Figure 7); however, the detector available may result in measuring within a non-optimised region. NIR measurements which correspond to the peak wavelength of extremely hot objects (in excess of 2000 K) can typically be viewed by conventional Si based charge-coupled device (CCD) cameras with suitable filtering [56]. However, when viewing objects below 1000 K background solar radiation is equal to and can surpass the emission of objects [57]. Whilst lower temperatures can be measured using these conventional CCD chips [58] excessive filtering can lead to challenges in establishing the emissivity of an object, as such a number of other technologies are typically employed.

Detectors for thermal imaging fall into two categories – quantum detectors and microbolometers. The latter are significantly cheaper and utilise the change in physical parameters in a material, typically the variation in electrical resistance due to alterations in temperature [59]. These detectors have a sensitivity of approximately 10 mK [60] however they are more prone to environmental noise [61] than quantum devices. Additionally, due to the time constant associated with the change in electrical resistance, microbolometers have significantly lower frame rates, typically 30 Hz [62]. Arrays of amorphous silicon or vanadium oxide [59, 63, 64] are arranged in order to provide the spatial resolution with the pitch of these so-called 'focal plane arrays' governing the ultimate spatial resolution of measurements.

Due to the continued progress in materials science and limited scope for improvement, microbolometers are increasingly becoming an obsolete technology in the field of applied science [65]; however, they have continued application in consumer products. Quantum detectors on the other hand utilise advanced CCD chips to detect incident photons in order to produce a voltage which can be harnessed for temperature measurements [62]. The CCD chips which are used in infrared cameras are varied; however, irrespective of the material the device must be cooled in order to obtain accurate measurements to reduce the probability of thermally excited free

charge carriers producing a response signal. Historically this cooling has been achieved using liquid N_2; however, modern CCD detectors are cooled to approximately 70 K using a Stirling cooler. Quantum detectors are less prone to environmental disturbances (assuming the frame is configured correctly) than microbolometers and also offer significantly higher frame rates at similar sensitivities [62].

Quantum detectors operate by measuring a change in the free charge carrier concentration in the semiconductor which is induced by incident electromagnetic energy. In order for any change to occur a minimum energy must first be reached, with any incident radiation below this cut-off wavelength remaining undetected. The cut-off energy of a detector is determined by the band gap between the valence and conduction bands of the semi-conductor which must be exceeded. The cut-off energy (denoted by ΔE) can be used to determine a cut-off wavelength (λ_{cutoff})and frequency (v_{cutoff}) [51], as seen in Equation 22:

$$\Delta E = hv_{cutoff} = \frac{hc}{\lambda_{cutoff}}$$

(22) Cut-off frequency and wavelength of a quantum detector

Assuming the infrared radiation of interest is above the cut-off wavelength the current response of the detector is related to the quantum efficiency of the semi-conducting material and to the flux of incident photons on the detector ($\Phi_{radiation}$). This quantum flux

$(Z_{radiation})$ can be calculated using Equation 23 with the current response $(I_{detector})$ shown in Equation 24:

$$Z_{radiation} = \lambda \frac{\Phi_{radiation}}{hc}$$

(23) Quantum flux of incident radiation as a function of incident radiative power

$$I_{detector} = C_1 \eta Z_{radiation}$$

(24) Quantum detector current response to incident quantum flux

By understanding both the incident radiative flux and the resultant signal generated, the responsivity (R_λ^I) of the detector can be seen to be dependent solely on the quantum efficiency (η) of the semi-conducting material used and the wavelength of incident light:

$$R_\lambda^I = \frac{I_{detector}}{\Phi_{radiation}} = \frac{C_1 \eta \lambda}{hc}$$

(25) Responsivity of a quantum detector

Detectors can be characterised according to a number of quantitative relationships, the most useful of which is the noise equivalent temperature difference (NETD). The NETD is the minimum blackbody temperature difference which can be distinguished using the detector. The NETD of a quantum detector is image dependent and given by the ratio of signal change to a combination of the noise of the image. The noise equivalent power (NEP) is used to quantify this background noise and can be calculated for a given bandwidth (Δf) using Equation 26 by measuring the energy of incident photons (E_{photon}):

$$NEP_\lambda = \frac{2E_{photon}}{\eta}\Delta f$$

(26) Wavelength dependent noise equivalent power (NEP) for a quantum detector

Using this term the NETD can be obtained according to Equation 27:

$$NETD = \frac{I_{detector}}{NEP}$$

(27) Noise equivalent temperature difference (NETD) for a quantum detector

By identifying the NETD a signal-to-noise ratio can be established; therefore, in order to ensure the accuracy of thermal measurements an uncertainty related to the NETD must be applied to all temperature measurements, with the appropriate minimum signal-to-noise ratio being heavily dependent upon the framing of the image. This criterion can be demonstrated using the simple case of an object at a uniform temperature being imaged with uniform background and atmospheric conditions. In this instance the incident radiation on the detector (Φ_{det}) can be described by a combination of terms based on the radiation emitted by the object (Φ_{obj}), the radiation emitted by objects included in the background of the frame (Φ_{back}) and atmospheric radiation (Φ_{atm}). As seen in Equation (28 these terms must be conditioned by the emissivity of the object in addition to the transmittivity of the atmosphere (τ_{atm}):

$$\Phi_{det} = \tau_{atm}\varepsilon\Phi_{obj} + \tau_{atm}(1-\varepsilon)\Phi_{back} + (1-\tau_{atm})\Phi_{atm}$$

(28) Effect of background and atmosphere on radiation incident on the detector

In this special case, if the emissivity of the object is high the required signal-to-noise ratio will be lower than the case of a highly reflective material. Additionally, if the transmittivity of the atmosphere is high within the relevant wavelengths the minimum signal-to-noise ratio required will be reduced.

Irrespective of the choice of detector an infrared camera utilises optical components in order to achieve adequate image quality. The optics used in infrared imaging differs from white light optics only in the materials used; due to the differing transmissive properties of materials at the respective wavelengths of interest. Indeed, standard silica glass which is highly transparent in white light has a very high emissivity for infrared wavelengths rendering it opaque in the infrared spectrum. Germanium is used for many infrared optics due to its high transmittivity with infrared wavelengths, and is often coated with an anti-reflective coating to improve the image quality. This anti-reflective coating which can be a single or multiple layer coating of materials such as magnesium fluoride or aluminium oxide can significantly reduce the reflectivity of materials [51] and reduce the prospect of a phenomenon known as the Narcissus effect, which occurs when the camera detects a reflection of itself due to reflections. This can result in severely misleading temperature readings – particularly when the camera detector is cooled.

Whilst the optical lenses used in thermal imaging are manufactured to be highly transmissive to all infrared wavelengths the transmittivity of infrared windows can be highly variable across the spectrum. The material used for an infrared window has a number of design criteria which must be met to ensure the efficacy of the window [66]:

- Optical transparency to IR light in the requisite wavelength range.
- Low optical emissivity.
- Similar coefficient of thermal expansion (particularly at high temperatures).
- Chemical and physical compatibility with reactants and housing.
- Sufficient mechanical strength under operating conditions.

A wide number of materials can be used as infrared windows with a small selection of these materials shown in Table 2:

Table 2 Properties of various windows transparent within the infrared regime.

	CaF_2	BaF_2	Sapphire	ZnSe	Ge (Untreated)
Transmitted Wavelengths (µm)	0.13 – 8	0.18 – 12	0.23 – 5	0.6 – 20	2 – 20
Surface Reflectance (%)	3.1	3.6	7.6	17	36
Chemical Incompatibility	Water (mild), Acids	Water (mild), Acids	HCl	Acids (mild)	Halogens, HNO_3
Knoop Hardness (kg mm^{-2})	158.3	82	1400	120	692

As can be seen from Table 2 the choice of window is heavily dependent on the system chosen – for instance if a CaF_2 window were used to view a SOFC anode the humidified gas may result in damage to the window over time. A number of authors have detailed the development of windows for infrared imaging with developments ranging from yttria windows [66] to multi crystal sapphire windows [67] which will enable the production of large windows with reduced imperfections.

2 Literature Survey

2.1 Thermal Management of Electrochemical Power Systems

The sensitivities to temperature of electrochemical power systems previously discussed have resulted in the development of a wide array of thermal management strategies. These control mechanisms are employed to ensure optimal performance, balancing the instantaneous performance of the system with long term stability and efficiency. Strategies are necessarily different between both low and high temperature fuel cells and batteries due to the various system idiosyncrasies; and indeed may be extended beyond the window of operation – a case which is particularly important with SOFC operation.

Due to the thermally mismatched materials within a SOFC system the heating and cooling cycles to and from operating temperature can have a significant impact on the thermal stresses within the cell. Whilst this is dealt with in greater depth in Chapter 5 it is important to consider this slow heating/cooling requirement when discussing thermal management. Thermal gradients which may be formed due to the internal reforming of fuels must also be considered in thermal management strategies [68]. In order to alleviate these gradients external reforming of hydrocarbon reactants can be performed; this does however significantly increase the balance-of-plant of the

system. A compromise can be found by performing partial reformation of the reactants prior to feeding it into the SOFC.

In contrast to SOFCs, thermal management strategies for Li-ion batteries focus primarily on cooling due to the high rate of heat generation and close packed nature of high power battery packs [69]. These issues have been exacerbated in recent times with a drive to improve the volumetric energy density of cells and packs; resulting from increasingly compact and power hungry consumer electronics. Indeed, some of the first work reported investigating thermal management of Li-ion packs highlighted the importance of the pack size and geometry [70] on the temperatures experienced within the system. Various solutions to thermal management issues have been proposed in the literature including both active and passive mechanisms.

As the name suggests, active cooling involves the active passing of a coolant through the battery pack; this method has employed both air and fluid as a coolant [71-74]. In order to increase the efficiency of this cooling mechanism modifications to the battery may be made, including the addition of fins to increase the surface area and in turn increase the efficiency of heat transfer in the system [75-77]. Other novel approaches to the thermal management of Li-ion cells have also been suggested, these include the use of the electrolyte as a

coolant within prismatic cells [78]; however, as with all multi-phase heat transfer, the efficacy of the system is governed by a number of factors including the coolant used, the flow-rates and the surface area of the cells. As such, planar or prismatic cells are more suited to this form of cooling, due to their large form factor which increases the exposed surface area.

In contrast to active systems, passive thermal management systems employ static, solid packing material. This management strategy has the advantage of not requiring parasitic power, for instance, the operation of fans/blowers which can reduce the effective power density of systems [79]. In addition, the volumetric density of the system, which is the key spatial consideration in high power battery systems, can be reduced by eliminating the need for ancillary systems using passive cooling technology.

Typically, phase change materials are used in passive thermal management systems. These systems use the sensible and latent heat of the phase change material to absorb heat from the individual cells within the battery pack. As the phase change materials do not generate any heat the net heat flow will always be from the cell to packing material, mitigating against temperature rises in cells. In producing these systems, cheap, abundant materials such as paraffin wax have been trialled [80]. Investigations have shown that

the low thermal conductivity of the material result in heterogeneous thermal distribution throughout the battery pack; as such, PCMs are often designed with a thin, highly thermally conductive mesh interspersed through the material [80-82]. This has the advantage of enabling the transfer of heat from the surface of cells into the full depth of the PCM cooling system; fully utilising the available thermal mass and improving the efficiency and efficacy of the system. Despite these advantages, work conducted by Karimi and Lu has highlighted the need for bespoke choices due to cost, size and efficacy when designing thermal management systems [83].

Whilst thermal management is a critical safety concern in Li-ion systems, in PEMFC stacks temperature control has a considerable impact on the electrochemical performance and durability of the stack. As a result of this, thermal management systems are often considered in conjunction with water management in these systems [84]. Pinhole formation in the polymeric membrane is reported to result from mechanical stresses generated due to repeated drying of the membrane [85]; as such, the humidity of inlet gases is a key concern. Hot (and indeed cold) spots can also result in membrane drying, resulting in swift degradation of the cells' performance [86-88].

The temperature and humidity of gases are also key determinants in the conductivity of the membrane in PEMFC systems [89], so effective thermal management mechanism is a key tenet in the design of PEMFCs. Open-cathode or air-breathing PEM fuel cells can be cooled by the flow of air across the exposed electrode, either through forced convection [90] or passive convection [91-93]. In the case of forced convection the parasitic losses associated with the fans and blowers must be considered in addition to the additional volume required to house the ancillary devices [94]. Despite this, it has been observed that the maximum achievable current density of air breathing PEMFCs under forced convection is significantly enhanced [90, 95].

Whilst high temperature operation can result in membrane drying, should the PEMFC be operated at too low a temperature flooding of the membrane can occur [96]. This phenomena is caused by water condensing on the surface of the electrode; blocking access to the triple phase boundaries, thus limiting the localised electrochemical reactions [97]. Depending on the operational mode this may force other regions of the fuel cell to operate at a higher current density; resulting in widely heterogeneous temperature distributions and potentially generating areas of localised membrane dehydration. Whilst physical modifications to the cell have been suggested to

prevent flooding [98], this critical issue can be mitigated through an intelligent thermal management strategy.

2.2 Thermal Imaging of Electrochemical Power Systems

2.2.1 Single Frame Imaging

Single frame thermal imaging has been widely used in order to obtain boundary conditions for models, or indeed, for model validation. However, single frames can also be used to describe the steady-state condition of devices with high accuracy. This mode of operation can also be used as a diagnostic – identifying areas of high or low electrochemical activity, thus elucidating vital information in the design and optimisation of systems. Air breathing PEMFCs were examined by Obeisun *et al.* [99] who looked at the temperature distributions associated with the passive fuelling strategy employed by these devices. An increased operating current was seen to result in increased surface temperatures, with inhomogeneous distributions being imposed on the device by the housing in which it was contained. The effect of clamping pressure was also observed to have an impact on the temperature distribution; with lower clamping pressures in the centre of the cell resulting in a lower temperature, this was attributed to poor electrical contact.
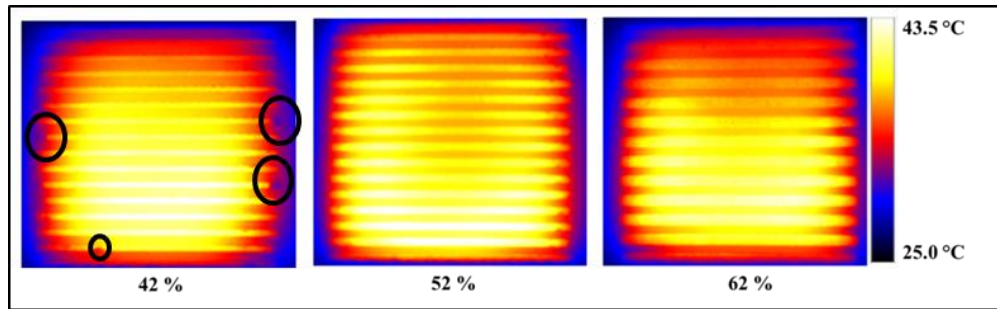
Figure 10 - Images showing the effect of the opening ratio of an air breathing PEMFC obtained by Obeisun *et al*. [99]. Heterogeneous temperature distribution is visible on the cell due to non-uniform clamping forces and the flow configuration in the system. Water formation can be seen at the edges of the cell at the 42% opening ratio as highlighted using the black circles.

As a result of this finding it was suggested that by increasing the opening ratio of the cell (in doing so enabling more reactant to reach the cell) the temperature at the centre of the cell may in fact decrease. Further work suggested that circular openings improved the electrical contact of the cell, enabling a larger opening ratio in the current collector, whilst maintaining sufficient electrical contact with the cell [99].

Martins *et al*. have validated a one-dimensional PEMFC model using thermal imaging [100]. Once more a non-uniform temperature distribution was observed; however, in this instance measurements were taken from the plastic fuel cell housing. Temperature variations of 6.5 °C (approximately 20% of the maximum absolute temperature) were observed at low operating currents (1.5 A). These variations, which were seen despite the additional thermal mass added by the plastic housing, were observed to be in agreement with the model

that the authors produced, which accounted for temperature variations along the flow channel.

A similar approach was taken by Matian *et al.* who used thermal images to validate a heat transfer model for PEMFCs [101]. To conduct this work the surface of a multi-cell stack was coated with a matte paint to achieve a uniform emissivity across the various layers which comprise the system. The temperatures obtained via infrared imaging were seen to be within 5% of the predicted values, with variations associated with the gas flow directions described as seen in Figure 11. It was also observed that the absolute temperature was higher on the cathode (air side) of the cell. The temperatures at the respective gas entry and exit points was seen to vary significantly, with the surface temperature decreasing by 33 °C between the air inlet and outlet. The temperature between the hydrogen inlet and outlet was also seen to increase by 8 °C. The work was subsequently expanded to include multiple cells with good agreement between the experimental results and the model observed once again.
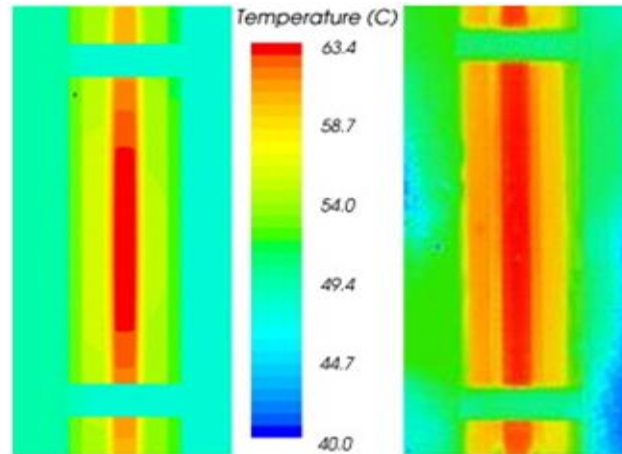
Figure 11 - Comparison of the temperature distribution of a two cell PEMFC system obtained using finite element analysis (left) and thermal imaging (right) reported by Matian *et al*. [101]. Good agreement is seen between the computational and experimental results, highlighting the impact of thermal imaging as a tool for model validation.

The flow direction of reactants was also seen to have an impact on the temperature distribution within a PEM device operated in electrolysis mode by Dedigama *et al*. [102] who showed a linear relationship between the operating current density and temperature of the electrolysing device at a number of operating current densities. In this instance the device was not painted; however, emissivity corrections were applied during the analysis of the results. Furthermore, the rate of heat loss was linked to the efficiency of the system which may be used to find an ideal operating point for PEM electrolysers.

In order to gain optical access to the surface of fuel cell electrodes modification of the system is often required, as demonstrated by Hakenjos and Hebling [103] who used a ZnSe window to observe the temperature at a PEMFC cathode. The interaction between cooling

54

gas streams and heat generating electrochemical reactions was observed, with a complex temperature distribution visible through the infrared measurements.
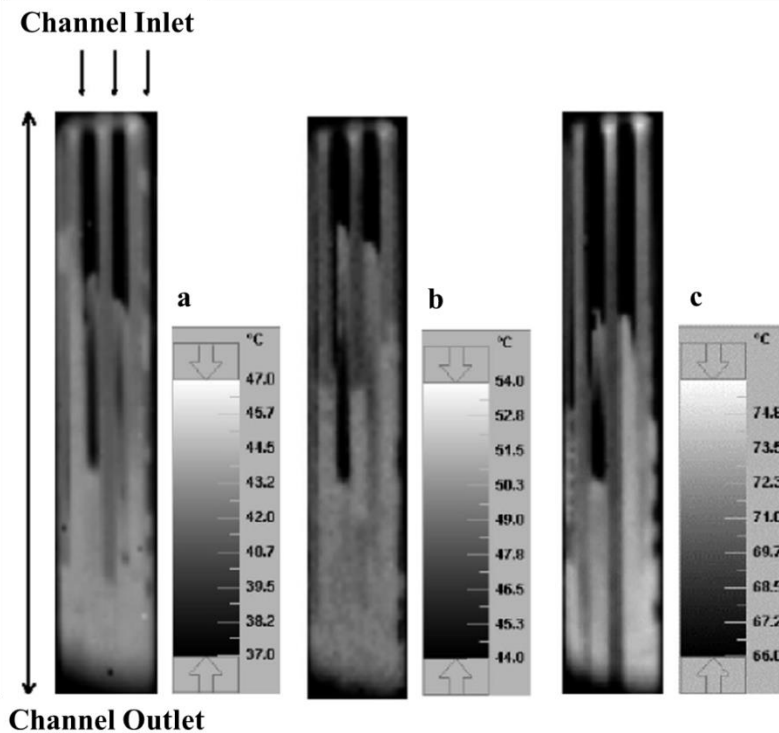
Figure 12 - The temperature distribution of a PEMFC cathode observed through a sapphire window as reported by Shimoi *et al.* [104] at three operating current densities: a) 345 mA cm^{-2}, b) 556 mA cm^{-2} and c) 992 mA cm^{-2}. Water formation and adherence to the window is visible towards the bottom of the cell through areas of white along initially black channels which masks the lower portion of the electrode in all measurements.

Shimoi *et al.* also used a window to examine the temperature distribution along flow channels in PEMFCs [104] as seen in Figure 12. This study highlighted water droplet formation as a major challenge to obtaining accurate thermal images of the cathode. Once again, hot-spots were observed at the electrode surface and a

dependence between the operating condition and temperature was seen.

Water formation also inhibited the imaging of the cathode temperature distribution in a study reported by Guo et $al.$ [105] shown in Figure 13. Despite this the authors were able to successfully image the anode (fuel side) of a PEMFC using a BaF_2 window. As this side of the fuel cell does not produce water, condensation on the window was not observed. This study showed increased temperature activity at both edges of the system which utilised an interdigitated flow field configuration. This was attributed to increased gas pressure in these areas, which in turn, increased the rate of electrochemical activity. A cooler region was observed in the middle of the cell which was suggested to be as a result of lower pressure due to the flow conditions. The effect of operating current densities was examined with small non-uniform temperature distributions being visible at 0.424 A cm^{-2}; these heterogeneities were seen to increase with increasing current densities.
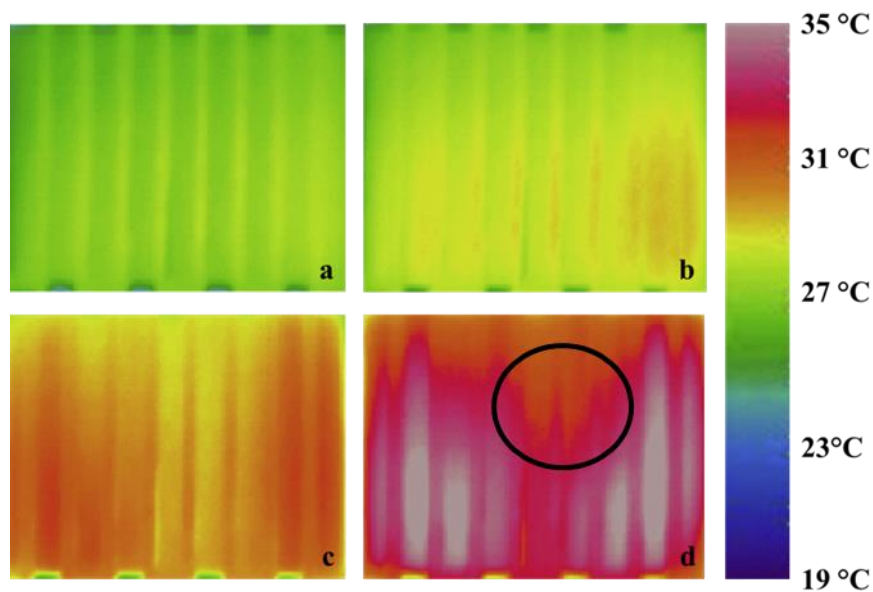
Figure 13 - PEMFC anode temperature distribution measured through a BaF$_2$ window by Guo *et al*. at current densities of: a) 424 mA cm^{-2}, b) 742 mA cm^{-2}, c) 1061 mA cm^{-2}, d) 1379 mA cm^{-2}. The effect of flow direction is seen most clearly in image (d) via the cold spot indicated by the black circle located in the middle of the cell.

Rather than inhibit the measurement as discussed previously, Daino *et al.* [106] used infrared imaging to visualise water formation through the MEA of a PEMFC. In addition to obtaining thermal information pertaining to the through-plane temperature distribution, the authors utilised the highly emissive nature of water droplets to identify the respective phases of water at the anode and cathode. It was observed that liquid water was present at the cathode, whereas water transport primarily occurs in the vapour phase at the anode. This work highlighted potential uses for thermal imaging as a visualisation tool to identify areas and artefacts in systems which have to date been considered inhibitory to accurate thermal measurement.

57

Models for Li-ion cells have also been validated using thermal imaging. Kim *et al.* has reported the validation of thermal models using infrared imaging [107, 108] seen in Figure 14; however, these studies only compared the model to a single discharge rate of 5C, with the validation images given after a discharge time of 10.8 min showing the behaviour of the battery at a very low state-of-charge.
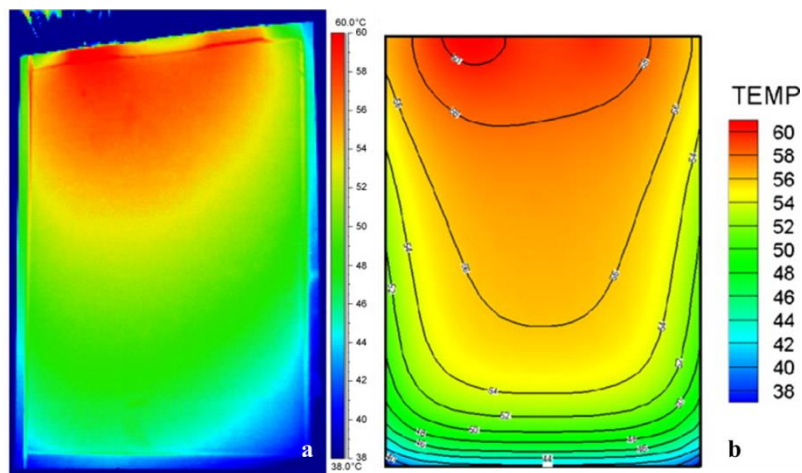
Figure 14 - Validation of finite element analysis developed by Kim *et al.* [107] to investigate the surface temperature of Li-ion batteries. Good agreement between the results obtained via infrared thermography (a) and computational modelling (b) are observed for this time point at a discharge rate of 5C.

Similar work was performed by Wang *et al.* [109] who performed a finite element analysis to examine the transient response of the temperature distribution on the surface of a planar cell. This model was validated using single frame thermal images taken at 5 minute intervals, which showed the temperatures at the current collecting tabs were higher than the average cell temperature.

The impact of cell design was studied by Waldmann *et al.* who investigated the thermal performance of six different cell designs [110]. In conducting this work the authors utilised thermal imaging on two of the designs, showing the deviations in surface temperatures which occur in planar and cylindrical cell designs. The thermographic results show that temperature distributions are significantly larger in the planar cells studied with variations approaching 20% observed. Work conducted at the National Renewable Energy Laboratory, by Peseran *et al.* [111] and Keyser *et al.* [112] have demonstrated the applicability of thermal imaging to investigate the thermal performance and characteristics of batteries which can be employed in both electric and hybrid vehicles. This work indicated an axial temperature distribution across the system, with large temperature variations visible at high discharge rates in a six cell system [111]. Further studies have shown a relatively uniform surface temperature distribution in a three cell system when cooling was present; however, mild heterogeneities were visible when the cooling was removed [112]. The research was then expanded to aid model development and battery design by Bharathan *et al.* [113] who charted the development of battery stacking technology by comparing the temperature distribution on two generations of power systems using similar cells, with a new method showing significantly more homogeneous temperature

distribution and a lower overall operating temperature for the same discharge rate.

2.2.2 Time Resolved Thermal Imaging

The use of time resolved thermal imaging has revealed the thermal effects of operational transients and failures of electrochemical devices. By examining these effects (and considering the entire system) control strategies can be altered to maximise the performance of both fuel cells and batteries. Noorkami *et al*. [114] used thermal imaging to validate a stochastic model aimed at incorporating temperature uncertainty into the operation of PEMFCs. This work involved the recording of thermal data at various points along the polarisation curve of an air-cooled, open-cathode commercial PEMFC. Once statistically relevant samples of data were obtained, distribution functions were generated and used to generate polarisation curves which included the uncertainty associated with the temperature measurement. The model revealed that rather than the widely reported polarisation curve, a polarisation 'band' results, which increases in width with increasing current. Additionally, it was observed that the fuel cell tended to operate towards a lower voltage, indicating that PEMFCs err towards poorer perceived temperature performance due to the natural variation in temperature within a given system.

Meyer *et al*. used thermal imaging to investigate the performance of commercial PEMFCs under a range of conditions. Dead-ended operation of the system was examined, showing a larger temperature rise with time during dead-ended operation than observed when the system was operated under through-flow conditions [114]. This behaviour was attributed to variations in the humidity within the system during operation, resulting in an increased current flow, and consequently an increased Joule heating effect.

A novel application of lock-in thermography has been employed by Robinson *et al*. [115] to identify defects within Li-ion pouch cells which has been detailed in Chapter 6. This technique uses an active sinusoidal stimulus (e.g. heat, light, acoustic) to increase the sensitivity of the detector in obtaining a frequency dependent amplitude image, whilst also enabling the acquisition of a phase image. Traditionally this technique has used a heat lamp as the stimulus to identify sub-surface defects in operational components. The work by Robinson *et al*. used the charge/discharge current of a Li-ion cell as stimulus, as illustrated in Figure 15(b).
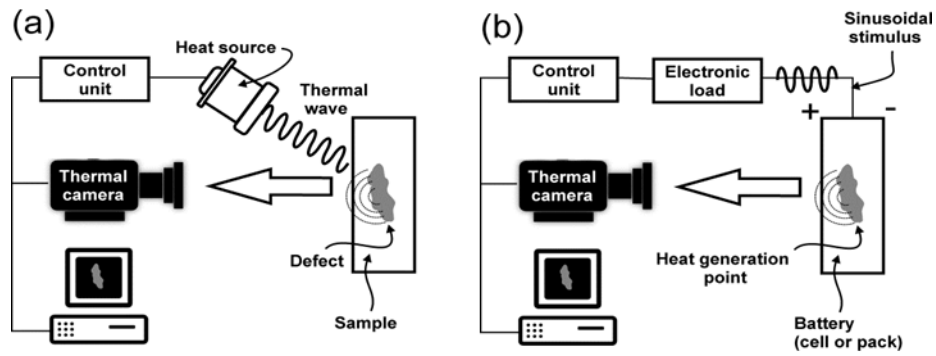
Figure 15 - Overview of lock-in thermography process highlighting (a) the traditional use of a heat lamp to detect subsurface defects and (b) the modified use of the direct electrical current emplyed by Robinson *et al*.

Work conducted using this novel experimental configuration showed that lock-in thermography can be used to identify internal structural deformation. The results show areas of increased electro-thermal impedance associated with areas of impaired heat transfer; in this instance it is associated with sub-surface gas pockets. It was suggested that this technique could have a significant impact on the study of Li-ion systems by enabling non-destructive identification of defects within cells *in operando*.

A similar technique was used by Engebretsen *et al*. [116] who combined lock-in thermography with a technique known as electrothermal impedance spectroscopy to investigate temperature distributions within an open-cathode PEMFC highlighting the potential for lock-in thermography as a tool in examining fuel cell systems.

Multi frame imaging of SOFCs was conducted by Pomfret *et al.* [117]; this work used low molecular weight alcohols (MeOH, EtOH) to observed the cooling effect of carbon formation. It was observed that operating both using methanol and lower operating temperatures (below 750 °C) resulted in increased carbon formation; however, above this temperature limited carbon formation was reported. Operation using ethanol was seen to result in significant carbon formation at all temperatures. As previously discussed, the operation of SOFCs using hydrocarbons is associated with significant endothermic reactions and associated temperature gradients; this operation mechanism may also lead to the formation of carbon on the surface of the devices. These temperature variations were observed *in operando*, while areas which were later revealed to be significantly damaged were also visible using thermal imaging. The greatest cooling effect was observed under ethanol fuelling at an intermediate operational temperature of 750 °C; this result was ascribed to incomplete pyrolysis of the ethanol reactant.

This work built upon foundations laid by the same author which detailed the effect of changing reactant flow from hydrogen to propane [56] (shown in Figure 16), and was subsequently expanded to investigate the effect of humidification on ethanol in subsequent articles [118, 119]. Once more, temperature variations associated with fuel cracking were observed; however, it was reported that

increasing the humidity of the inlet ethanol feed reduced the cooling effect. Despite this, areas of damage to the cell were reported for operation at 750 °C using wet ethanol; in contrast, operation of the cell under similar conditions using dry ethanol did not cause damage. Further work comparing the effects whilst operating under methanol and methane flows showed similar results; with cooling effects due to the cracking of hydrocarbon reactants reported across the surface of the SOFC anode [120].
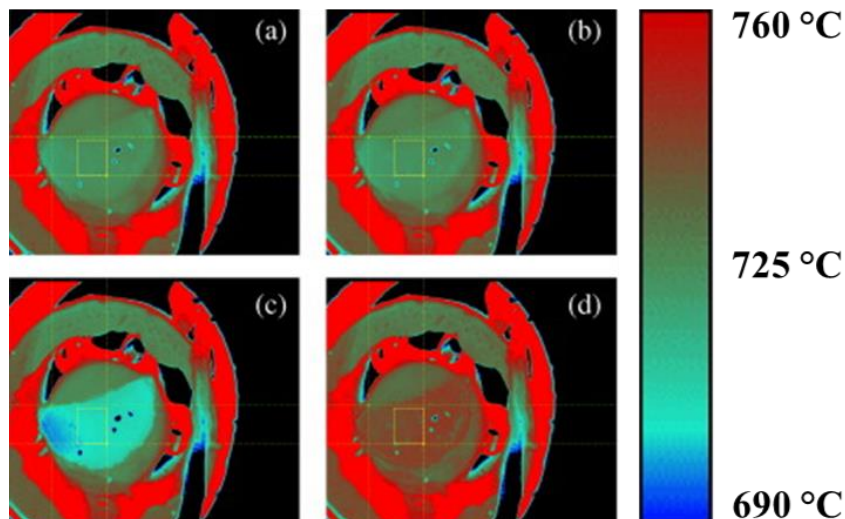
Figure 16 - Near infrared thermal images of an SOFC under Ar (a) with the maximum temperature changes shown for changes in flow to b) a H_2/Ar mixture, c) a propane/Ar mixture resulting in direct reformation of the hydrocarbon on the surface of the cell and associsate cooling and d) air as reported by Pomfret *et al*. [56].

Reports of thermal imaging of large form-factor SOFCs under hydrogen operation are limited; however, Brett *et al.* [121] used infrared imaging to investigate the effect of cell polarisation on a small pellet cell. In order to access the cell, only the cathode was imaged with temperature rises of approximately 2.5 °C at a current

density of 270 mA cm^{-2}. It was observed that the temperature rise associated with cell polarisation was higher at lower operating temperatures and it was also reported that by neglecting the increase in temperature, models risked underestimating the power available from the cell, particularly at high current densities. This prediction was enabled by calculating a total heat transfer coefficient for the cell from the thermal images obtained, highlighting the suitability of thermal imaging when validating models. Further work conducted by Schöttl and Brett [122] examined the effect of thermal shock on SOFCs, with relatively low flows of cooling gas (N_2) being sufficient to result in substantial temperature gradients (up to 10 $^{\circ}$C mm^{-1}) in the surface temperature of the cell – potentially inducing significant stress gradients as shown in Figure 17.
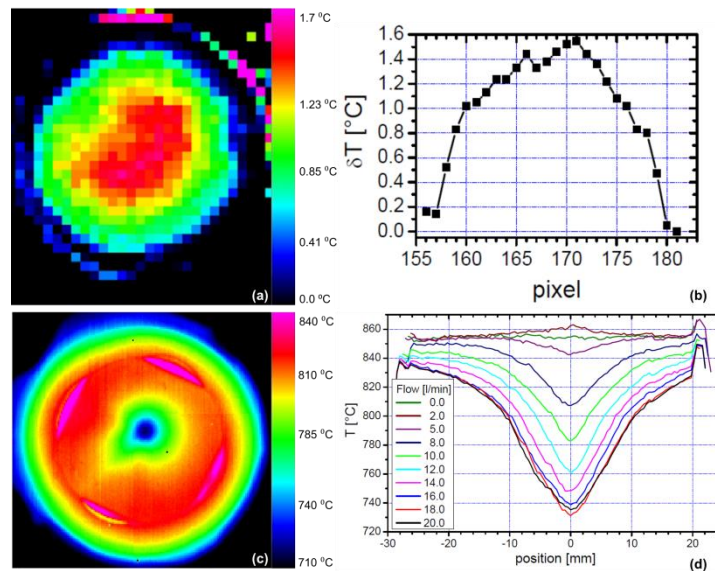
Figure 17 - Infrared image (a) and temperature distribution (b) of a pellet SOFC [121]. Also shown is the effect of introducing a cool N_2 stream to the surface of a SOFC cell (c) which is seen to generate large temperature variations (d), as reported by Schöttl and Brett [122].

Solid oxide cells were examined in electrolysis mode by Cumming *et al.* [123, 124] who showed that temperature rises were similar irrespective of the location, or absolute temperature of the cell. It was suggested that this observation (which contradicts that reported by Brett *et al.* [121] for operation in fuel cell mode) was as a result of the decreased electrolyte thickness. It was further reported that the concentration of hydrogen has an impact upon the rate at which the temperature rises; however, the ultimate temperature remains the same under both conditions. An observable change between endothermic and exothermic conditions was observed as the SOFC was reduced in voltage from 1.5–0.85 V, the extent of which was dependent upon the fuel-side reactant. Operation under steam rich conditions was seen to have a significantly smaller endothermic effect than under CO_2 rich conditions, with the opposite occurring during the exothermic portion of the voltage sweep; while co-electrolysis was seen to result in a temperature difference which lay in between the two extreme conditions examined.

The failure of Li-S batteries was investigated by Hunt *et al.* who performed the industrially standard nail penetration test on such cells [125] shown in Figure 18. In doing so, the effect of this critical safety test on the surface temperature distribution on the cells was examined. This test is used to evaluate the safety of battery systems to penetration by metallic objects with the associated short circuiting

has been observed to cause substantial temperature rises in traditional Li-ion cells [126, 127]. The work performed by Hunt *et al.* suggested that the Li-S chemistry which replaces the traditional graphite with sulphur in the anode are more stable to external short circuiting with a maximum temperature rise of 10 °C observed. Finite element analysis of Li-ion systems has also been validated using continuous thermal imaging. Kim *et al.* has shown excellent agreement between a two-dimensional model during both charge and discharge under constant power operation [128]. This work was expanded to a three dimensional model which also considered external electrical contacts by Yi *et al.* [128] shown in Figure 19.
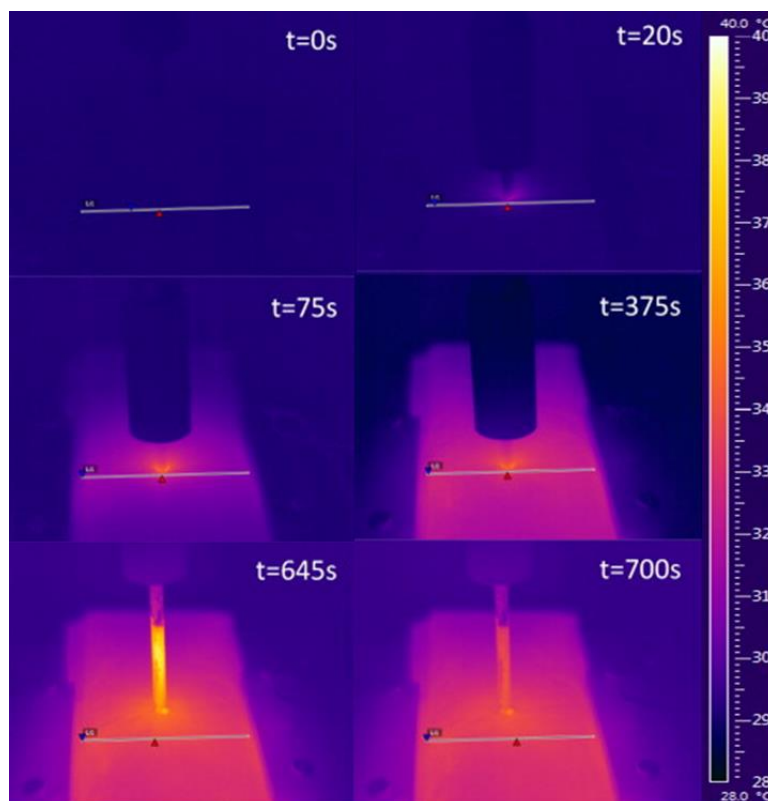
Figure 18 - Multi frame thermal imaging charting the temperature change associate with a nail penetration test conducted on a Li-S cell by Hunt *et al.* [125].

In both instances, non-uniform temperature distributions were observed, with the extent of the inhomogeneity increasing with increasing current. However, including electrical contacts was seen to significantly exacerbate the complexity of the thermal distribution throughout the cell. Temporal variations in the level of agreement were observed in the model produced by Yi *et al.* [128] with the model being most representative at longer time intervals. Despite this, the model enabled the approximation of better temperature dynamics to be examined in great detail with relatively high precision; demonstrating the efficacy of thermal imaging as a tool for the validation of temporally dependent models.
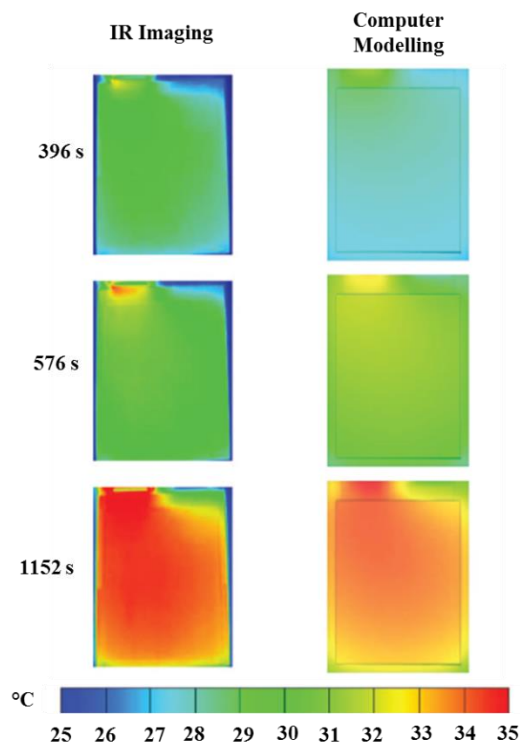
Figure 19 - Comparison of thermal imaging and finite element analysis conducted by Yi *et al.* [128] showing improved agreement with increasing time at a discharge rate of 5C. Note the effect of the electrical contacts (upper left) on the temperature distribution of the cell.

A continuous temperature monitoring system incorporating thermal imaging which interfaces with LabVIEW has been reported by Qin *et al.* [109]. This has potential not only for steady state and transient monitoring but also in quality control (QC) processes. A QC methodology has also been demonstrated by Duan *et al.* to identify defective batteries using a high current charging process [129]. This work showed that defective cells showed both higher and faster surface temperature rises when compared to pristine cells. As the cost of thermal imaging devices continues to decrease, it is feasible that these methodologies could be employed as a low cost automated screening process to monitor cells post production. Similar techniques may also be employed upon high risk power systems in vehicles and aerospace applications as a diagnostic to prevent catastrophic cell failure.

2.2.3   Correlative Metrology Employing Thermal Imaging

The use of a correlative metrological approach enables thermal imaging to be complimented by techniques which enable the systems examined to be understood in substantially more depth than otherwise. In performing a combined experiment, the dynamics of devices can be examined both *in situ* and *in operando*. There is no requirement, however, for sequential experimentation to identify causal mechanisms associated with the structure of devices.

Robinson *et al.* have combined *ex situ* X-ray microtomography with thermal imaging and electrochemical impedance spectroscopy to identify the cause of non-uniform temperature distributions on the surface of cylindrical Li-ion cells [130]. This work showed the presence of metallic safety componentry located at the positive terminal contributed significantly to the heterogeneous thermal distributions at discharge rates within the manufacturer's specified operating window for the cell and is discussed in depth in Chapter 4. Low clamping force, which results in poor electrical contact, was also identified as a potential cause of Joule heating at the negative terminal. Additionally, it was seen that a safety component known as a positive temperature coefficient (PTC), which is used to prevent excessive discharge rates, was not activated up to an ambient temperature of 60 °C.

Synchrotron radiation was employed by Finegan *et al.* (shown in Figure 20) to investigate thermal runaway in Li-ion cells [131]. This condition, which causes catastrophic failure of the cells, was examined *in operando* through a series of radiographic and tomographic measurements highlighting its devastating impact upon the internal structure of the cells. Infrared imaging was used to measure the surface temperature of the cells while it was subjected to thermal abuse designed to simulate conditions which would be experienced in the event of a fire. It was observed that thermal

runaway occurred when the surface temperature of the cell was within the region 230–260 °C. Hotspots were observed appearing on the surface of the cell using infrared imaging which is indicative of internal short circuits during the experiment. The Joule-Thompson effect was also observed through thermal imaging on the opening of the internal pressure relief valve. Transient temperature variations in excess of 700 °C were reported across the 65 mm diameter cell with the internal temperature of the cell reaching in excess of 1085 °C as evident copper globules formed by the melting of internal current collector material.
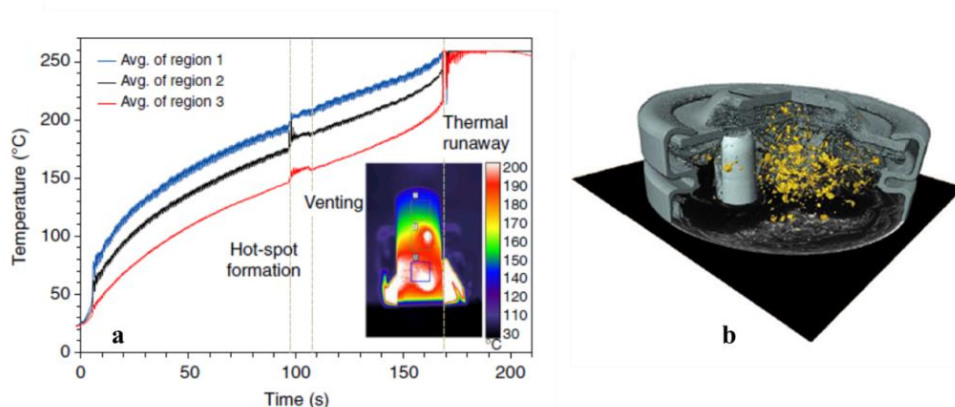
Figure 20 - Temperature measurements obtained by Finegan *et al.* [131] showing: a) the onset of thermal runaway and b) *post mortem* tomographic reconstructions of the top of the cell after failure. Copper globules formed during the cell failure are shown in gold and indicate a temperature of 1085 °C within the cell during the failure process.

Synchrotron radiation was also employed by Robinson *et al.* to investigate the effect of temperature variations on stress distributions within the Ni-YSZ anodes employed in SOFCs [131] which forms the basis of Chapter 3 in this thesis. This work, which involved the construction of a special high temperature furnace compatible with

the synchrotron beam line apparatus [132], utilised a fixed camera location in order to relate the one dimensional temperature variations generated to the location of the diffraction measurements across the cell sample. It was observed across a range of temperatures that the imposed temperature variations induce non-uniform stress distributions within the cell which exceeded those expected by up to 16 %. This work informed finite element analysis, which incorporated the measured temperature field into the a computational models using COMSOL Multiphysics [133].

The use of hydrocarbon fuels on the surface temperature of operational SOFCs was investigated by Kirtley *et al.* who combined thermal imaging with Raman spectroscopy and Fourier-transform infrared emission spectroscopy to give a holistic view of the processes occurring at the anode. Effects induced by methane were investigated and compared to those observed using biogas [134]. The combination of these techniques enabled the reforming process to be examined in substantially more detail than was previously possible, with the study observing that both gaseous carbon emissions and solid phase carbon deposits were reduced when operating in biogas. As carbon deposition has widely been reported to significantly impair and degrade the performance of SOFCs, this finding highlights the potential use of SOFCs in a more sustainable manner. This work expanded upon initial research conducted by

Eigenbrodt *et al.* [135] to investigate who once more combined thermal imaging with Raman spectroscopy to identify the type of carbon formed under both methane and methanol fuel flows. The inference of reactant cracking obtained using thermal imaging by the presence of large cooling effects was validated through concurrent Raman spectroscopy.

These synchronous studies highlight the benefit of a correlative approach when using thermal imaging – enabling processes to be identified in depth, which in turn results in an improved understanding of the mechanisms observed.

3 Experimental Methodology and Techniques

As the different thermal imaging experiments performed require significantly different operating parameters and configurations, the following section describes the key experimental methodologies common to all experiments including calibration of the thermal camera and construction of a frame. In addition, the scientific basis and background for a number of key techniques including electrochemical impedance spectroscopy, X-ray diffraction and microtomography is outlined.

3.1.1 Thermal Imaging Calibration Techniques

In advance of performing infrared imaging, calibration of the camera was required to achieve accurate results. Whilst the required calibration differed across all experiments due to environmental and material differences, a general procedure was followed for consistency. This section details how a general calibration procedure is performed using FLIR's Altair software.

1. Estimation of temperature range

Before conducting any experiment the required temperature range was estimated based on literature or experimental experience. Initially a wide temperature range is selected based on the two temperature calibration ranges provided by the camera: 15 – 250 °C

and 250 – 1500 °C. To enable more accurate temperature responses these ranges were subdivided depending on the experiments. In the case of a small temperature rise from room temperature to 30 °C a single calibration range encapsulating the range and sufficient contingency at each end was used to obtain the absolute temperature. This however is not necessarily the most appropriate method over a larger range of temperatures. If the temperature change observed is sufficient, multiple temperature calibrations were performed; sample calibration curves are shown in Figure 21.
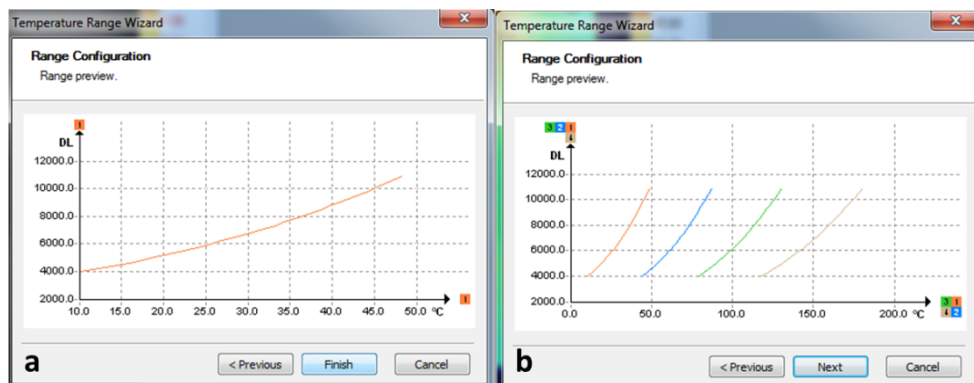
Figure 21 - Sample calibration curves obtained using Altair for a) a single temperature range from 10–47 °C and b) a four curve extended calibration range from 10–175 °C.

This calibration technique enables extended temperature ranges to be imaged; however when using this extended range of operation it is vital that the ranges overlap to ensure accurate measurement.

2. Estimation of effective emissivity

The effective emissivity of the sample; which may be a combination of the transmittivity of optics and emissivity of the surface of interest, was calculated prior to all experiments. The emissivity can be obtained by imaging the sample at a known temperature – however this may change over the range of temperatures imaged. In order to obtain the emissivity of high temperature samples a K-type thermocouple was placed on the surface of the sample. By imaging in the vicinity of the thermocouple the true surface temperature can be identified at that point, this protocol can then be applied through the relevant temperatures so that the effective emissivity of the sample can be obtained throughout the experiment.
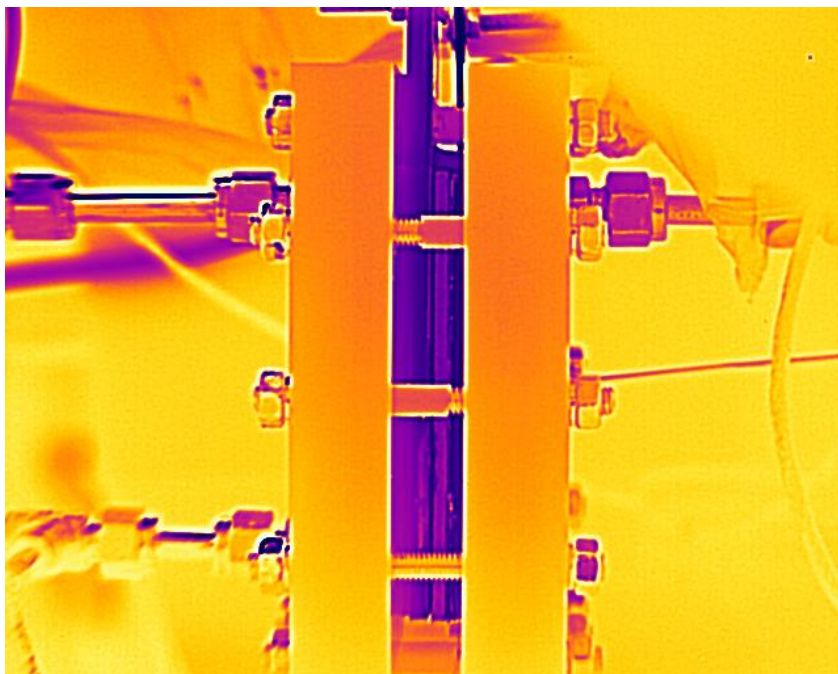
Figure 22 - False colour infrared image of PEM electrolyser taken at a uniform temperature.

Figure 22 highlights the importance of correcting for non-uniform emissivity. The PEM electrolyser shown in Figure 22 is composed of a number of materials including PMMA, carbon and copper; in this instance the entire device is imaged at a uniform temperature. If no emissivity corrections were performed the temperatures obtained from this infrared image would lead to significantly false results. This was demonstrated in a collaborative work performed by the author [102] investigating the transient thermal response of the PEM electrolysis shown in Figure 22. Emissivity values were calculated by allowing the device to reach ambient conditions and by shielding the experimental area, thus ensuring no reflections were leading to false results. Having allowed the device to equilibrate, points were selected along the various different components. The location of the components are shown in Figure 23.

By measuring the ambient temperature of the material ($T_{ambient}$) using a thermocouple the emissivity of each material (ε) was calculated to correct the surface temperature of the material as measured using infrared imaging ($T_{material}$) and remove an emissivity based errors as detailed in Equation 29:

$$\varepsilon T_{material} = T_{ambient}$$

(29) Calculation of the emissivity of a material

The list of emissivities calculated and physical thickness of the materials is shown in Table 3.
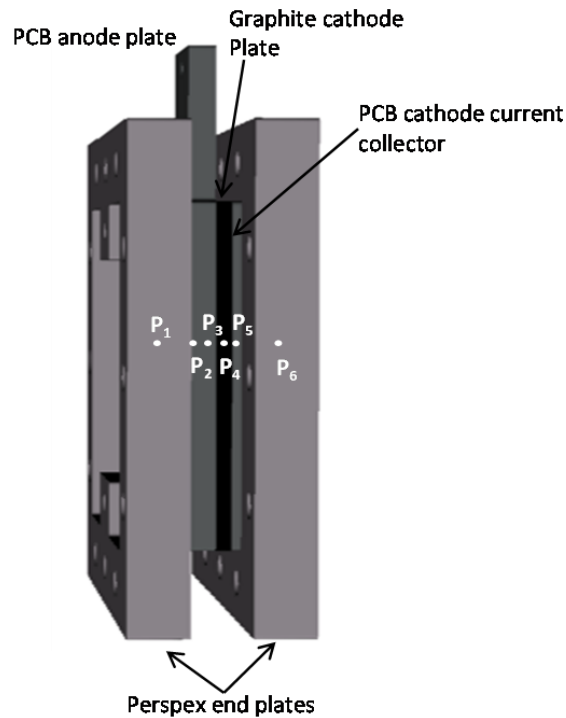
Figure 23 - Location points (shown as P_1–P_6) along the proton exchange membrane with the materials shown.

Table 3 - Emissivity and thickness of material at points as indicated in Figure 24.

Position	Material	Thickness (mm)	Emissivity
P1,P6	Perspex	20	0.85
P2,P3	FR4 (PCB)	3.2	0.79
P4	Graphite	2	0.27
P5	FR4 (PCB)	1.6	0.79

When the emissivities had been calculated the PEM electrolyser was operated at a number of current densities ranging from 0.2 A cm^{-2} to 1 A cm^{-2}. Figure 24 shows false colour images of the PEM electrolyser under the range of operating conditions and indicates

that the cell temperature increases with a corresponding increase in

operating current density.
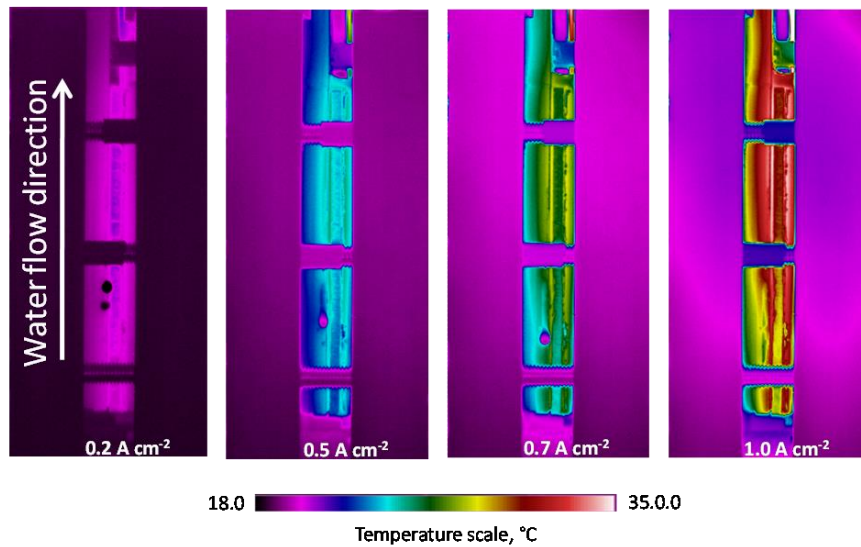
Figure 24 - False colour images of proton exchange membrane under a range of operating conditions.

The results of measurements taken at points one to six as indicated

by P_1 etc. is shown in Figure 25.
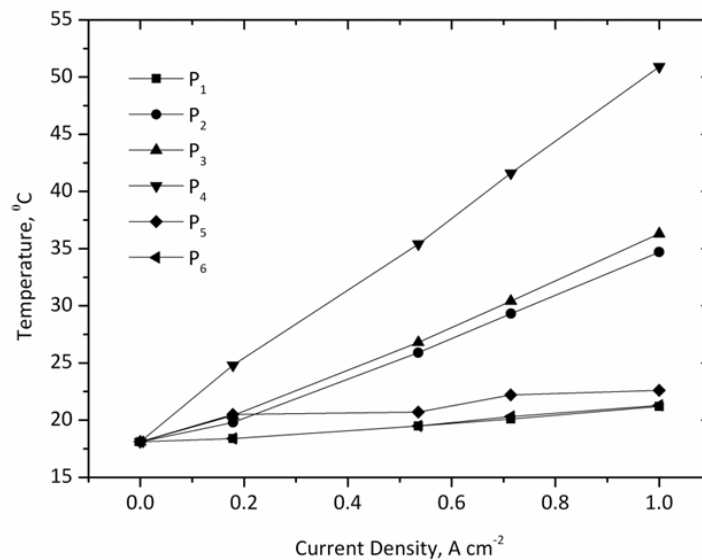
Figure 25 - Effect of current density on the temperature of PEM electrolysers with points shown as indicated in Figure 23.

Initially all temperatures are the same due to emissive corrections discussed previously; however, it is seen that P$_4$, which is located on the graphite flow field of the plate, shows the highest rise in temperature. This result is due to the fact that the plate has the highest thermal conductivity, and lowest heat capacity of the materials in the cell. This correction highlights the vital role obtaining accurate emissivity measurements plays in calculating absolute temperatures; and also the ease with which errors can be made should an operator fail to take account of this correction.

Under certain circumstances the emissivity of surfaces can be altered to improve imaging and obtain a uniform surface emissivity. When highly reflective surfaces were imaged the surface was coated with a matte black paint; this treatment can also aid the rejection of unwanted surface reflections. Once more a calibration curve can be generated using a thermocouple at a range of temperatures to quantify the emissivity over the range of temperatures expected.

A quasi-blackbody can also be used for the estimation of emissivity. In this case a long, thin cavity in the surface can be used to give the temperature of the object. In the course of this work quasi-blackbodies have been used to calculate apparent emissivity ($\varepsilon_{apparent}$) with a minimum aspect ratio of 1:7. The effect of the aspect ratio is shown in as calculated using a modified version of

Equation 30 [51] which details Gouffé's theory of blackbody cavities. This theory postulates that the apparent emissivity of the cavity ($\varepsilon_{apparent}$) can be related to the emissivity of the material which forms the wall of the cavity (ε_{wall}) through a relationship between the surface area of the aperture (s), the interior surface of the cavity (S) and that of a sphere which would have the same diameter as the depth of the cavity (S_0). Whilst these measurements are not facile to conduct in real life, Figure 26 shows that for a material of reasonable emissivity ($\varepsilon > 0.7$), any aspect ratio greater than approximately 1:5 yields sufficiently accurate results so as to be considered a quasi-blackbody.

$$\varepsilon_{apparent} = \frac{\varepsilon_{wall}(1 - \varepsilon_{wall})}{\varepsilon_{wall}\left(1 - \frac{s}{S}\right) + \frac{s}{S}} \cdot \left[\frac{s}{S} - \frac{s}{S_0}\right]$$

(30) Apparent emissivity of a cavity blackbody calculated using the geometry of the cavity
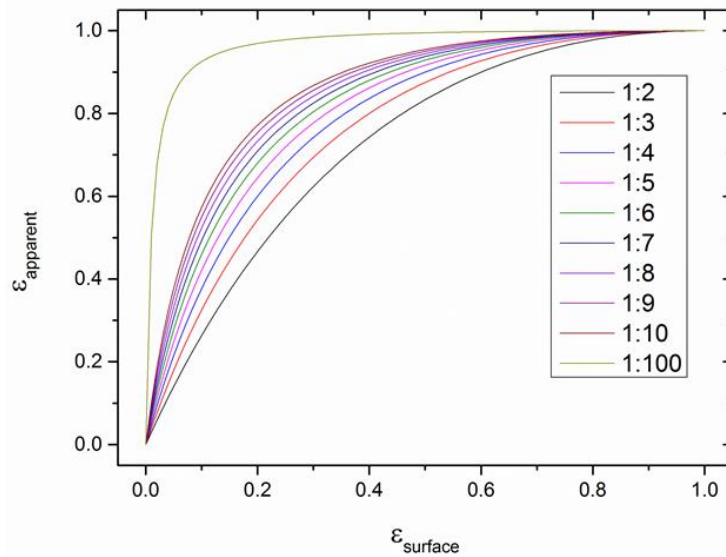
Figure 26 - The effect of the cavity aspect ratio and surface emissivity on the apparent emissivity observed using a cavity blackbody.

3. Focussing and programming of the camera

Focussing of the camera was typically performed using an automatic focussing protocol in Altair; however, this was not always sufficient in focussing on the desired surface. The edges present in images were obtained using the inbuilt 'edge finding' filter, as shown in Figure 27(a). This edge finding algorithm enables the features of a surface to be clearly identified, eliminating the effect of 'thermal spreading' and 'hot-spot' type behaviour as seen in Figure 27(b). Once the relevant edges were identified manual focussing was then performed in order to maximise the image quality and pixel resolution for all images. The pixel resolution, which is dependent on the geometry of the imaging scenario, is a measure of the spatial resolution of the thermal maps obtained.
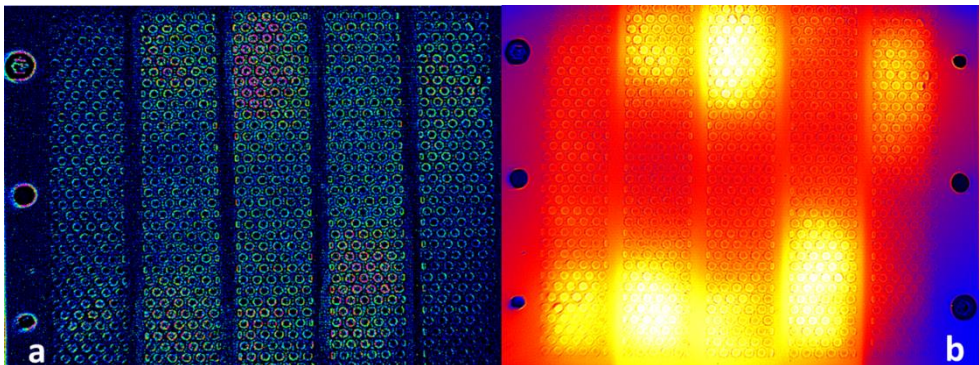
Figure 27 - a) Example of focussed image obtained using find edges filter; b) Image with filter removed showing thermal distribution in an open-cathode PEMFC.

Once the images were accurately focussed and calibrated, the camera was programmed in order to minimise data storage requirements. This was performed based on the speed of the

processes being investigated. While a frame rate of 25 Hz was commonly used, certain processes (for instance lock-in thermography and electro-thermal impedance spectroscopy) required framerates approaching 100 Hz. In contrast, long duration experiments (such as those detailed in Chapter 5) exhibited slow thermal dynamics enabling reduced framerates to be used. Typically a 1 min recording at 25 Hz produced a 1 GB file, with higher framerates increasing this data requirement.

3.1.2 Electrochemical Impedance Spectroscopy

Electrochemical impedance spectroscopy (EIS) is an AC diagnostic technique commonly used in the analysis of electrochemical devices. The distinction between electrical resistance and impedance is subtle but crucial, namely, resistance does not account for any time dependencies [12], thus cannot be used to describe an oscillating current, which is time dependent. EIS is performed by imposing a sinusoidal oscillation on either the voltage (potentiostatic operation) or the current (galvanostatic operation) and measuring the resultant oscillation in either the current or voltage respectively as seen in Figure 28.

In performing EIS it is imperative that the technique does not disturb the steady-state nature of the system, thus a small perturbation must

be used. The mathematical description of this technique (performed potentiostatically) is outlined in Equation 31.
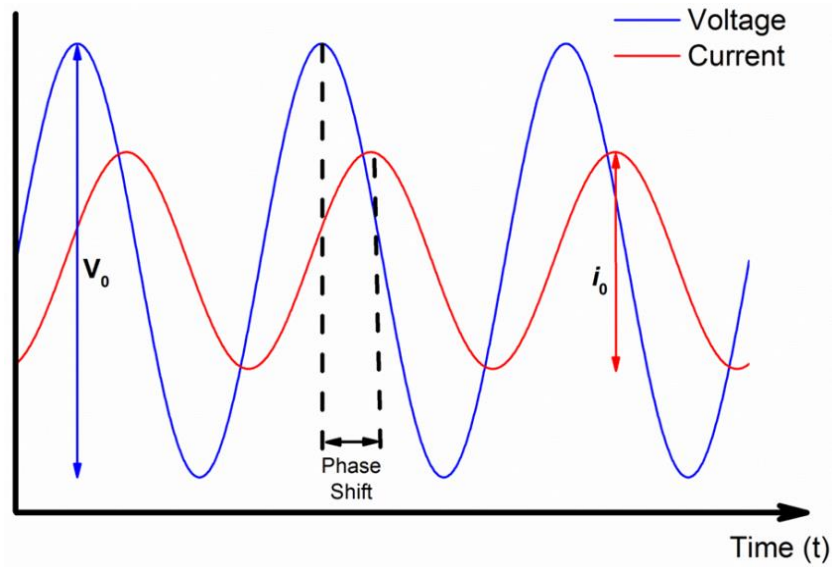
Figure 28 - Typical voltage and current profiles during an electrochemical impedance spectroscopy experiment operated potentiostatically.

Here the transfer function response (Z) which is obtained as a complex number is seen to be the ratio of the Laplace transform of the time dependent voltage (E) and current respectively (I). In turn, these Laplace transforms are obtained by measuring the magnitude of the voltage (E_0) and current (I_0) and the phase shift (ϕ) between the signals at a given frequency (ω).

$$Z(\varpi) = \frac{L[E(t)]}{L[I(t)]} = \frac{E_0}{I_0}\frac{e^{j\omega t}}{e^{j\omega t-\phi}} = \frac{E_0}{I_0}e^{\phi} = \frac{E_0}{I_0}(\cos(\phi) + j\sin(\phi))$$

(31) Mathematical description of electrochemical impedance spectroscopy

When this is performed over a range of frequencies polarisations and electrochemical phenomena can be decoupled according to the respective time constants which govern the processes by identifying the frequency dependent impedance. The results of an EIS study are commonly plotted on a Nyquist plot which charts the real impedance component against the negative of the imaginary impedance component. At all points on a Nyquist plot the magnitude of the impedance can be obtained by measuring the magnitude of a vector from the origin to the relevant point with the phase shift between the stimulus and response signal being the angle between the x-axis and the vector. Typical Nyquist plots are shown in Figure 29 below for both a PEM fuel cell and a Li-ion battery.
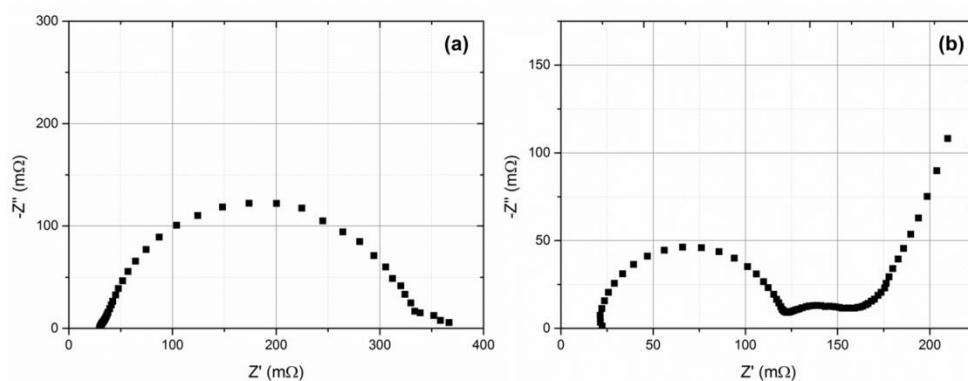
Figure 29 - Nyquist plots showing the EIS characteristics of a) a PEM fuel cell and b) a Li-ion battery.

Once Nyquist plots are obtained it is possible to model the system analysed using a technique known as equivalent circuit modelling demonstrated in Figure 30. This technique utilises a range of fundamental electrical components, including resistors and capacitors, to describe the performance of the system. Fuel cells are

typically modelled using a combination of resistors and capacitors whilst Li-ion batteries can be modelled in a similar way; however, typically an additional element known as a Warburg element is used to account for diffusional limitations associated with the Li-ions.
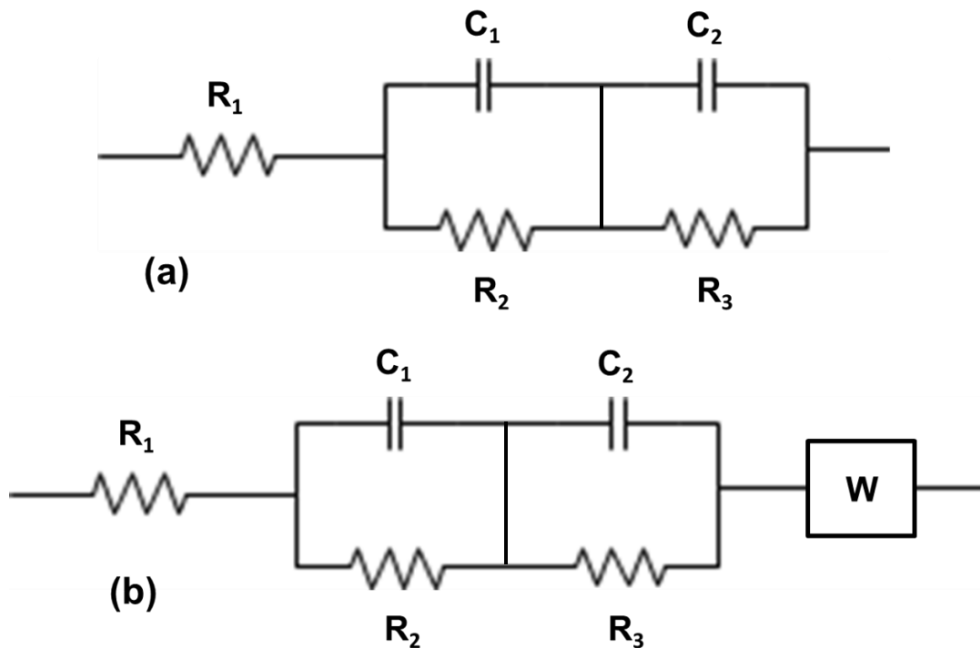
Figure 30 - Equivalent circuits used to model (a) PEM fuel cell and (b) Li-ion battery.

Using equivalent circuit analysis it is possible to quantify the component resistances within the analysed system. The pure Ohmic component of the resistance in the system (which is commonly simply referred to as the resistance) is obtained at a point known as the high frequency intercept. This point occurs at the first intersection of the equivalent circuit with the x-axis and as such has no imaginary component. The resistances, associated with a variety of electronic and transport processes, which occur at lower frequencies can be similarly obtained using this method.

3.1.3 X-ray Diffraction

X-ray diffraction (XRD) is a well described technique which uses X-rays to study crystal structures, either for identification or quantification purposes. This technique relies on the fact that when an X-ray is passed through a crystal it is scattered by the electrons within the crystal structure; these scattered rays then interfere with each other resulting in unique diffraction patterns. These circular diffraction patterns are then quantified according to the intensity of the response obtained using purpose-build detectors. In this work the directionally dependent diffraction pattern has been analysed to obtain structural information pertaining to SOFC anodes. The diffraction patterns obtained are analysed using Braggs Law, shown in Equation 32 which describes the relationship between the wavelength of the incident X-ray photons (λ), spacing between the crystal planes (d) and the angle of incidence of the planes (θ).

$$n\lambda = 2d\sin\theta$$

(32) Braggs law for crystallographic diffraction

By solving Braggs law it is possible to obtain the crystal lattice parameter. In this work, Topas (Bruker, USA) software was used to obtain characteristic bulk lattice parameters for a mixed Ni-YSZ cermet sample. This software requires numerical input of the diffraction pattern obtained in the direction of interest and in turn calculates the unit cell parameters for the sample of interest.

3.1.4 X-ray Computational Tomography

X-ray computed tomography (CT) is a non-destructive technique which can visualise structural properties of a wide range of materials and devices [136] in high resolution. In this work, microscopic CT (μCT) is used to identify the complex structure within a commercial Li-ion cell. The technique relies on variable attenuation of incident X-rays between differing materials, which can be measured using a CCD camera. The rotation of the object within the X-ray beam produces an array of greyscale values known as a sinogram. This is then treated using mathematical transforms based on algorithms most appropriate to the imaging technique to generate two dimensional image 'slices' [136]. By stacking these slices and interpolating between connecting areas of similar attenuation the voxels can in turn be generated enabling the full reconstruction of the sample; enabling the identification of key features and areas of interest.

This computational structure is composed of a number of 3D pixels known as voxels; the size of which determines the resolution of the reconstructed image. The quality of image obtained is dependent on a wide range of contributing factors; including the energy and photon flux of the incident beam, the geometrical properties of the experiment and the pixel resolution of the CCD camera recording the signal [136]. Historically synchrotron radiation has yielded superior

reconstructions; however, increasingly lab based CT is preferred due to simpler access and improved resolution. A number of commercially available programmes have been developed to conduct the reconstruction of the 2D slices. These have also been used to obtain the microstructure of devices to inform finite element analysis; in this work the commercial software Avizo Fire (FEA VSG, France) has been used as detailed in Chapter 4.

3.1.5 Focussed Ion Beam Tomography

Similar to μCT focussed ion beam (FIB) tomography is an imaging technique which enables the computational reconstruction of materials in three dimensions. However; FIB is a destructive technique which involves the physical removal of layers of the sample using an ion beam in order to obtain the reconstruction. This technique involves the combination of scanning electron microscopy (SEM) and ion beam milling in order to obtain sequential images of the sample which can be binarised and reconstructed using similar methods to those employed when analysing CT.

In order to achieve accurate measurement the sample is typically immobilised in a resin; which is then filed to expose the surface of the interest. The sample is then coated in a conductive material before imaging with a SEM. After each image is obtained the sample is milled using the ion beam to a specified depth – it is this depth which

defines the voxel size, and therefore the resolution, of the reconstruction. Once the array of images has been obtained the greyscale SEM images are binarised to separate the respective phases of interest within the sample. At this point the reconstruction can be performed to yield a three dimensional representation of the sample.

While FIB tomography is a destructive technique it offers improved spatial resolution when compared to X-ray techniques, and can also be used to observe phases which have low X-ray attenuation. In this work FIB tomography has been used to elucidate information regarding the microstructure of SOFC anodes to inform finite element analysis of SOFC systems.

4 A Combined Thermal Imaging, X-ray Micro-Tomography and Electrochemical Impedance Approach to Study Li-ion Batteries Under Discharge

4.1 Introduction

Effective operation of Li-ion battery systems requires careful thermal management in order to ensure stable performance, durable operation and prevent thermal runaway which can lead to catastrophic failure [137]. Poorly designed battery packs can also result in significantly reduced volumetric and gravimetric power density; as such, thermal management strategies are amongst the most significant design criteria when developing battery pack systems used in electric vehicles (EVs) and hybrid electric vehicles (HEVs) [41].

The 18650 spiral wound cell is widely used in portable applications, but has also been applied in automotive applications [138]. The design of this cell often incorporates a positive temperature coefficient (PTC) safety device in the battery cap, which demonstrates a large increase in electrical resistance above a certain trigger temperature. When an over-current condition occurs, such as during an electrical short, the high currents cause the PTC to self-heat and enter a high-resistance state acting to limit the current passed and protect the battery and user from adverse consequences

[139]. Although generally an effective safety measure, the incorporation of an additional resistive component acts to increase the internal resistance of the battery (and lower its efficiency) and can generate hazardous temperatures with potential failure leading to fire, causing further damage to the systems which employ such technology. This scenario is a particular risk in the instance of a short circuit of a cell [140].

In addition, localised temperature variations caused by short circuits or internal defects within individual cells may result in 'hot-spots' within battery packs, leading to thermal runaway which can cause catastrophic failure of whole systems [141]. This has been observed in the grounding of the Boeing 787 'Dreamliner' fleet in 2013 due to faults associated with Li-ion battery packs that included two major battery thermal runaway events in 52,000 flight hours [39] and a fire which occurred in a modified Toyota Prius vehicle due to incorrect electrical contacts within Li-ion battery packs [40]. Given the importance of temperature management in the design of Li-ion systems, a range of electrochemical models have been developed to predict thermal behaviour. These models often make assumptions which neglect non-uniform thermal distributions [142] or have only been validated against a single point temperature measurement, typically made using thermocouple/s on or within the battery / pack [143].

Recent modelling efforts have included attempts to incorporate non-uniform resistance distributions within cells and battery packs [144, 145]. These models highlight the importance of thermal management in battery packs and the need for system level experiments. However, the models do not incorporate a PTC element, which will further modify the temperature distribution within packs. In addition, limited experimental validation of the work has been reported, which restricts the use of such models.

Models which fail to take into account the heating effects of external 'non-electrochemical' (Ohmic) heat sources, risk eliminating a significant source of heating in a real battery system, particularly at high discharge rates. External elements may include a mechanical safety valve, a PTC element or metallic contacts. Yi et al. [146] developed a model which accounts for such resistances in a planar Li-ion cell and attests to the importance of characterising these loses.

While much work has gone into producing accurate and robust modelling of Li-ion batteries, experimental validation is required in order to maximise the potential of this area. Discrete thermocouple measurements cannot adequately capture the temporal-spatial dynamics exhibited by batteries and battery packs. The non-invasive nature of thermal imaging, its high temperature resolution and

significantly improved spatial resolution represents a much more accurate and representative measurement of the surface temperature of batteries compared to discrete thermocouples.

Wang et al. [109] used infrared thermal imaging on planar Li-ion batteries; however, the work did not investigate the effect of the discharge rate, nor the effect of spatial location on the temperature of the battery. Kim et al. [107, 108] reported validation of an electrochemical model using infrared techniques; however, the results are presented for only a single discharge rate.

4.2 Experimental Methods

Experiments were carried out on single 18650 spiral wound lithium nickel manganese cobalt oxide (NMC) Li-ion cells (ICR18650S3, 2200 mAh, LG Chem Ltd., Seoul, South Korea) which have a rated maximum discharge current of 4400 mA (2 C). Prior to each test the cell was fully charged to 4.2 V, the maximum rated voltage, first by constant current charging to 4.2 V and a subsequent constant voltage charge at 4.2 V until the current tapered down to 3% of the initial applied current using an electrochemical test station (Maccor 4300, Maccor Inc., Oklahoma, USA) and the manufacturer's recommended charge rate of 0.5 C. Although no significant thermal effects were observed during charging at this rate, the cells were

disconnected from all electrical contacts for a period of 1 hour prior to discharging, to ensure thermal equilibration with ambient temperature. The surface of the battery was coated with a matt black paint to minimise infrared reflections and ensure a uniform emissivity. In order to calculate the emissivity of the coated surface a purpose-built cavity black-body (ε= 0.98) was used [51] prior to conducting all experiments, in addition to a diffuse reflector which eliminates the effects of environmental reflections.

The geometry of the experimental setup as shown schematically in Figure 31 resulted in a spatial resolution of ~0.1 mm using the infrared camera with the images being recorded at a frequency of 1 Hz in order to reduce data storage requirements. Discharging of the battery was conducted using a potentiostat (IviumStat, Ivium Technologies, NL) at varying C-rates within the safe discharge regime according to the cell manufacturer.
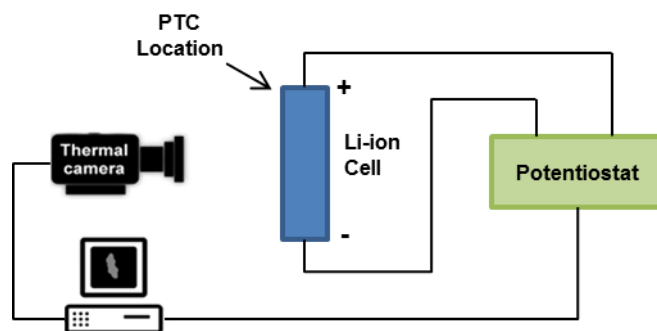
Figure 31 Experimental configuration highlighting the thermal imaging camera, potentiostat and 18650 Li-ion cell used in all experiments

Potentiostatic Electrochemical Impedance Spectroscopy (EIS) was conducted from 10 kHz to 1 Hz using a 15 mV AC sinusoidal perturbation, at the open circuit voltage (OCV) to assess whether the resistance associated with the PTC element was increasing due to the higher temperatures within the positive terminal. An environmental chamber was used to assess the effect of temperature on the electrochemical impedance response and to determine the onset of increased resistance due to thermal activation of the PTC element. The chamber consisted of a PID controlled electronic heater which enabled the temperature within the enclosure to be controlled to ±1 °C of the desired set point. During the experiments the chamber was allowed to reach thermal equilibrium for a period of no less than 10 minutes prior to experiments to minimise the inherent PID fluctuations in temperature.

In order to ensure the battery was without any structural defects and to determine the assembly and location of internal components X-ray tomography was conducted at the Manchester X-Ray Imaging Facility at Harwell. Tomography scans of the positive terminal region and of the full battery were obtained, and subsequent 3D analysis of the reconstructed image data was performed using Avizo software (FEI Company, Oregon, USA). X-ray micro-tomography scans were performed on the battery using a Phoenix v|tome|x system (Phoenix X-ray, GE Measurement and Control, Germany). The battery was

rotated 360° about its long axis whilst 1000 projections were captured with the nanofocus tube operating at 100 kV and 270 μA. The sample and detector were positioned in projection magnification providing an effective pixel size of 8.94 μm for the high resolution imaging

4.3   Results

4.3.1   X-Ray Microtomography

In order to associate external measures of temperature with internal heat generation sources, an understanding of the internal structure of the battery is a prerequisite. While the 18650 (18 mm diameter, 65 mm high) battery is a widely used standard, the internal configuration can vary between manufacturer and internal defects can arise due to manufacturing tolerances and material processing variability. Disassembly of a battery is both a hazardous and destructive process; in contrast, X-ray tomography has been shown to be a powerful, non-destructive tool for the characterisation of the structure of electrodes, single cells and devices [147-149]. Figure 32 shows a 3D rendering of the tomographic data set for the 18650 cell. The spirally wound internal structure of the cell, separator material (identifiable by the white concentric circles) and hollow central section, are visible in Figure 32(b).
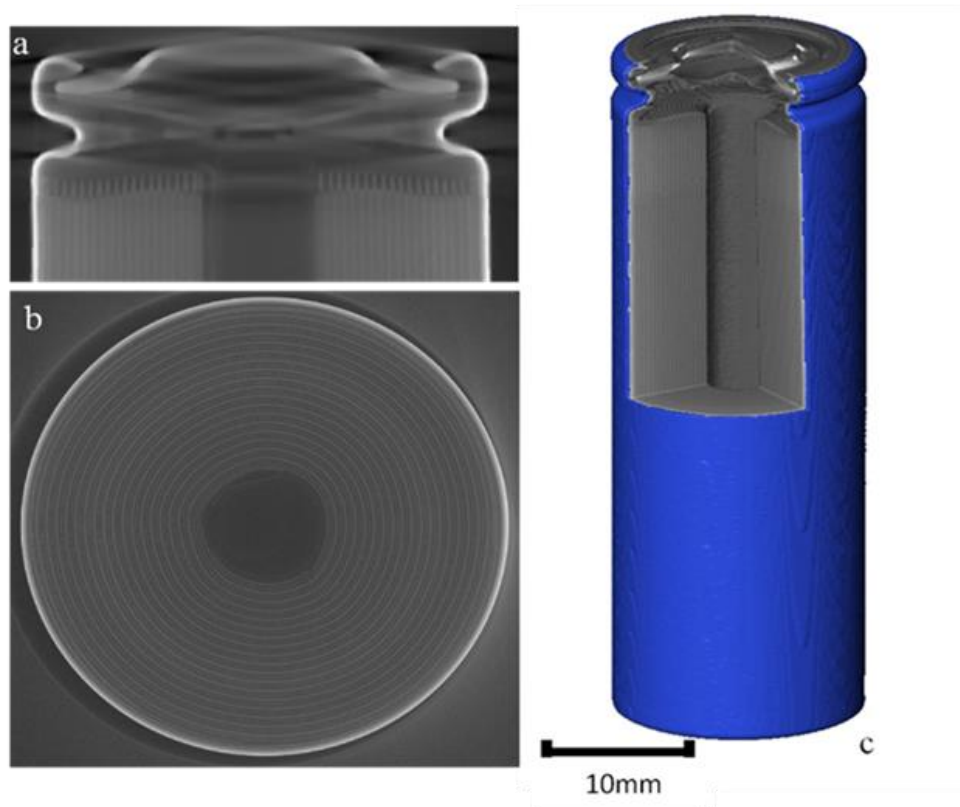
Figure 32 - 3D rendering showing: a) the safety valve assembly in the battery cap, b) a magnified cross section of the battery showing the electrode assembly and hollow centre, and c) a magnified longitudinal slice of the battery.

No macro-structural defects were observed within the cell, which could give rise to undesirable sources of heat. The X-ray microtomography also enabled a reconstruction of the battery cap architecture (Figure 33), including the valve, PTC and positive electrode terminal.
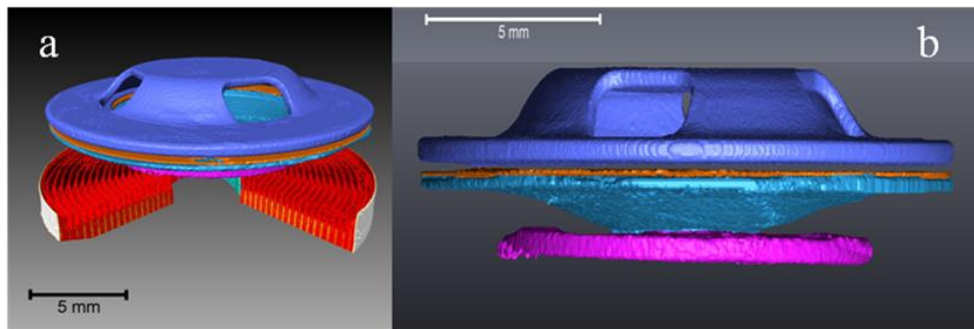
Figure 33 - 3D reconstruction showing: a) auxiliary view of the safety valve area highlighting the positive electrode contactor (purple), PTC element (orange) and safety valve (turquoise); b) orthographic view of the positive terminal area. The tomographic reconstructions show the tightly packed nature of the positive terminal area. The entire battery cap (terminal and safety componentry) is ~5 mm in height.

4.3.2 Infrared Imaging

Infrared imaging was conducted while the battery was discharged at a range of discharge rates, ranging from C/10 to 2 C. Average battery temperatures rose with time during discharge as a result of heat generation associated with reaction and Joule heating, with significant spatial variations observed along the length of the battery. The local temperature along the central-line of the battery was captured, as indicated in the inset in Figure 34, with local temperature deviations from ambient as a function of time and discharge rate plotted in Figure 34.
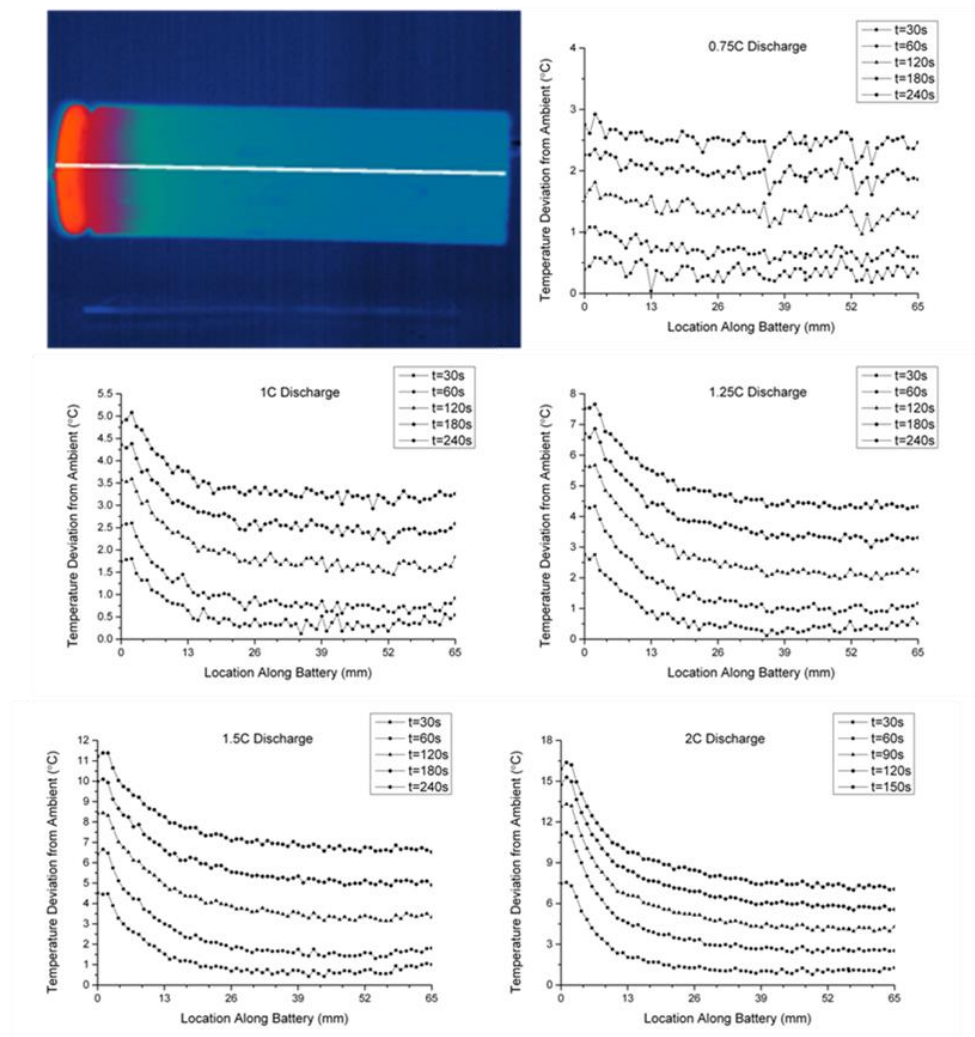
Figure 34 - Axial line of measurement and temperature deviation distributions as a function of location along battery and time (in seconds) during 0.75 C--2 C discharge.

The temperature profile during discharge was similar in all cases from C/10 to 0.75 C; namely no significant gradient was observed. At discharge rates higher than 1 C an area of increased temperature is identifiable 0 mm – 4 mm from the positive terminal of the battery. This area corresponds to the battery cap, as identified by the X-ray tomography. The temperature at the surface of the battery cap is seen to be larger than that along the body of the battery purely due to the discharging process; this implies a higher rate of heat generation

at the positive terminal than in the bulk of the battery itself. From the microtomograms it can be deduced that this increased rate of heat generation is attributable to the battery terminal area due to its non-uniform nature and multi-component construction.

By comparing the temperature rise at both terminals it can be concluded that the contact resistance with the external current collector does not contribute greatly to the temperature variation. This is particularly evident for the 1C – 2C discharge rates, during which a significant temperature gradient is observed close to the positive terminal but with no similar gradient appearing at the negative terminal. This implies that the battery cap provides a significantly higher resistance to current flow; resulting in the increased heat generation and corresponding temperature rise. It has been reported that safety valves used within Li-ion batteries are either composed of an aluminium or aluminium/polymer structure [150], the bulk material will not add significantly to the resistance of the cell due to the high electrical conductivity of these materials. It is therefore proposed that the contact resistance between components in the cap and the PTC element provides sufficient resistance to cause the temperature variations observed.

As PTC elements are designed to be activated (resulting in an increase in electrical resistance) at elevated temperatures, it is

important to consider not only surface temperature but also internal temperature, which may vary considerably from that measured at the surface [151]. It is evident from Figure 34 that, for discharge rates of 1C and above, increasing current leads to a higher temperature gradient close to the positive terminal of the battery. However, the temperature profile itself does not change appreciably with time at each discharge current, with a relatively uniform increase in temperature observed along the length of the cell.

The temperature heterogeneity highlighted above is particularly relevant to the positioning of thermocouples in battery packs. If the thermocouple is located towards the negative terminal of a battery the error in measuring the peak temperature of the cell may be particularly large; something which when incorporated into a battery pack may have severe consequences. The fact that cells are typically uniformly aligned within battery packs will tend to create an area of high heat output at the positive terminal current collector.

In addition to examining the axial temperature distribution, the radial surface hoop circle distribution within cylindrical Li-ion cells was also investigated. It can be seen in Figure 35 that provided the current collectors are positioned in the centre of the electrode terminal, there is no significant radial variation in thermal variation around the cell housing.
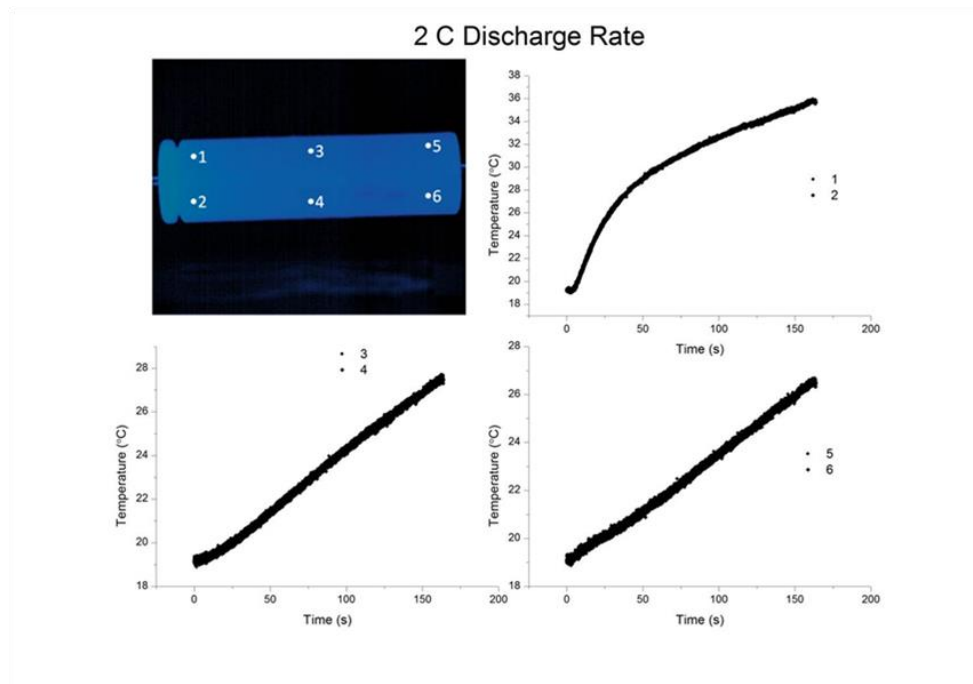
Figure 35 - Transient temperature response at different locations along the axis of the battery (30 mm approx. between each point axially, 5 mm approx. between each point radially along the surface hoop circle) at a 2 C discharge rate.

However, poor electrical contact can lead to heterogeneity in the radial temperature distribution and additional heating at the electrode terminals. For example, Figure 36 shows the case of an acentric current collector pin at the negative electrode terminal the poor mechanical coupling (caused by a low clamping force) leads to localised Joule heating and the acentric connection leads to heating from the point of contact causing a radially non-uniform heat distribution. This effect is also observed at the positive terminal; however, due to the magnitude of the heating in this region the effect is less pronounced than at the negative terminal. These effects manifest themselves in highly non-uniform temperature gradients

across the battery surface and further add to the limitations of not including non-electrochemical elements and appropriate external resistances when modelling battery temperatures.
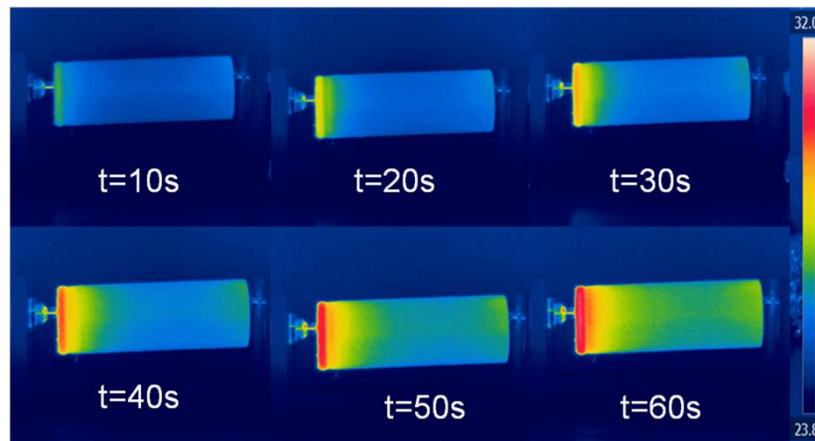
Figure 36 - Effect of acentric current collection from a pin current collector on the positive (left hand side) and negative (right hand side) electrode during a discharge at a rate of 2 C during a 60 second period.

Electrochemical impedance spectroscopy was conducted on the cell at various temperatures at OCV in order to decouple the thermal effects on the various loss mechanisms in the battery. The typical EIS response of Li-ion cells is composed of a bulk Ohmic resistance coupled with two overlapping RC arcs corresponding to solid-state resistance and capacitance at high frequencies and charge transfer resistance and the associated double-layer capacitance at intermediate frequencies [152]. In addition, at low frequency a Warburg element accounts for the diffusional limitation associated with the mass transfer of lithium ions between the electrodes and the electrolyte.
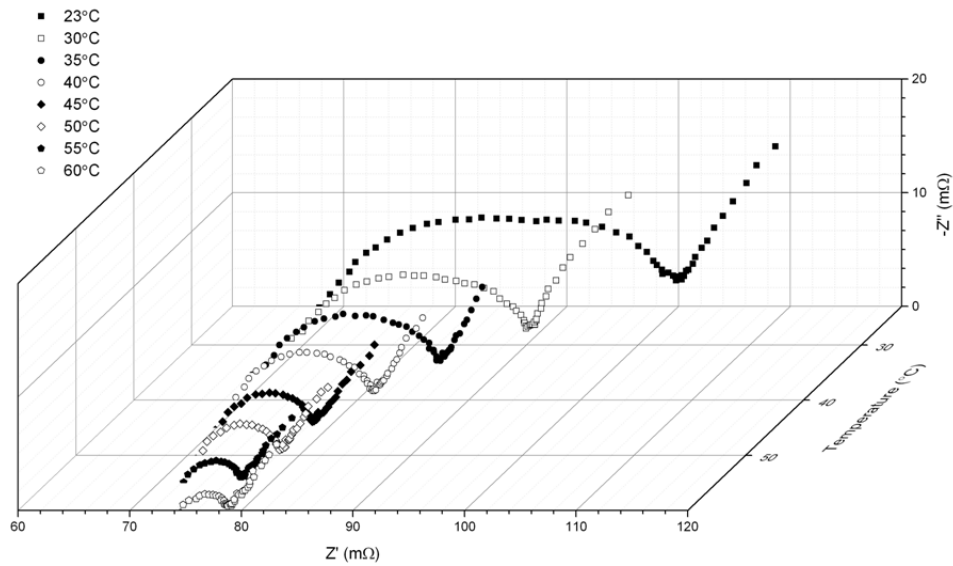
Figure 37 - Effect of temperature on the EIS sweeps at OCV conducted within an environmental chamber over the temperature range of 23–60 °C.

Figure 37 shows the electrochemical impedance response in complex plane (Nyquist plot) form at OCV as a function of temperature. It is not possible to resolve two arcs for all temperatures, either because one of the RC couples is much smaller than the other and/or the time constant for each process is not significantly different; however, an indication of a secondary arc is visible at 20 Hz at a temperature of 23 °C indicating the presence of two time dependent processes. A Warburg impedance feature, typified by a line proceeding at 45° to the real axis, is evident at low frequency (<100 Hz in all cases) in all cases. Nagasubramanian has demonstrated the effects of temperature on 18650 Li-ion cells, showing a reduction in the overall electrochemical impedance with increasing temperature and an approximately stable Ohmic

resistance, given by the high frequency intercept, at temperatures ranging from -20 °C to 40 °C [153]. In agreement with the work of Nagasubramanian, a reduction in the primary arc resistance is observed with increasing temperature up to 60 °C.

The purely Ohmic component (determined from the high-frequency intercept with the real axis) goes through a minimum within the 20–30 °C region of experimentation, as shown in Figure 38. The observed effect of temperature on the Ohmic resistance within the temperature range 20–40 °C is once more in agreement with the results reported by Nagasubramanian [153]; however, above 40 ºC an increase in Ohmic resistance is observed. This increase occurs at a similar temperature to the crossover point between the stable Ohmic resistance of the PTC element and the temperature activated increase as reported by Zhong et al. [154] for LiFePO$_4$ cells.

The EIS data shown in Figure 54 imply that the PTC effect does not contribute to the asymmetric heating of the cell due to increased resistance over the majority of the relevant temperature range in this study (due to the relatively small increase in Ohmic resistance), rather, it is solely the presence of the PTC and safety valve at the positive terminal which drive the heating by a non-uniform distribution of Ohmic resistance within the cell.
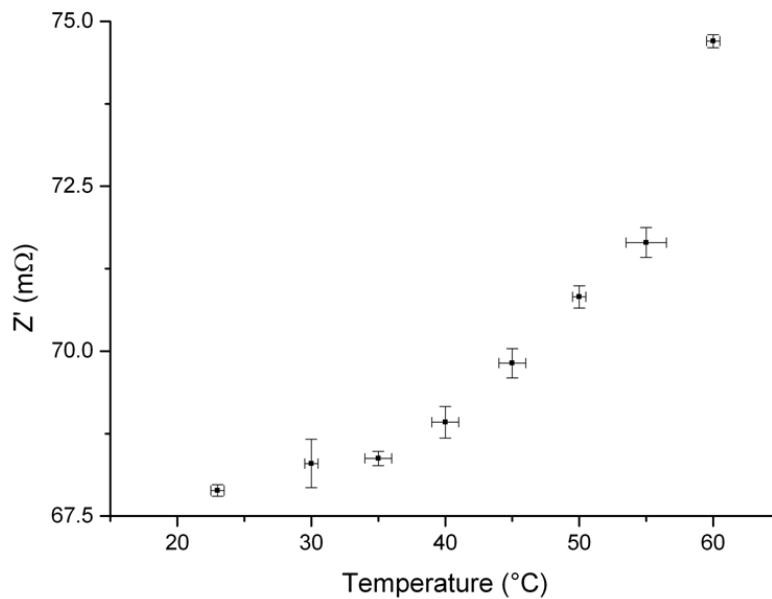
Figure 38 - Effect of temperature upon the location of the high frequency intercept (purely Ohmic resistance) showing the standard deviation of the EIS measurements and the range of temperature fluctuation throughout the duration of the measurement.

4.4 Conclusions

Heterogeneous temperature distribution across the length of a single 18650 Li-ion cell has been observed for discharge rates above 0.75 C, within the standard operating window of the cell. External electrical contact resistances at both terminals can contribute to this at higher current densities; however, the most significant heating effect is observed within the cell at the positive terminal. The high-resolution thermal images show that discrete thermocouples cannot fully capture the thermal profile and the location of placement is

important for safety purposes and should be sited close to the positive cap of the cell.

X-ray microtomography provides a clear picture of the internal structure of the battery and shows that the source of the heating corresponds to the PTC and safety valve assembly. EIS as a function of whole-cell temperature shows that this particular PTC is not activated significantly, if at all, prior to temperatures below 60 °C. Given that the high discharge rates studied (up to 2 C) did not lead to cell temperatures anywhere as high as this, activation of the PTC is not expected to occur. Rather, the heating effect in the positive cap is attributed to the materials and internal contact resistances between the battery roll, PTC and safety valve.

Models must consider spatially allocating the Ohmic resistances within cells in order to give a truly accurate representation of both the thermal and electrochemical effects of the system. In addition, the non-uniform materials of the cell must be accounted for in order to capture the dynamics of battery discharge which have been shown to significantly deviate from a 'quasi' steady-state or uniform thermal distribution assumption often made when producing electro-thermal models. Finite element models that consider the internal structure of the battery must consider the features in the cap and structure of the 'jelly roll' and casing to this end.

5 Combined Thermal Imaging and X-ray Diffraction for Crystallographic Strain Analysis of SOFC Anodes

5.1 Introduction

As previously detailed, the construction of a SOFC involves the combination of layers of a porous ceramic cathode, dense ceramic electrolyte, often yttria stabilised zirconia (YSZ), and a porous cermet anode (typically a Ni–YSZ composite). The incorporation of nickel into the anode is required to catalyse the reduction reaction which occurs at this electrode; specifically at the triple phase boundaries within the structure. Whilst producing this mixture of ceramic and metallic components is essential for effective operation it poses significant challenges due to the wide disparity in the coefficient of thermal expansion (CTE) between the Ni and YSZ as seen in Table 4.

Table 4 Coefficient of thermal expansion of Ni, YSZ and composite Ni/YSZ cermet mixtures at 900 °C.

Material	CTE ($\times 10^{-6}$ m K^{-1})
Ni	19.3 [155]
8 YSZ	9.45 [156]
10 YSZ	9.07 [156]
Ni (15 %) / YSZ	10.40 [157]
Ni (30 %) / YSZ	11.64 [157]
Ni (50 %) / YSZ	13.20 [157]

As seen in Table 4, the amount of Ni incorporated into the cermet material has a significant impact on the bulk thermal expansion coefficient; which is most relevant to interactions between the anode and YSZ electrolyte, the fact that solid Ni is present within the anode will introduce significant CTE inhomogeneity. During any rapid heating in a constrained environment, strains will manifest themselves within the anode, a consideration which will also apply in the presence of temperature variations. In order to mitigate against the issues instigated by the CTE mismatch it is common to limit the rate of heating and cooling and to attempt to operate the cells under isothermal conditions; however, this is often impractical and indeed may not be possible.

Temperature variations in SOFCs can arise due to a wide range of conditions including simply heating and cooling, to and from operating conditions [158] and under operation due to localised electrochemical reactions [159] within a cell. Due to the high operating temperatures required to optimise the performance of cells, the balance-of-plant can be greatly increased by the requirement to minimise thermal heterogeneities. This need is present in order to reduce the prospect of thermally induced failure, due to delamination [160] or cell cracking [161], and to prolong the stack lifetime. Finite element analysis (FEA) has indicated that thermal gradients of the order of 10^4 K m^{-1} may exist under internal reforming conditions [68]

and that gradients drastically increase the prospects of cell failure [162] by causing stress gradients across the cell. Indeed, finite element models also predict the presence of temperature variations under steady state conditions [163-165] resulting in thermally derived stress gradients. Limited reports of experimental procedures investigating the effect of temperature variations in operating SOFCs exist; however, it has been reported that large temperature gradients and localised hot spots are observed due to internal reforming on small form factor SOFCs [166, 167].

The mechanical failure of SOFCs has been attributed to the compound nature of the membrane electrode assembly, which results in stresses being generated between the component layers [159, 168-170]. In addition to these, the presence of temperature variations during the heating / cooling phases has also been reported as being a significant cause of failure in SOFCs. While stresses are also generated in the formation steps during the production of SOFCs the coefficient of thermal expansion (CTE) mismatch has been widely reported to be the main cause of thermomechanical failure of SOFCs [171, 172]. Stresses derived in the production of cells arise from the sintering of layers and as a result of a volume change of approximately 41 % when reducing NiO to Ni [173] (with a volume change of approximately 69 % observed in the oxidation step [173]). The residual stresses imposed during sintering can have an

impact upon stresses observed in the operation of the cell; however, they can be relieved through a heating cycle [174]. Additionally, as the cathode typically exhibits both a low stiffness and a similar CTE to the electrolyte, the effect of CTE mismatch is largely observed only within the anode and at the anode / electrolyte interface [174]. This CTE mismatch can generate internal stresses that are often sufficient to cause local internal damage or even complete fracture or delamination [158, 159, 162, 168-170, 175]. This stress cannot be measured by conventional techniques and therefore are poorly understood [176]. As a result, a significant quantity of the literature is devoted to FEA which has been conducted to predict the effects of cell treatment (i.e. redox cycling) and operation. Lin *et al.* [168] investigated the effect of stacking SOFCs, concluding that the CTE mismatch between seals and interconnects impacted significantly on the stresses experienced by the cells. The modelling conducted in this study also indicated that temperature variations were unavoidable due to the nature of operation of the cell. It has also been reported that the layer which experiences the most significant stresses is the anode [159] due to the thickness of this layer within the commonly used anode supported cell.

These problems are not unique to SOFCs, temperature variations are known to promote failure in a range of cermet materials; for example, thermal barrier coatings [177], which are used in a range of

applications including gas turbines [178] and automotive components [179].

In order to improve the understanding of the composite structures discussed, internal stress distributions and internal fracture processes need to be studied non-destructively and *in situ*. Synchrotrons provide ideal locations for the study of such materials due to the flexible nature of many beamlines which enable *in situ* measurements via integrated furnace designs. Additionally, the high resolution measurements available enable internal changes in lattice structure to be measured with high spatial and temporal accuracy.

To date a limited number of experiments on the utilisation of X-ray diffraction of operationally relevant SOFCs have been reported. Villanova *et al.* [175, 180] have utilised synchrotron sources to identify residual stresses within SOFCs, while Sumi *et al.* [181] and Tanaka et al. [182] have also measured the effect of redox cycling on the internal stresses in anode supported Ni / ScSZ SOFCs. In addition to this, synchrotron radiation has been used to conduct high resolution tomography to analyse the internal microstructure of SOFC anodes [21, 22, 183]. X-ray diffraction using lab sources has also been performed in order to investigate the effects of reduction on the stresses within anodes. Wolf *et al.* [184] studied the redox

cycling of anodes and indicated that the 40 % volume contraction previously discussed resulted in significant tensile stress within the anode. Focused ion beam tomography has also been utilised in order to conduct microstructural stress analysis on SOFC anodes [185]; this work indicated that the stresses experienced by the Ni phase within the anode exceeded the yield strength, resulting in plastic deformation at temperatures approaching 800 °C. Recently, measurement of crystallographic strain induced by temperature variations has been achieved using infrared lamp heat sources with measurements using thermocouple arrays [186, 187].

The work detailed in the following section represents the first time a combined X-ray diffraction and infrared imaging study has been performed. To conduct this work a novel furnace was designed [132] to enable high resolution synchrotron data to be collected with the simultaneous recording of spatially resolved temperature data. In addition, the use of infrared imaging enables non-contact, direct surface measurement; eliminating the possibility of thermocouple arrays, required to record spatially resolved thermal data, acting as heat sinks, while also simplifying the design of the experiment.

This method enables the investigation of the effect of one-dimensional temperature variations by sub-dividing the sample into a range of isotherms and analysing the effect of temperature variations

upon lattice parameters within a sample; in this case a composite Ni / YSZ SOFC electrode.

5.2   Experimental Design and Construction

Commercially available anode supported planar NiO / YSZ bilayer button cells (AEB-2.7, Fuel Cell Materials, Ohio, USA) were prepared by laser cutting into individual square tokens of side 10 mm (Laser Micromachining Ltd., Denbighshire, United Kingdom). The cell was constructed of a 6-10 μm layer of YSZ-8 electrolyte on a 220-260 μm NiO / YSZ anode layer. Prior to performing the experiment the cells were reduced from their green NiO / YSZ state to a dark grey Ni / YSZ in a tubular furnace.   Before reduction a flow of N_2 (500 mL min^{-1}) was placed through the furnace for 2 hours to ensure no oxygen was present in the tube, the furnace was subsequently heated at a rate of 5 °C min^{-1} until the desired heating set point of at 600°C was reached.   At this point a flow of 10 % H_2 in N_2 was initiated and maintained for 3 hours to ensure total reduction of the sample, which was subsequently checked using the diffraction patterns obtained at the beamline.

5.2.1 Furnace Design and Temperature Control

To conduct the experiment at relevant SOFC operating temperatures, a novel furnace was designed which enabled concurrent thermal imaging and diffraction data to be obtained. The furnace was purpose built to couple with the sample stage located in the beamline I-12 (JEEP) experimental room at Diamond [188] and is shown in Figure 39. The SOFC half-cell samples were heated using an Inconel sample stage, which was heated by three PID controlled 225 W cartridge heaters (CIR-10121 / 240V, Omega Engineering Inc., Connecticut, USA) which were individually programmable. The heaters were placed into recesses machined into the stage (as seen in (c)) with control thermocouples placed within 2 mm of each heater. To achieve sufficiently high, and stable, temperatures for the duration of each scan the heaters were operated both in series and parallel. The heating stage was placed upon a thin (*ca.* 5 mm) pyrophyllite insulating platform which limited the rate of conduction to the external furnace housing and the sample stage.
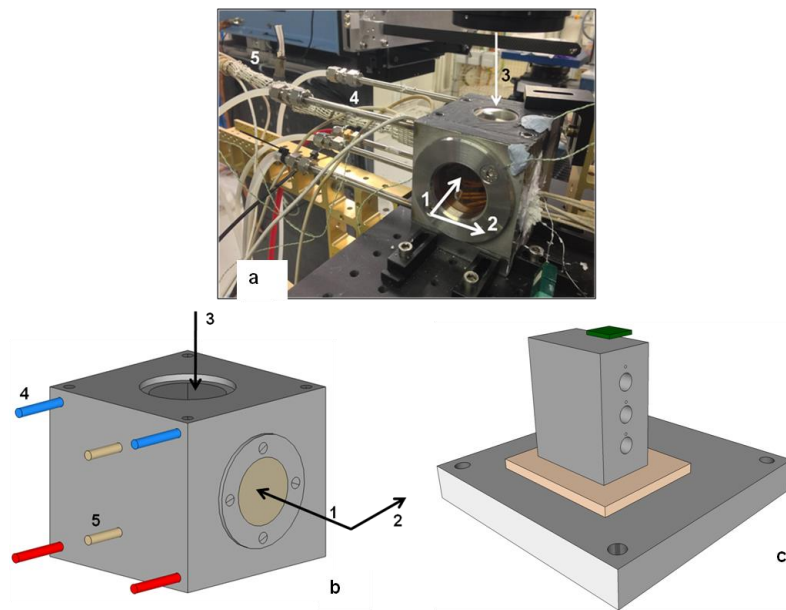
Figure 39 - Image (a) and schematic (b) of the furnace enclosure highlighting: 1) the beam direction and 2) the scan direction in the vicinity of the beamside Kapton window. The IR imaging direction is given by the arrow located at 3, with the external portion of the cooling circuit and gas preheating line located at 4 and 5 respectively. c) Shows the internal furnace stage with insert for 3 × 225 W cartridge heaters, and ceramic insulator.

The furnace enclosure was composed of two Inconel sections – the first an Inconel base which was bolted to the sample stage upon which a second Inconel shell was mounted enclosing the heating stage. The base was designed so that a recess enabled simple alignment of the pyrophyllite insulating layer and heating stage. The furnace enclosure contained two removable Kapton windows for X-ray transmission (arrow 1) and a recess for infrared imaging (arrow 3), into which a high temperature IR transparent CaF_2 window was placed (Z267589-1EA, Sigma Aldrich, St. Louis, USA). Translations in all directions (x, y, z, θ) were achieved using the primary beamline stage. By also mounting the infrared camera to this stage a fixed relationship was defined between the thermal measurements, the

sample and the diffraction scan points throughout all experiments. This enabled spatial relationships to be inferred between all of the data collected during the post processing of the results.

Temperature variations were achieved by overhanging the sample on the edge of the heating stage. Gradients were observed to be isothermal in the beam path with gradients observed along the scan path as indicated in Figure 40. To ensure the Kapton windows were not damaged by the high temperatures generated in the furnace a cooling water loop was incorporated into the shell. The cooling system consisted of two ¼" parallel streams of chilled water that passed through the shell of the furnace body and around the Kapton windows; the coolant was recycled through a chiller via Swagelok connections. In doing this, the temperatures of the Kapton windows, which were measured using K-type thermocouples, were kept below 100 °C at all times ensuring the windows did not degrade or melt.
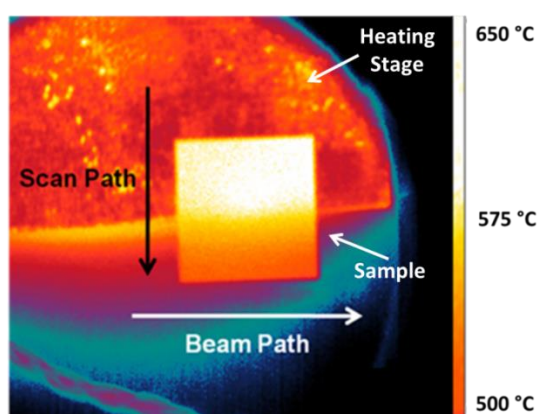
Figure 40 - Direction of the beam and scan shown with an example of a false colour thermal image highlighting gradients using a 256 shade colour-map. Note the temperature range displayed in the image has been scaled to identify the absolute temperature of the sample.

A forming gas mixture of 4% H_2 in N_2 was passed over the samples at all times at a rate of 80 mL min^{-1} to ensure no oxidation of the Ni within the samples; trace signals of NiO were obtained from the diffraction patterns, these however, were found to be constant throughout the experiment, indicating no oxidation of the sample occurred. The forming gas was preheated to over 250 °C using an inline heater in order to maintain a high ambient temperature within the furnace and consequently to reduce the duty of each cartridge heater. The furnace and gas lines were also insulated to minimise heat losses. In addition to the three thermocouples used for the PID control of the heating stage a further four K-type thermocouples were located throughout the furnace to monitor the temperatures of the external surfaces for safety purposes.

Both the emissivity of the sample and transmittivity of the window were obtained by calibrating the thermal imaging results with readings obtained from a thermocouple located on the surface of the sample. This was imperative due to the wide range of temperatures observed, and the potential for both emissivity and transmittivity changes of the sample and window respectively. This calibration involved relating the temperature of both the control thermocouples and the sample thermocouple to the output of the camera. In all cases it was found that the combined emissivity and transmittivity of the sample and window were in excess of 0.9, leading to highly

accurate infrared results. In order to aid the exclusion of external sources of infrared, the surface of the furnace was painted in a matte black paint leading to the external steel having an emissivity in excess of 0.98.

5.2.2   X-ray Diffraction: Calibration and Alignment

All X-ray diffraction experiments were conducted at beamline I12 at the Diamond Light Source. This beamline, which has a useful X-ray spectrum in the range 53–150 keV, was chosen due to the ability to couple the sample stage with *in situ* sample environments while also capturing high quality diffraction data [189]. During all experiments a monochromatic beam with an energy of 80 keV was used. A Thales detector (Pixium RF4343, Thales Electron Devices S.A., France) was used throughout the experiment. The detector consists of a CsI scintillator on an amorphous Si substrate and has a pixel size of 148 μm. Images were recorded with an exposure time of 80 s in order to ensure adequate count levels which resulted in a total scan time of approximately 30 minutes for each experiment. In total, 20 exposures were collected during each scan, resulting an exposure frequency along the sample of 2 mm^{-1}. Prior to each sample being imaged, the imaging system was calibrated using a CeO_2 sample, this was located at a position which reflected the location of the sample to be imaged. A schematic of beamline I12 is shown in

Figure 41, illustrating the location of the major imaging equipment and imaging stage.
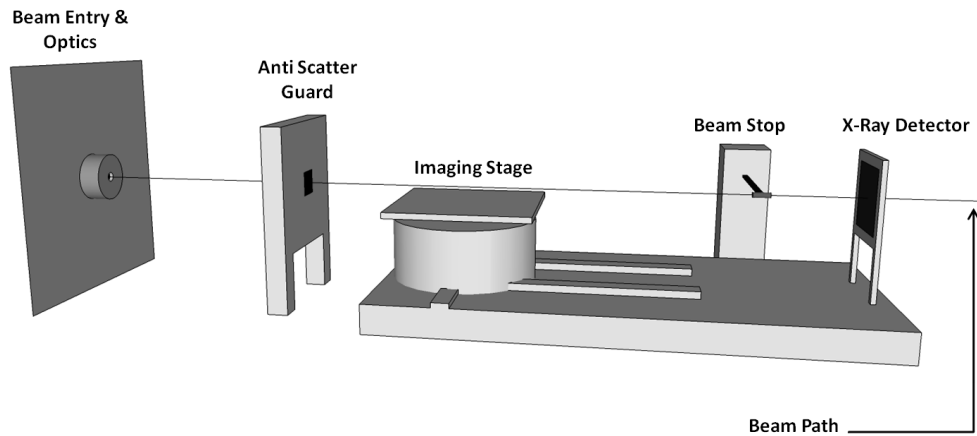
Figure 41 - A schematic of the I-12 beamline highlighting the location of the major equipment within the experimental hutch.

Once the sample was placed within the furnace, coarse image alignment was performed using X-ray radiography, and the sample position was registered with the thermal camera in order to relate the scan location and thermal imaging pixel locations. After a coarse alignment was achieved, a second alignment was performed via X-ray diffraction. As the sample was placed upon the Inconel heating stage the third and fourth quadrants of the diffraction pattern were shielded from the detector. This increased the requirement for the sample to be flat along the length of the heating stage, to avoid masking of the diffraction patterns in the useable quadrants; therefore, alignment in all orientations was performed prior to all experiments. The X-ray diffraction was recorded using a 50 µm beam aligned along the interface of the SOFC anode and electrolyte.

The size of the beam was sufficient to ensure the anode/electrolyte interface was analysed at all times, the beam position relevant to the sample was confirmed using radiography.

In performing the simultaneous thermal imaging the camera was calibrated for two major temperature ranges, 15 – 250 °C and 250 – 1500 °C, which were in turn reduced to a suitable range of expected temperatures for the individual experiments. The camera was fixed to the sample stage, ensuring a defined orientation relative to the sample heating stage at all times, this was in turn used as an alignment guide in the initial placing of the sample. The optical set-up of the thermal camera resulted in a fixed pixel resolution of 74 μm. This fixed working distance configuration resulted in approximately seven resolvable temperature distributions being captured for each single diffraction scan point. Infrared images were recorded at 20 s intervals to minimise data storage requirements, the thermal variatons used throughout the study were as a result of the average of these individual recordings for the full duration of each experiment. The combined emissivity and transmittivity of the window and sample was corrected for each experiment; however, these were largely similar, with slight variations observed as a result of window fouling.

5.3 Effect of Temperature Variations on the Crystallographic Strain in SOFC Anodes

The nature of the experimental design of the furnace enabled high resolution simultaneous thermal imaging and X-ray diffraction; the use of thermal imaging also significantly simplifies and improves the measurement of temperature variations. Figure 42(a) shows a sample thermal image obtained at a nominal temperature of 640 °C as determined by the control thermocouples. This nominal temperature, which describes the temperature of the sample in the isothermal region prior to the onset of the temperature variation, was obtained by the temperature measured by the control thermocouple within the heating stage. Figure 42(b) also shows thermal gradients obtained by processing the raw infrared images obtained during the experiment; these represent the average variation observed throughout the length of each experiment (typically 30 mins in duration).
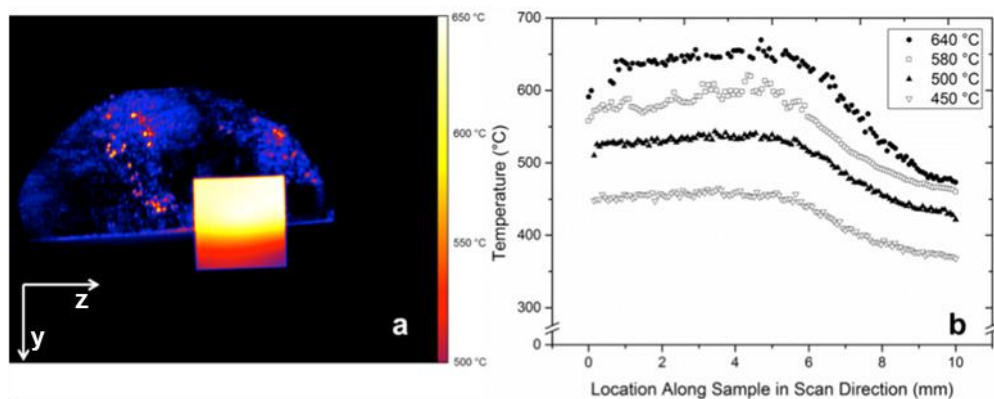
Figure 42 - a) Sample infrared thermal image recorded at a nominal temperature of 600 °C. b) Temperature variations acquired from thermal

imaging averaged across the length of the sample and the full duration of the scans for four nominal temperatures.

Figure 42(a) shows a top down view of the sample, describing the x-z plane with a large temperature variation visible in one dimension along the y-axis of the sample; this corresponds to the scan raster direction. By contrast, isotherms are seen to run along the z-axis of the sample corresponding to the direction of the incident X-ray beam. Due to the thickness of the sample, it was assumed that there was no temperature variation through the sample along the x-z plane. These isotherms enable accurate XRD analysis as all results were obtained in transmission by integrating the results throughout the thickness of the sample. The temperature variations, as seen in (b), correspond with thermal gradients of approximately 10^4 K m^{-1} which have been previously reported during internal reforming conditions in SOFCs [68].

Figure 43 shows a schematic of the sample during the experiments detailing the relative orientations of the temperature variations, scan directions and lattice parameter orientations analysed. This diagram highlights the impact of the temperature variation upon the Ni lattice parameters analysed. Due to the orientation of the sample with respect to the X-ray beam the 90° lattice parameter is vertically perpendicular to the incident X-rays (along the x-axis) with the 180° lattice parameter being horizontally perpendicular to the X-ray beam

(along the y-axis). Additionally the temperature variation is considered solely one dimensional (due to the thin sample) and horizontally perpendicular to the incident X-ray beam (along the y-axis and therefore parallel to the 180° Ni lattice parameter).
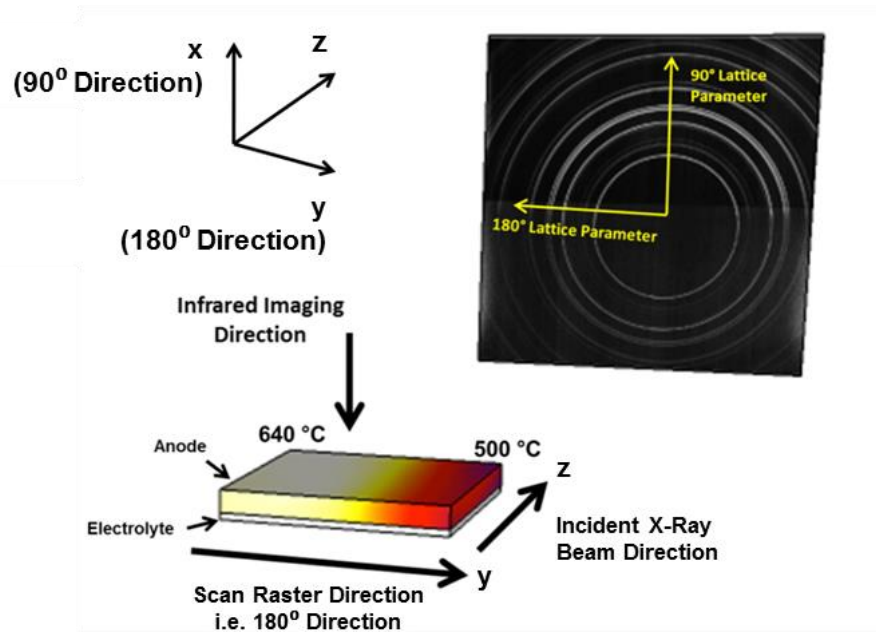
Figure 43 - Schematic of the Ni / YSZ half-cell indicating the direction of the incident X-ray beam, the scan raster direction, the imposed temperature variation and the orientation of the infrared thermal imaging. Also shown is the direction of the 90° and 180° Ni lattice parameters which were used for all analysis.

As a result of the geometric orientation of the experiment the 90° lattice parameter measurements can be considered discrete points perpendicular to the temperature variation along vertical isotherms, and thus unaffected by the temperature variation. In contrast, the 180° lattice parameters are discrete points parallel to the temperature variation and thus are strongly affected by the presence of the

variation due to it acting across the length of the X-ray measurement area of 50 μm.
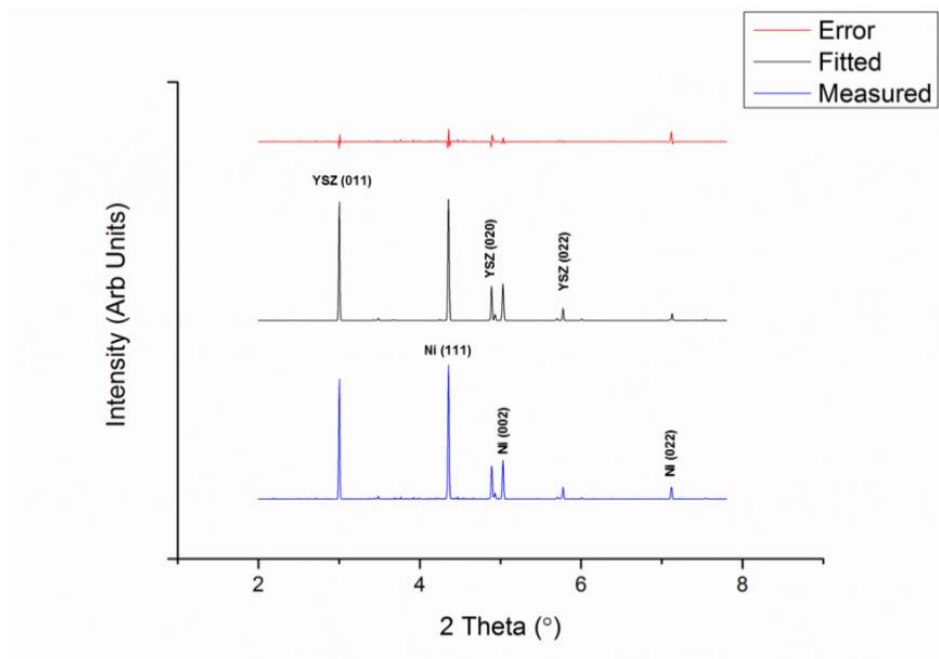
Figure 44 - Measured and fitted XRD diffraction patterns for a sample at 625 °C (located in the centre of the sample) up to a 2 theta angle of approximately 8° with the Ni and YSZ peaks highlighted in the measured and fitted patterns respectively. Also shown is the error trace of the fitting highlighting the fact that all peaks are fitted.

Le Bail fitting was performed using Topas in order to obtain elemental analysis of the X-ray diffraction results with a sample fit shown for a 90° scan obtained from the centre of a sample at 625 °C in Figure 44. The location of YSZ and Ni peaks corresponding to various planes in the crystal structures obtained from the XRD patterns are highlighted in Figure 44 in addition to an error trace which indicates the fitted result obtained correlates well with expected results. In addition, the amplitude of the peaks is within a 5% error in each case. Similar results were observed across the full length of the sample and at all temperatures observed for both the

90° and 180° cases. Trace quantities of NiO were observed during the fitting; however, the absolute quantity of NiO never exceeded 3% (occurring at approximately 400 °C) and remained constant throughout the 30 minute scan in all cases, indicating no oxidation of the sample occurred during the scans.   While the calculated quantities of NiO remained constant during heating cycle, it was observed that the NiO peaks increased in integrated area; this is due to slight alteration in the location of measurement between scans. Such peaks are visible in Figure 45 which shows the effect of temperature on the scans obtained for a sample from ambient to 600 °C.

Figure 45 highlights the 90° Ni peaks obtained during Topas analysis over the range of temperatures examined during the experiment. It is evident that the location of the peaks shifts negatively with increased temperature, with the Ni (022) peak shifting from a 2-theta angle of 7.22° to an angle of 7.17°.   Additionally, it is evident that the amplitudes of the Ni peaks remains relatively stable, indicating a stable sample composition throughout the duration of the experiment enabling direct comparison of the results obtained between temperatures.   A small increase of NiO peaks is observed at a 2-theta angle of approximately 6.1° from 350 °C to 400 °C, with a subsequent reduction in the peaks from 400 °C to 600 °C.   The results seen in Figure 45 also show the NiO concentration remained

stable throughout the experiment with the NiO peaks, evident between a 2θ angle of 5.5° and 6° remain constant throughout each individual experiment.
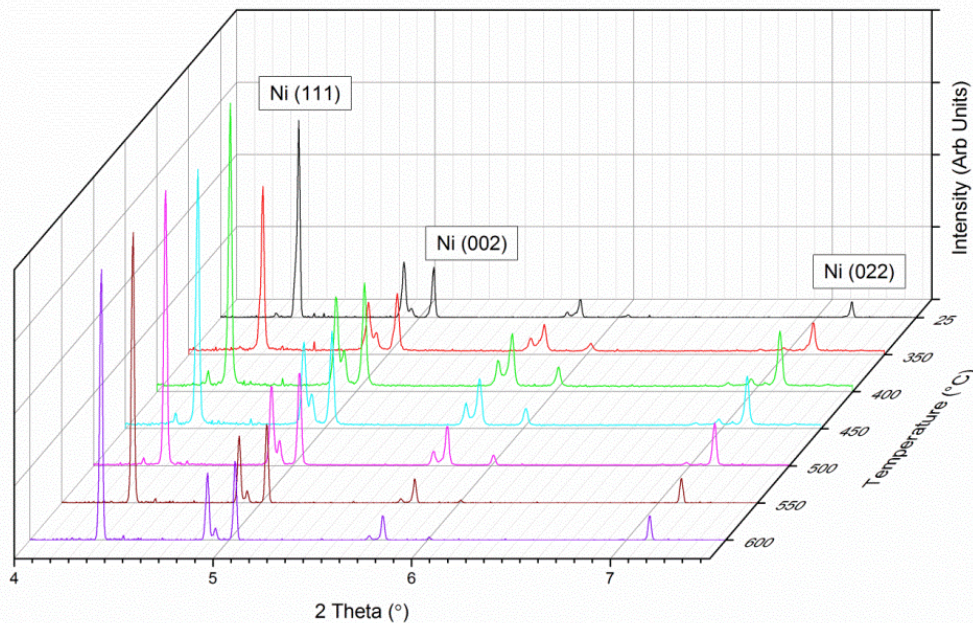
Figure 45 - X-ray diffraction patterns showing the change in location of Ni (highlighted) and YSZ peaks with increasing temperature from ambient (25 °C) to 600 °C. All XRD patterns shown are taken from the same scan location over the range of temperatures.

As the Ni unit cell is face centred cubic, a pure Ni unit cell can be described by a single lattice parameter [190]; this, however, is not the case when the Ni is incorporated into a Ni/YSZ cermet due to the constraining effect of the YSZ electrolyte, as seen in Figure 46, which shows an offset between the 90° and 180° Ni lattice parameters. Due to the interconnected, complex 3-D structure of the Ni phase within the cermet mixture, the Ni grains will be randomly orientated throughout the mixture. Given this random orientation, defining a

universal Poisson's ratio is not possible. Instead, averaged Ni lattice parameter lengths in the 90° and 180° directions are described based on an assumption that the crystals are orientated with equal probability in all directions along the beam path through the thickness of the sample. These averaged parameters are obtained by calculating the eccentricity of the Ni diffraction signal obtained in the first and second quadrants throughout the full 10 mm thickness of the sample.

The effect of incorporating Ni into the cermet mixture is highlighted in Figure 46 which shows a constant offset between the averaged Ni 90° and 180° lattice parameters over a wide range of operationally relevant temperatures using data obtained at beamline I-12.

The elastic deformation in both the Ni 90° and 180° lattice parameters, evident in Figure 46, is as a result of linear thermal expansion caused by a uniform heating / cooling cycle. This behaviour, which is a well-established phenomenon, can be described by a single (temperature dependent) parameter, namely the CTE, given by the slope of the curve. The offset observed between the 90° and 180° Ni lattice parameters is seen to be constant across the full range of temperatures and is observed due to the creep caused by the reduction of NiO to Ni in the formation step of the anode. In both the heating and cooling cycles shown in

Figure 46 the contribution to the change of Ni lattice parameter is a simple product of the temperature change and the coefficient of thermal expansion.
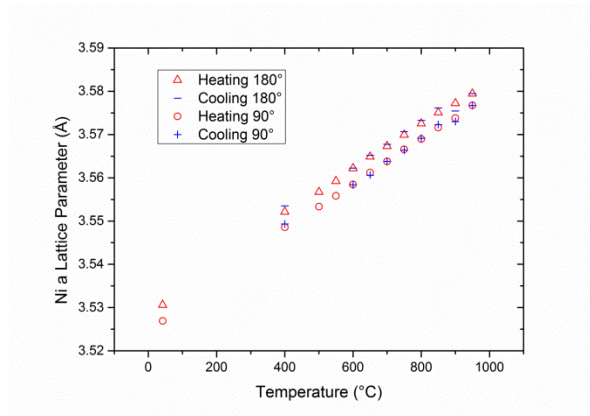
Figure 46 - Offset between Ni 90° and 180° lattice parameters due to the reduction of a NiO/YSZ layer to Ni/YSZ over a range of operationally relevant temperatures.
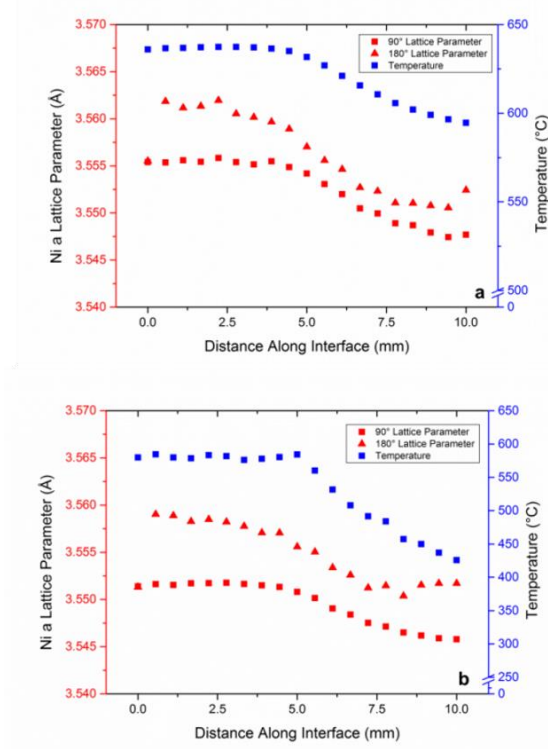
Figure 47 - Ni 90° and 180° lattice parameters (red) and the temperature variation identified using infrared imaging (blue) measured across the length of the sample at two nominal temperatures a) 640 °C b) 590 °C.

Figure 47 shows the effects of temperature variations on the Ni 90° and 180° lattice parameters. The results are presented to show both the temperature variation identified by thermal imaging and the lattice parameters obtained from XRD analysis. The results displayed in Figure 47 show a non-uniform contraction in the averaged 180° Ni lattice parameter with respect to the averaged 90° Ni lattice parameter. While the behaviour of the averaged 90° Ni lattice parameter is consistent with linear thermal contraction (there was no observed deviation from the expected close to plane stress condition as no temperature variation exists in the 90° direction), the averaged Ni 180° lattice parameters show considerable deviation from the behaviour expected. Rather than a uniform offset between the two lattice parameters, as shown in , a convergence is evident along the length of the sample, coinciding with the onset of the temperature variation. In addition, contraction of the averaged 180° lattice parameter is evident prior to the onset of the temperature variation, indicating that the presence of a temperature variation affects the lattice parameters, even in regions of constant temperature.

This behaviour can be explained by a proposed 'nearest neighbour effect' (shown diagrammatically in Figure 48), with the resultant contraction of the averaged 180° lattice parameters along the isothermal region (0 – 5 mm) being caused by the reduction in the Ni lattice parameter along the gradient. Given that the Ni must be interconnected throughout the anode to ensure sufficient electronic

conductivity, a large contraction in the Ni unit cell in a single direction will increase the stress on its neighbouring unit cells resulting in exacerbated deformation, as indicated in Figure 48.
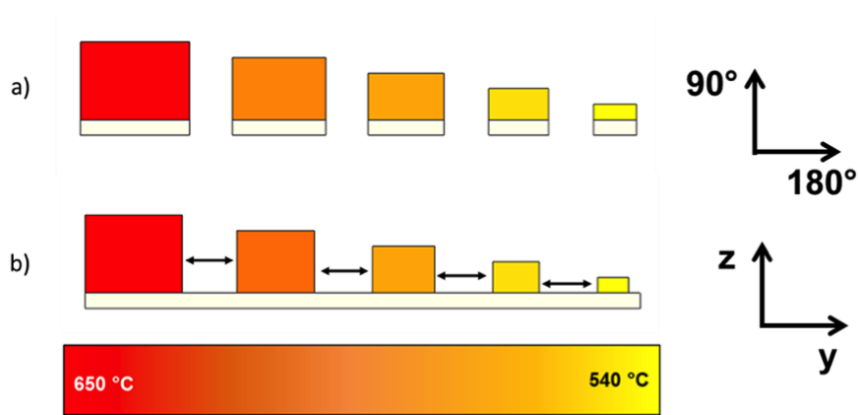
Figure 48 - Diagrammatic representation (not to scale) of the nearest neighbour effect. The effect of constraining a Ni / YSZ cermet (shown with a red to yellow colour scale) on a YSZ electrolyte (shown in white) for both (a) a number of discrete temperatures and (b) along a temperature variation are described.

Figure 48(a) shows the effect of discrete temperatures on the Ni / YSZ cermet which is constrained by a YSZ electrolyte layer due to the mismatch in CTE between the two component layers. Here, an offset between the 90° and 180° averaged lattice parameters is shown to be caused during the reduction process by the constraining electrolyte layer. However, due the uniform and discrete temperatures, no interaction between thermally mismatched grains occurs and contraction occurs at equal rates for both lattice parameters. This contrasts with the effects observed in presence of a thermal gradient, as described by Figure 48(b).

Due to the temperature variation, strains are manifested across interconnected grains at different temperatures and thus non-uniform levels of expansion occur. The effect of these interactions is to exacerbate contraction in the plane perpendicular to the constraining electrolyte layer (corresponding to the averaged 180° lattice parameter) and thus induce larger stresses upon the individual grains. In this instance the extent of deviation from a case of constant temperature will depend on the magnitude of the temperature variation across the sample in all directions. As a result of the nature of this experiment a one-dimensional temperature variation was imposed resulting in deviations only in the averaged 180° lattice parameter (which is parallel to both the temperature variation and the electrolyte layer). This effect will be influenced by the microstructure of the anode, with a high level of solid phase connectivity increasing the interaction between the grains.

The results of were used as a control sample set in order to directly compare similar cells, both with and without a temperature variation. In order to compare the two cases, models were developed using a linear fit in MATLAB to relate the average lattice parameter length in both the 90° and 180° directions to the absolute temperature. Utilising this model and the temperature variations observed in Figure 47(a), an 'expected contraction' curve was generated. This curve enables a direct comparison between the extent of contraction

in the averaged 180° Ni lattice parameter in the presence of a temperature variation (Figure 47(a)) with an expected contraction (obtained from a similar sample (Figure 46)) investigated without the presence of a temperature variation. Both the measured and modelled deviation from a normalised Ni 180° lattice parameter taken at 640 °C are displayed in Figure 49.

By comparing the expected and measured results it is evident that the presence of a temperature variation causes a significantly amplified deviation in averaged 180° lattice parameter than would be expected from linear thermal expansion type behaviour (which is modelled in Figure 49). Once more, it is proposed that the 'nearest neighbour effect' results in significantly increased distortion in the Ni unit cell. The distortion shown above can be considered to be an indication of the stress experienced by the mean Ni unit cell in the 180° direction; while in the 90° direction linear thermal expansion behaviour is the only cause of thermal stress.

Thermal stress was calculated for points along the temperature variation from the first principal definition of strain ($\varepsilon_{thermal}$, which is given by Equation 33.

$$\varepsilon_{thermal} = \frac{L - L_0}{L_0}$$

(33) Calculation of Thermal Strain

Where L is the Ni lattice parameter length at a given temperature and L_0 is the stress-free Ni lattice parameter length obtained at a sintering temperature of 1100 °C. The thermal stress ($\sigma_{thermal}$) then obtained at the discrete points along the temperature variation by utilising the definition of Young's modulus (E) for elastic materials to yield.

$$\sigma_{thermal} = E \times \varepsilon_{thermal}$$

(34) Calculation of Thermal Stress

This calculation was performed using values of the Young's modulus obtained from Pihlatie *et al.* [191] at the relevant temperatures of interest. Figure 50 shows the results of the calculated thermal stress as a function of temperature for the samples across three independent experiments.
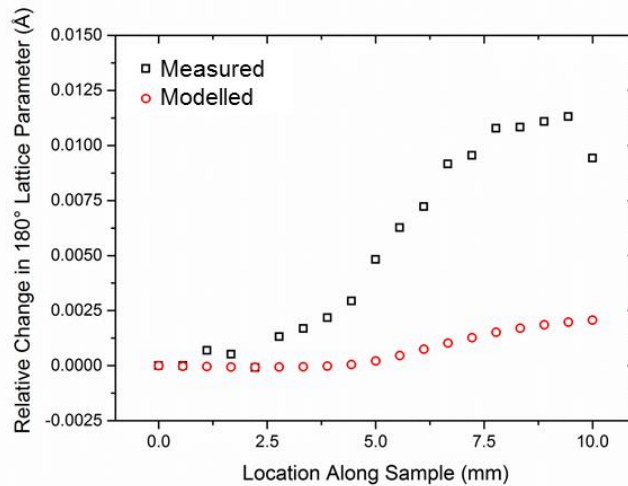
Figure 49 - Relative change of both the measured and modelled value of the Ni 180° lattice parameter along the length of the sample using the data displayed in (a) at a nominal temperature of 640 °C.

Once more it is observed that non-thermal expansion type stress behaviour is displayed by the Ni 180° lattice parameter in Figure 50. The linear behaviour displayed by the 90° lattice parameters, which result in a uniform grouping of lattice parameters obtained at constant temperatures, is consistent with behaviour expected along the isotherms in which the measurement was taken. In contrast, a stress gradient is observed along isotherms in the 180° lattice parameters. The magnitude of the isothermal stress is seen to range between 50–75 MPa in all cases which, when compared to the lowest absolute thermal stress along the isotherm, results in a stress gradient between 10–16 % of the absolute tensile stress. This increased stress, along what is ostensibly a region where no thermally induced stress gradient is present, is significantly large under the externally unconstrained sample conditions in which the experiments were performed; however, by adding constraints to the edges of the sample, the stress within the sample will increase even further, thus increasing the chance of fracture of the sample.
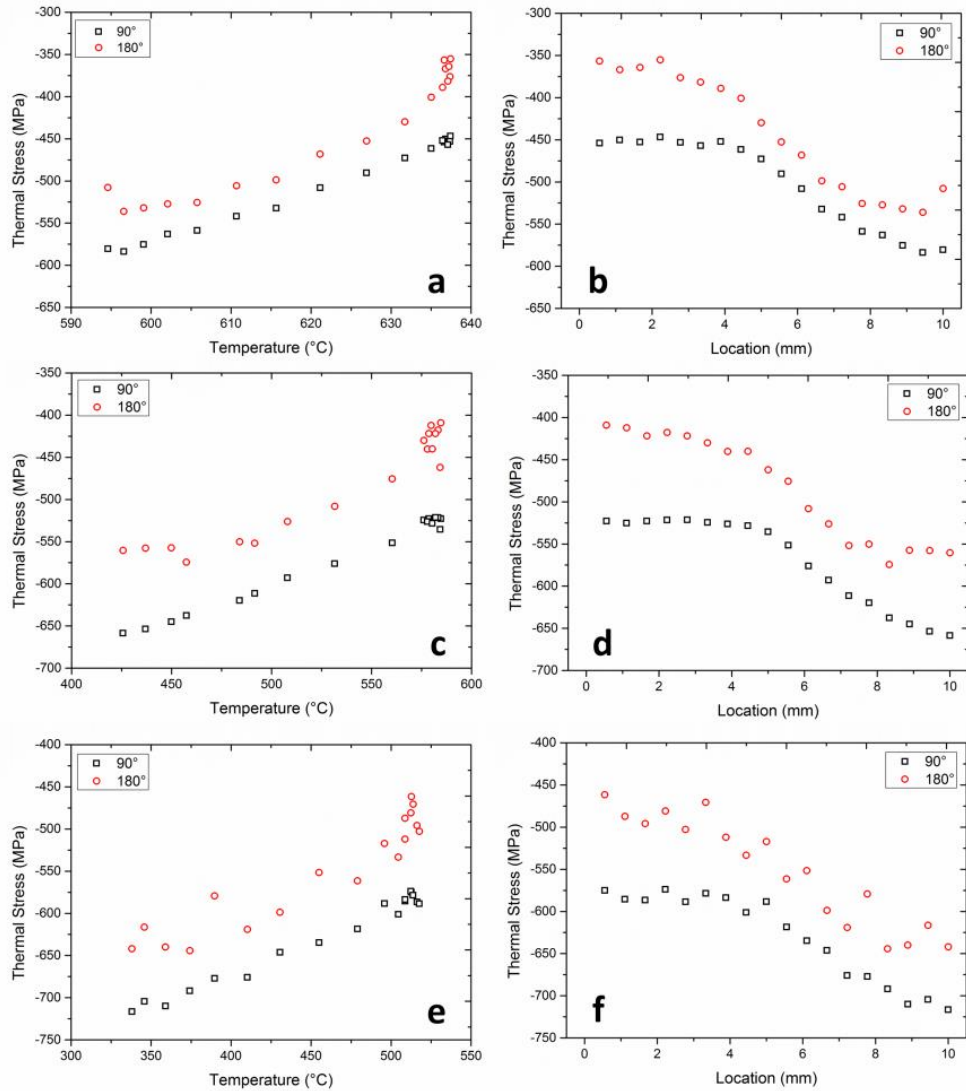
Figure 50 - The effect of temperature variations upon the tensile stress within the sample with respect to the Ni lattice parameter lengths at a stress free temperature of 1100 °C for both the 90° and 180° Ni lattice parameters at nominal temperatures of: (a) 640 °C; (c) 590 °C; (e) 525 °C. Also shown is the location along the sample at which the stress is calculated at nominal temperatures of: (b) 640 °C; (d) 590 °C; (f) 525 °C.

5.4   Finite Element Analysis of Steady State Operational Stresses Due to Thermal Heterogeneity

In order to gain an insight into the effect of the results detailed in Section 5.3 finite element analysis (FEA) was performed on a simple SOFC system.   The model, which was run under steady state conditions, showed that temperature gradients were inherent due to flow configurations and fuel utilisation.   These temperature gradients were then transformed into stress distributions using simple relationships detailed below to generate stress maps which account for the results previously obtained.   The model further highlights the need to include these non-uniform stress fields even in the simplest of scenarios – an unconstrained single cell operating with no internal reforming using hydrogen and air as reactants.

Finite element analysis was performed using a modified SOFC model available with COMSOL Multiphysics (Version 5.0, COMSOL Ltd., Cambridge, UK).   The model utilised a number of well-established mass and momentum transfer laws in order to enable the investigation of the current density distribution in a full SOFC.   In preparing the model a sample geometry (shown in Figure 51(a)) was built within COMSOL to reflect a similar sample to that described in Section 5.3; however, due to computational restrictions the maximum width of the sample which was examined was 5 mm. The model was composed of two flow channels spaced 4 mm apart on both the

anode and cathode which enabled gas to be supplied. The flow channels were 0.5 mm in width and both traversed the full 10 mm length of the cell. In order to achieve an accurate representation of the samples analysed during the experimental work, modifications were made to the default COMSOL properties (as seen in Table 5).

A user defined mesh was designed in order to reduce the computational time required to solve the equations, as seen in Figure 51(b). The mesh was designed to maximise the nodal density at the surface of the electrodes and at the interface between the electrodes and electrolyte. In doing this, high resolution results were obtained in these regions allowing accurate reporting of current density gradients in these areas. In contrast, a relatively wide mesh was employed through the flow channels; the errors introduced by this mesh were examined by increasing the nodal density which resulted in negligible difference to the gas concentrations along the gas flow channels.

To solve the equations both electronic and ionic charge balances were performed at all nodes using Ohm's law, with Butler-Volmer charge transfer kinetics also solved at each node. Momentum balances were solved using modified Navier-Stokes equations in the gas channels, with the Brinkman equations solved in the porous layers within the electrodes [192].
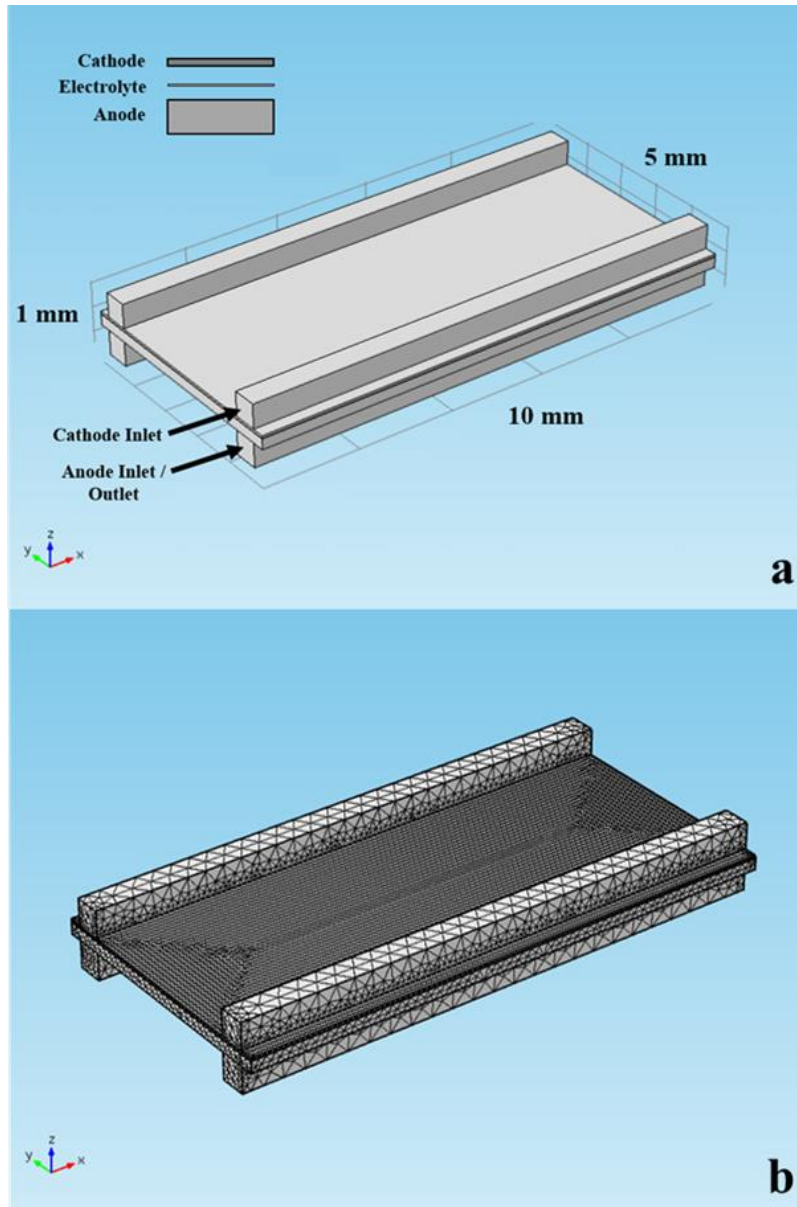
Figure 51 - (a) Geometry of the investigated SOFC used during computational modelling showing a scale schematic of the cell construction and the cathode inlet used during all simulations. Also shown is the anode inlet (used during co-flow simulations) and outlet (used during counter-flow simulations) and (b) the user defined meshing strategy used in all simulations.

Mass balances were performed at all nodes using Maxwell-Stefan's diffusion and convection equations. In order to solve all equations boundary conditions were supplied at the inlet and outlet of both gas

flow channels with the inlet pressure and composition defined in addition to the operating temperature and voltage.

To investigate the microstructure of the sample, focused ion beam tomography was performed. A Zeiss XB1540 FIB-SEM was used to collect the images, with imaging being performed at 5 kV in SE2 mode to achieve a suitable contrast between the pore and solid phases. Milling was performed using a 50 nA Ga^+ ion beam with an accelerating voltage of 30 kV. Prior to imaging, the sample was cast in an epoxy resin to enable accurate imaging; the sample was subsequently sputter coated with gold. A total of 76 images were used for reconstruction, which was performed using Avizo Fire (FEI, Oregon, USA) with a sample SEM image shown in Figure 52.
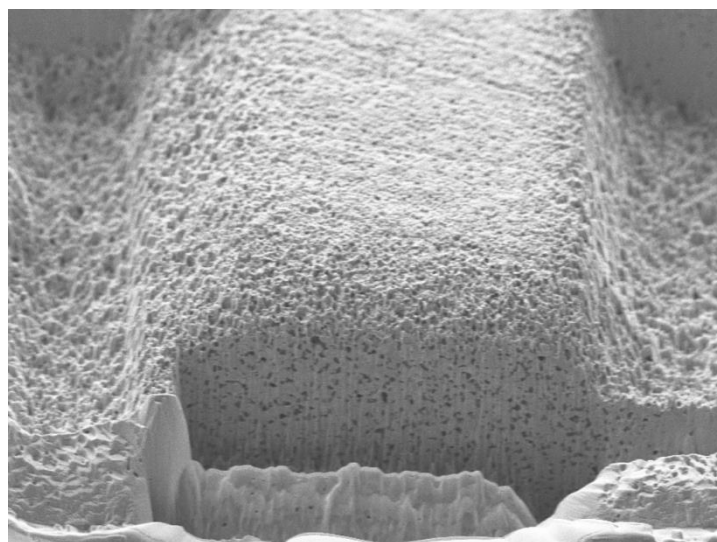
Figure 52 - Scanning electron microscope image used during FIB tomography reconstruction of the anode / electrolyte microstructure. Pores in the Ni-YSZ anode are visible in the image with the milled trenches also shown.

In total a reconstruction volume of 3,250 µm^3 was generated. Image analysis was performed in MATLAB (R2014a, Mathworks, Massachusetts, USA) and indicated a porosity of 18.7 % through the reconstructed element.

Table 5 Selected modifications to the COMSOL default parameters for Ni-YSZ anode.

Parameter	Value	Reference
Thickness	250 µm	Measured
Density (ρ)	3310 kg m^{-3}	[193]
Specific Heat (C$_p$)	450 J kg^{-1} K^{-1}	[193]
Electronic Resistance (R)	250 mΩ cm^2	[171]
Porosity	18.7 %	Measured
Young's Modulus (E)	53.1 – 56.4 GPa	[171]

Modelling was performed for both co-flow and counter-flow conditions using gas flow conditions which limited fuel utilisation to less than 5%. Multiple polarisations were investigated from 0.05 V to 0.8 V, which produced current density distributions for the full geometry in all cases.

The microstructure of the sample will have a large bearing on the nearest neighbour effect, with low pore phase connectivity increasing the effects observed. In order to quantify the microstructure of the samples used in the experiments, FIB tomography was performed. Both the solid and pore phases were reconstructed and are shown in Figure 53. The solid phase shown in (a) is seen to be fully connected throughout the sample, in contrast to the pore phase as

seen in Figure 53(b) which shows poor phase connectivity. The highly connected solid phase provides a thermally conductive pathway through which the temperature variations can be relayed, facilitating the nearest neighbour effect. This microstructurally dependent nearest neighbour effect can be used in conjunction with previous results indicating that the porosity of the sample impacts upon the stress within the anode [194, 195]; with a high porosity increasing the possibility of a high pore connectivity.
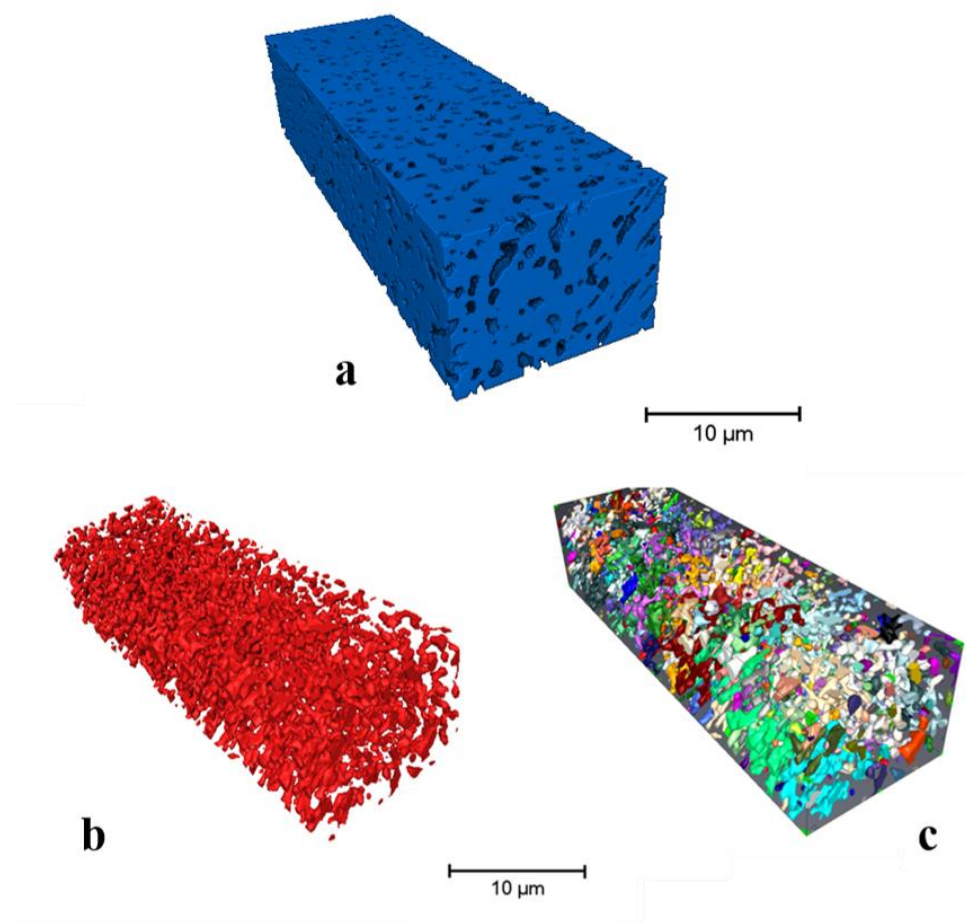
Figure 53 - Microstructural reconstruction of a representative volume of the sample showing: a) solid phase, b) pore phase and c) connectivity of the pore phase with connected pores shown in the same colour obtained using FIB tomography.

The computational simulations were used to generate current density distributions within a sample SOFC geometry, as shown in Figure 51(a); which, were in turn used to evaluate operational temperature variations relevant for operation with hydrogen as a fuel. The calculated temperature variations generated were subsequently used as a basis to evaluate the thermal stress distributions. The FEA was conducted for both co- and counter-flow conditions over a range of polarisations from open circuit voltage to 0.3 V. Electrochemical results indicate that the performance of the SOFC under counter-flow conditions was significantly better (300% increased current density at 0.6 V). The current density distributions obtained using FEA were used to calculate local heat generation by investigating the effect of Joule heating both in the anode and at the current collector. Joule heating (Q) which is given by a simple relationship between the electronic resistance (R) and local current density (i) shown in Equation 35:

$$Q = i^2 R$$

(35) Joule heating effect due to the presence of operating electric currents within the modelled SOFC geometry

This heat flux can then be converted to a temperature change (ΔT) by utilising the nodal structure employed within the COMSOL model which enabled a representative volume (dV) to be established for each point calculated in addition to knowing the density (ρ) and specific heat capacity (C_p) of the materials in question.

$$\Delta T = Q \cdot C_p \cdot \rho dV$$

(36) Temperature change as a result of the operating electric current distribution within the SOFC geometry

The polarisation curves generated indicate that the performance of the cell under counter-flow geometry was significantly better. Thermal stress was calculated using the coefficient of thermal expansion (α) and is described in Equation 37.

$$\sigma_{thermal} = E \cdot \alpha \cdot \Delta T$$

(37) Calculation of the thermal stress due to temperature variations between nodes in the model

By exploring the current density distribution at a number of polarisations it is possible to examine the effect of temperature variations present on thermal stress in SOFC anodes due to localised electrochemical reactions, the results of which are shown in Figure 54.

The thermal stress distribution in Figure 54 show that temperature variation occur at the anode inlet for both the co- and counter-flow situations. In order to ensure all the maximum thermal stress is described in all instances, a minimum thermal stress (equivalent to 16% of the maximum) is applied to areas where no temperature variation is observed. This ensures that no underestimation will occur – describing the minimum thermal stress which must be accounted in the design of systems. The thermal stresses experienced at high polarisation under co-flow conditions are seen to

be significantly lower than those observed under counter-flow conditions; however, the current generated by the cell is reduced by 300% under the co-flow conditions. In contrast, at low polarisation, counter-flow operation is seen to exhibit lower thermal stresses in addition to a higher electrochemical activity; therefore, in this scenario it is clearly advantageous to operate under a low polarisation (0.8 V) under counter-flow operation.
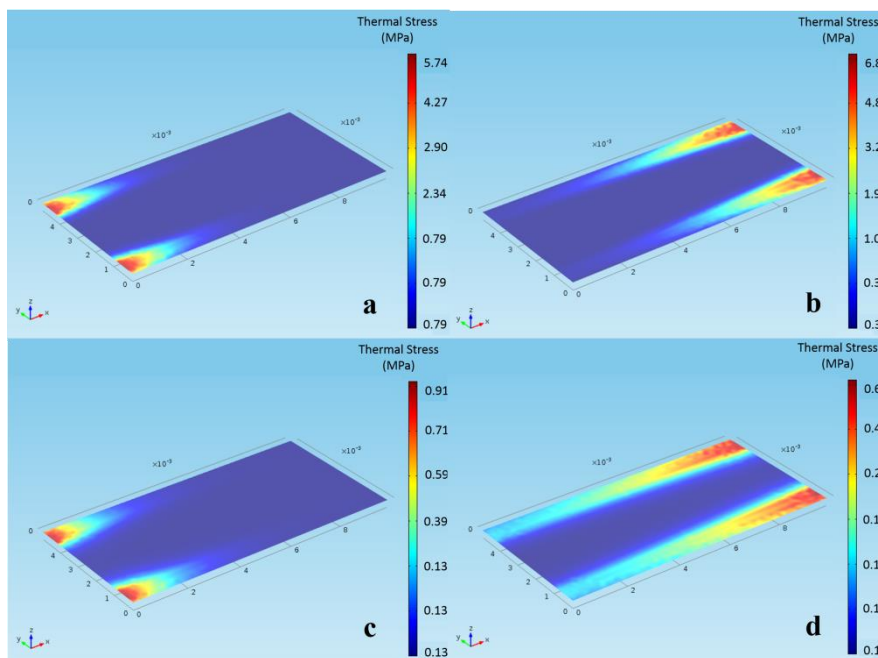
Figure 54 - Two-dimensional distributions showing the magnitude of tensile thermal stress obtained using COMSOL Multiphysics under co-flow (a, c) and counter-flow (b, d) conditions at a polarisation of 0.7 V (a, b) and 0.3 V (c, d).

While the thermal stresses associated with operation in this instance are relatively small, should internal reforming take place under similar electrochemical loading conditions the total thermal stresses will be significantly larger (as seen under the experimental conditions). In addition, thermal gradients generated through the internal reforming

process may be localised within the cell. In this instance it is important to consider both contributions from the internal reforming and operation as the contribution of each respective process may occur at different locations in the cell or stack. Additionally, in both the experimental and computational investigations reported herein, the samples have not been externally constrained. The effect of such a constraint will be to exacerbate the thermal stresses, potentially leading to conditions which may result in cell fracture and failure.

5.5 Conclusions

Non-uniform thermal expansion has been observed in Ni / YSZ SOFC anode half cells due to the presence of operationally relevant temperature variations using synchrotron radiation. Analysis of the X-ray diffraction peaks shows a good fit for both the 90° and 180° Ni lattice parameters for a simple face centred cubic unit cell, enabling analysis using commercial software which results in high accuracy correlation with the temperature variations obtained. The temperature variations, which were measured using infrared thermal imaging, have been shown to cause significant deviation from the behaviour expected if only thermal expansion type behaviour was considered.

Convergence between the Ni 90° and 180° Ni lattice parameters is observed across the length of the sample coinciding with the temperature variation. The convergence is observed prior to the onset of the temperature variation suggesting a 'nearest neighbour' effect which results from the connected nature of the Ni within the anode microstructure and results in deformation along isotherms due to the neighbouring unit cells contracting as a result of the temperature variation.

Comparison with work performed on similar samples at uniform temperatures has demonstrated that deviations of up to 400 % from the expected thermal expansion behaviour have been observed at operational temperatures indicating the presence of significantly higher strain in the Ni phase than would be expected.

Tensile thermal stress has been observed throughout the sample. It is observed that this compressive stress reduces with increasing temperature and behaves in a linear fashion for the 90° lattice parameters due to the experimental set-up. Thermal stress gradients of 10–15 % of the absolute stress have been identified along isotherms for the Ni 180° lattice parameters caused by the presence of temperature variations. Once more, such behaviour is explained by the 'nearest neighbour' theory. Additionally, constraining cells will

increase this stress resulting in an increased likelihood of fracture of the cell.

Finite element analysis has been conducted to investigate the operational effect of the non-uniform stress gradients observed in the SOFC anode. Through modelling the temperature distribution due to a range of steady state operating conditions was obtained. These stress gradients, which arise due to the presence of temperature variations inherent under normal operating conditions due to flow and reactant concentration heterogeneities, must be considered when describing thermal stresses within SOFC anodes. Models must also consider additional stresses when describing the stresses experienced within SOFC anodes during start-up and shut-down, heavy cycling or under internal reforming conditions which can cause large temperature variations and therefore exacerbate the results obtained through the computational modelling reported here, resulting in significant underestimation of the compressive stresses present.

6 Lock-In Thermography of Li-Ion Pouch Cells

6.1 Lock-In Thermography Methodology and Technique Review

Lock-in thermography is an advanced thermal imaging technique used to monitor the propagation of thermal waves within a specimen using an infrared detector. The technique typically requires thermal waves to be periodically generated by an external source with the intention of monitoring the distribution of the heat from the source [62]. The heat source can be generated by a wide range of sources including an irradiative thermal shock from a halogen lamp, sound waves or electrical impulses; indeed the source of the heat is unimportant, rather it is the ability of the experimenter to monitor the impulse, and the periodicity of the wave, that is significant. Lock-in thermography is frequently used in non-destructive testing (NDT) for material quality and safety analysis.

Lock-in thermography is described by Busse *et al.* [196] who utilise effects outlined by Rosencwaig and Gersho [197] who showed that both the range at which observations occur and the resolution of these observations depend upon the modulation frequency of the input signal and the thermal diffusivity of the solid of interest [197]. The modulation frequency of the input signal has been shown to be either inversely proportional or proportional to the power of $-^2/_3$

dependent upon the physical properties of the material. In utilising this knowledge, Busse *et al.* provide a technique which combines the maximum available depth analysis and the ability to obtain phase angle information; an ability vital in obtaining impedance information [196].

The thermal diffusion length (μ) is a parameter which determines the depth at which observations can be made, this is a parameter dependent upon the thermal conductivity of material (κ), the volumetric heat capacity (C_v) and the frequency of excitation (f); it is given by:

$$\mu = \sqrt{\frac{\kappa}{\rho C_v \pi f}}$$

(38) Equation for the Thermal Diffusion Length

As a result of the structure of Equation (38 lower frequency modulation will result in deeper observations. Vollmer and Mollmann [51] discuss the mathematical results of lock–in thermography in some detail, a graphical representation is shown in Figure 55.

Figure 55 shows how the response signal (S) is shifted by a phase angle Δφ, this shifted signal is subsequently measured by the infrared detector and stored as an array of temperatures for a given pixel, which is developed using a Cartesian coordinate system.
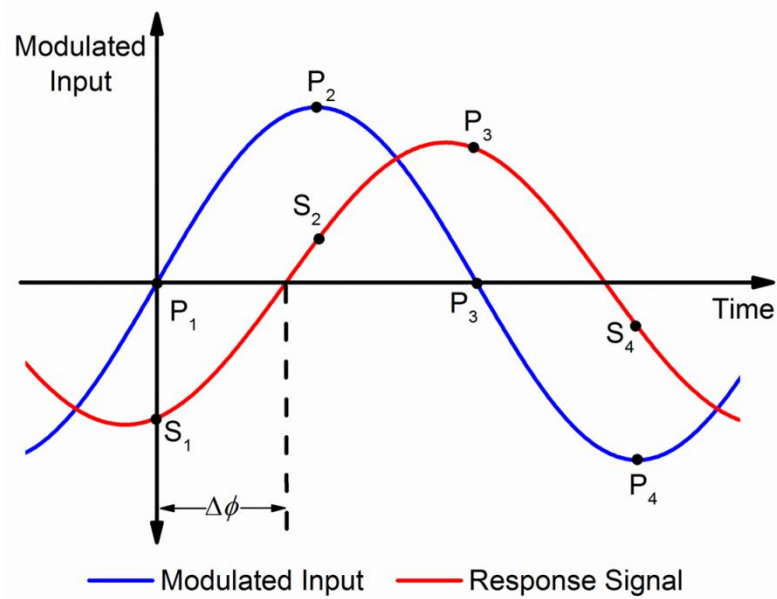
Figure 55 - Measurement principle for lock-in technique, adapted from [51].

This series of (x, y) data can then be used to evaluate both an amplitude (A) and phase signal (ϕ) as shown below,

$$A(x,y) = \sqrt{[S_1(x,y) - S_3(x,y)]^2 + [S_2(x,y) - S_4(x,y)]^2}$$

$$\phi(x,y) = \tan^{-1}\left[\frac{S_1(x,y) - S_3(x,y)}{S_2(x,y) - S_4(x,y)}\right]$$

(39) Four point lock-in measurement equation

This technique, known as the four-point technique, is limited to the situation where the input signal is a harmonically modulated signal [198], however in certain instances this is either undesirable or unachievable. These equations can utilised by software developed for use with an IR camera in order to produce images which accentuate the areas of increased or decreased resistance, whichever the case may be.

152

In situations where non-harmonic pulses are used a digital correlation can be used to equate the pulses to a sine wave and cosine wave. This technique described by Breitenstein and Langenkamp [53] uses a series of weighting factors to gain access to the basic harmonic function only, in order to remove distortion from higher harmonics. This digital method allows one to evaluate the phase of the signal in both an online and offline mode, a factor which is vital in highly transient processes which require high processing power to fully evaluate online. This 'narrow band' method results in two in-phase signals (S) being generated for the 0° and 90° phases. These can then be utilised similarly to the results in Equation 39 to produce the following results for the amplitude (A) and phase (ϕ),

$$A = \sqrt{(S^{0°})^2 + (S^{90°})^2}$$

$$\phi = \tan^{-1}\left[\frac{S^{90°}}{S^{0°}}\right]$$

(40) Digital lock-in measurement equation

A third method of obtaining images using lock-in thermography is to use fast Fourier transforms (FFT). This can only be achieved after all the images have been stored and thus takes a significantly longer period of time to complete; this does however, enable the examination of the object imaged in both the time and frequency domain. This method requires an algorithm to calculate both the real (R) and imaginary (I) component the Fourier transform of the response signal (F) in the form [199]:

153

$$F(u) = R(u) + jI(u)$$

(41) Response signal of a sine wave in Fourier form

This form can then be used to calculate the phase of the signal by:

$$\phi = \tan^{-1}\left[\frac{I(u)}{R(u)}\right]$$

(42) Calculation of the phase of a signal

The advantage to using lock-in thermography is that the average temperature is cancelled out within the software, thus only variations from the mean are evaluated, allowing for increased sensitivity [51]. This sensitivity has been reported to be as low as 10 µK [200].

Lock-in thermography has, in the past, been used primarily for both non-destructive testing (NDT) of aircraft components [51] and electronic devices, for instance semiconductors [198], circuit boards [200] and solar cells [201].

Initial studies using lock-in thermography used contact thermistors, as described by Breitenstein and Langenkamp [198]. Even using the relatively elementary measurement techniques described, the results showed that areas where increased current flows, known as shunts, produced a higher temperature. With the knowledge that these areas can be detected by imparting a modulating current further research was conducted using thermal cameras. Breitenstein *et al.* [200] described the investigation of localized current leaks in

electrical circuits using lock-in techniques. Using the narrow band method the authors demonstrated the viability of lock-in thermography for such a purpose for radiative heat sources as low as 3 μW. In the study the authors showed that the signal-to-noise ratio is proportional to the square root of the frame rate of the camera.

The effect of electrical shunts in solar cells is to lower the voltage of the cell; therefore it is desirable detect and understand how they form to optimise the fabrication process. Breitenstein *et al.* [201] used lock-in thermography to quantitatively evaluate shunt currents. The authors developed a relationship between the amplitude signal measured via lock-in thermography and the current seen in shunting regions. This was undertaken over a planar cell for a range of locations (*x*, *y*). The results investigated the efficiency of cells without shunts, while also considering the actual efficiency of the cells.

The work conducted by Breitenstein *et al.* [201] shows the power of lock-in thermography in developing theory along with practical measurements. This capability is hugely important in order to expand the areas in which lock-in thermography is used and gives great scope to the future work using this technique.

6.2 Introduction

One of the greatest engineering challenges facing battery developers is the ability to ensure effective thermal management [41]. Failure to do so impacts the performance, charge / discharge efficiency, durability and mean time between failures. Inefficient thermal design of battery packs results in reduced gravimetric and volumetric energy density and increased cost. There is a critical need to operate within the safe bounds of temperature operation whilst minimising heterogeneous temperature distribution. The increasing number of models aimed at describing temperature distribution in battery packs is testament to the importance of understanding this critical issue [202].

Incorporation of temperature measuring devices into battery packs is often used for control, test and operational purposes. This ranges from the crude placement of a single thermocouple, to highly complex instrumented arrangements. An alternative to discrete temperature sensors is the use of infrared measurements. This has the advantage of not requiring sensor placement or connecting leads, whilst high spatial resolution and rapid frame collection rates can be achieved. The technique is ideal for measuring the outer surface temperature of a battery pack [107-109, 130]; however, in order to investigate the temperature within a system, the construction needs

to be modified to allow infrared access, which is rarely appropriate for batteries.

Lock-in thermography [53] is an established technique in areas such as structural mechanics [203, 204], electronics [205] and materials science [205, 206]. By examining the relationship between a transient impulse that inspires heat generation within a device and the resulting temperature response, it is possible to interrogate the internal generation and transfer of heat within bodies. Typically, the specimen is exposed to a periodic energy source (e.g. a heat lamp, microwave, ultrasound, eddy current) [207]. Internal defects, such as cracks, high electrical contact resistance points and internal short circuits, act as barriers to heat transfer, resulting in changes to the amplitude and phase delay of the thermal response. For a battery, or other electrochemical power source, a current stimulus will result in internal heat generation as described in Section 1.2. Heterogeneous current density distribution and internal structure differences result in spatially variant thermal effusivity within cells, which impact on surface temperature responses. By varying the stimulus frequency, different frequency-dependant electro-thermal impedances can be interrogated – analogous to electrochemical impedance spectroscopy (EIS).

In addition to generating high-resolution maps of the response to periodic stimuli at different frequencies, the mathematical treatments utilised (based upon Fourier transforms described previously) enable emissivity contrasts to be rejected. Additionally, variations in surface reflections from transient environmental effects can be significantly reduced using multi-frame averaging. This variation rejection technique enables highly accurate measurements to be performed which can identify thermal activity at frequencies which were hitherto inaccessible [208], or required significant periodic averaging to yield accurate results (>0.05 Hz).

Herein, the authors demonstrate, for the first time, the application of electro-thermal lock-in thermography to Li-ion batteries, enabling frequency based temperature measurements which can be used for the detection of internal defects and faults; demonstrating the technique as a potential diagnostic for cells and highlighting the improvement in high frequency measurements which can be obtained using thermocouples.

6.3   Experimental Methods

Li-ion cells with a capacity of 2100 mAh (PL-565068-1.5C, AA Portable Power Corp., CA, USA) were investigated. The surface of the battery was coated with a thin layer of matte black paint in order to ensure uniform emissivity and negate reflections; while this

perturbs the system slightly (due to the addition of an additional thermal impedance) the effect is negligible. The emissivity of the coated battery was calculated using a quasi-black body ($\varepsilon = 0.98$) and a diffuse reflector. Thermal imaging was performed using an infrared camera (640×512 FPA InSb FLIR SC5000MB) which was calibrated in the temperature range 15–100°C. Images were recorded using commercially available software (Altair, FLIR ATS, France) at a frame rate of 100 Hz, in order to ensure a sufficient number of images were obtained to improve the quality of lock-in thermography images. Prior to performing lock-in corrections on the recorded images, the film was analysed to obtain regions within which the global battery temperature did not rise, to ensure no undesired transient effects were observed; images which revealed a temperature rise were not used for the analysis described here.

To establish the sinusoidal current perturbation, a potentiostat (IviumStat, Alvatek, UK) was used. The perturbation was applied with a peak amplitude of 1.8 A (0.85 C approx.) around a net 0 A discharge rate, ensuring a stable open circuit potential (OCP) was maintained. At high frequencies a minimum of 200 cycles were investigated to establish stable electro-thermal temperature oscillations. The current signal was monitored using a current probe (Tektronix A622, RS Components Ltd., UK) and digital acquisition unit (DAQ) (USB 6363 Multifunction DAQ, National Instruments,

USA) which was then amplified and used as an input for the camera to act as the lock-in signal as seen schematically in Figure 56.
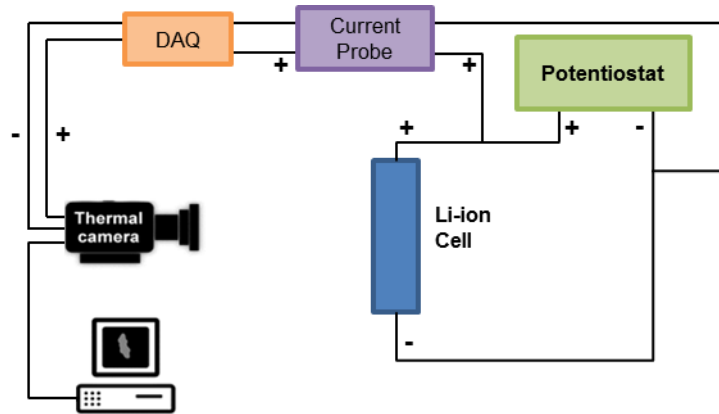
Figure 56 Experimental configuration used throughout all experiments highlighting the connections between the Li-ion cell and potentiostat and the parallel connections passing through the current probe and DAQ board enabling the lock-in signal to be detected

Lock-in thermography was performed using Altair LI software (FLIR ATS, France) using the 'e-mode' setting. A minimum of 1200 sequential frames (at 0.1 Hz) were used in order to achieve sufficient quality for both the amplitude and phase lag images.

6.4   Results

Figure 57 shows both white light (a) and infrared images (b, c) of the cell used throughout the experiments. Emissivity corrections obtained using lock-in thermography are seen when contrasting the average temperature (b) measured in the time domain with the electro-thermoampliogram (c), which is frequency dependent. Whilst

the cell in Figure 57(b) is at a uniform temperature, artefacts associated with surface asperities and paint layer defects that expose the reflective metallic surface, are seen to cause apparent temperature differentials across the surface. These emissivity contrasts are not observed in Figure 57(c).
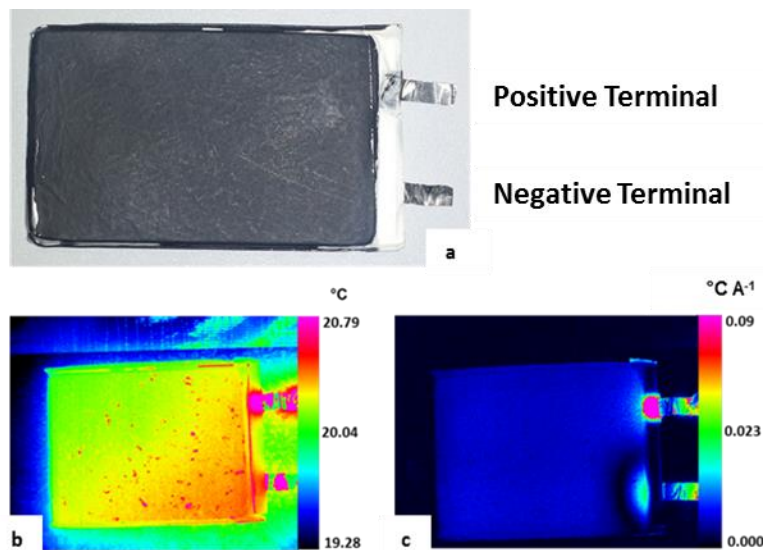
Figure 57 - (a) White light image showing the cell with the terminal location highlighted (note the negative terminal is located on the underside of the cell with the positive terminal located on the top of the cell); (b) average thermogram contrasted with (c) an electro-thermoampliogram performed at 0.1 Hz showing the effect of emissivity contrast rejection.

The phase response of the signal was examined manually to verify the results of the Altair LI software. The time-domain temperature response of a 25 × 25 pixel area to the stimulating electrical signal, is shown in Figure 58.

161
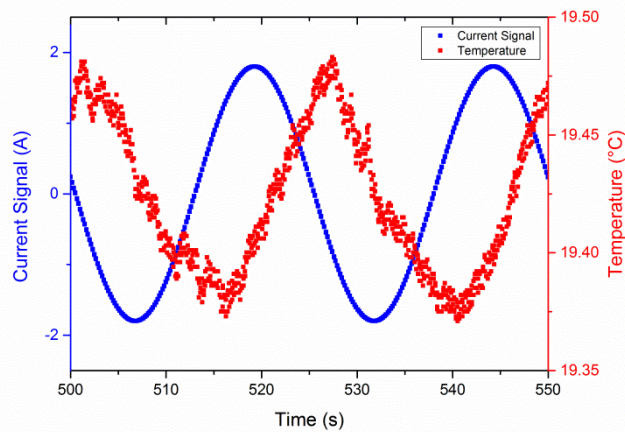
Figure 58 - Time domain electrical stimulus signal and subsequent temperature response taken from a 25 × 25 pixel area at a stimulation frequency of 0.04 Hz.

It is evident that the temperature signal lags due to internal thermal impedances, the form of which will depend upon the cell's thermal properties (i.e. thermal conductivity, heat capacity, thermal diffusivity, etc.), as well as the internal structure. Similar traces to those observed in Figure 58, were obtained for all frequencies investigated, with the phase lag and amplitude ratio being dependent upon the frequency. The effect of frequency can be described by the thermal diffusive length [53]; a characteristic length, which is material dependant and thus variable throughout the internal structure, given by Equation 43:

$$\mu = \sqrt{\frac{\alpha}{\pi f}}$$

(43) Thermal diffusive length of a material

162

Where μ is the thermal diffusive length; α is the thermal diffusivity, and f is the frequency of stimulation.

Figure 59 shows the amplitude response and phase lag of the thermal signal for three frequencies of current stimulation. The amplitude images show an increase in thermal response (°C per Amp) with decreasing frequency [progressing along down the left column from Figure 59(a) to Figure 59(e)], the longer time period allowing heat generated to be transferred and measured as temperature at the surface. The time lag in the heating is observed most clearly at the negative terminal which is located at the underside of the cell, as shown in Figure 57(a). As the frequency decreases from 0.1 Hz [Figure 59(b)] to 0.04 Hz [Figure 59(f)], the phase response at the negative terminal area is seen to shift to be similar to the (top) positive terminal; the longer time period accounting for the longer diffusive length from the back to the top of the battery.

The battery had a complex internal structure with heterogeneous generation of heat and temperature variations established throughout the volume of the structure. However, herein, temperature was a 2-dimensional measurement across the top face. As a result, thermal diffusion in 3-dimensions and interference of the heat generating sources, resulted in broadening and diminished temperature at the

top surface. For example, the heating effect at the positive and negative terminals was expected to be similar, but the temperature response above the negative terminal was diminished. However, performing lock-in at lower frequency resulted in a higher amplitude response and broadening. By decreasing the lock-in frequency the thermal diffusive length was increased, enabling interrogation of heat generation effects further from the surface, as seen in the 0.08 Hz and 0.04 Hz amplitude images.
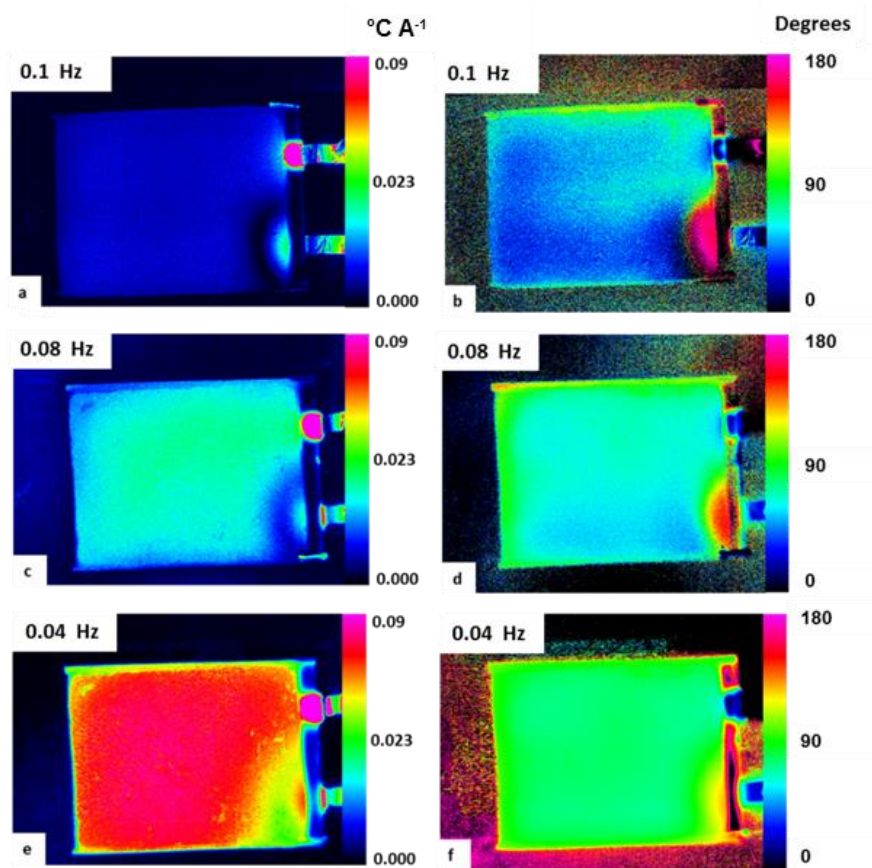
Figure 59 - Amplitude response (a, c, e) and phase lag (b, d, f) of the electro-thermal signal at three frequencies (0.1 Hz, 0.08 Hz, 0.04 Hz).

The effect of cell deterioration was investigated by placing the battery at a temperature of 65 °C for 7 days; this temperature being outside recommended long-term storage conditions for the cell. The cell showed evidence of degradation in electrochemical performance with the Ohmic resistance of the cell increasing from 72 mΩ to 90 mΩ after exposure to elevated temperatures. The increased Ohmic losses were likely due to gas formation which is commonly observed within aged cells [209] and was visible via the appearance of 'bubbling' at the surface fo the cells. This gas formation has the effect of reducing the connectivity between the electrolyte and electrode layers [148], in turn, degrading the performance of the cell. The effect of aging on the lock-in thermography response is shown in Figure 60.
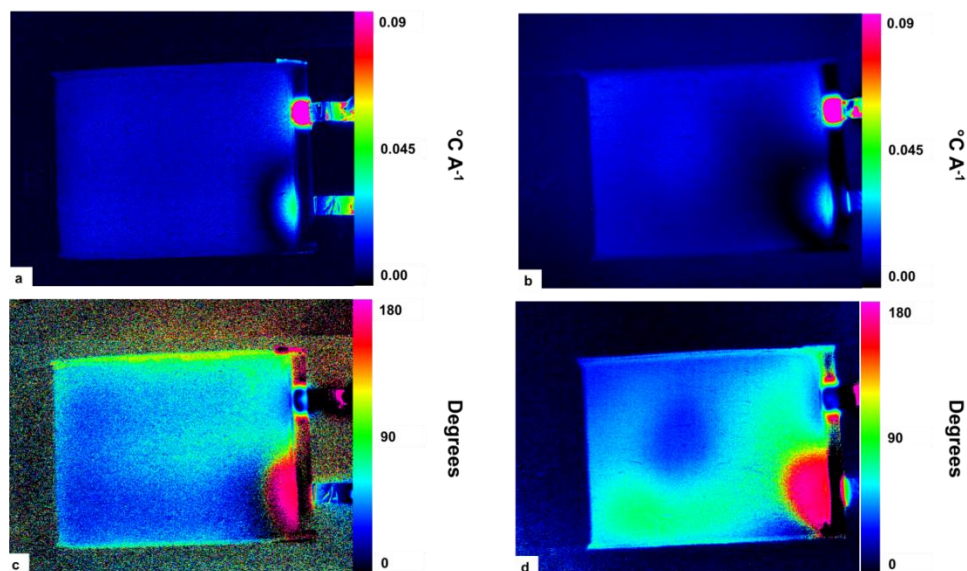
Figure 60 - Amplitude response (a, b) and phase lag (c, d) images of a fresh (a, c) and aged (b, d) cell performed at a single lock-in frequency of 0.1 Hz.

The areas in which gas pockets formed were evident by reduced amplitude response, as seen in Figure 60(b) when compared to Figure 60(a); this was due to the additional thermal impedance added by the presence of a less thermally conducting gas layer. Inspection of the aged battery shows slight bulging of the case in these areas. Utilising this dynamic technique, localised defects in the cell performance could be measured, enabling simple and fast identification of cell degradation, which cannot be observed using conventional steady-state thermography.

6.5 Conclusions

Electro-thermal lock-in thermography has been applied to Li-batteries for the first time to capture heat-transfer processes in the frequency-domain; this allowed the internal heat transfer characteristics of batteries to be studied while operating under pseudo-steady state conditions. This technique offers the potential to identify internal defects in operational systems, providing critical insights for safe and effective battery design and operation. In this instance, gas pockets formed as a consequence of accelerated ageing and were identified using the lock-in amplitude response.

This technique may be applied in the future in a manner which enables the aging characteristics to be monitored in real-time within electric vehicles or process-critical battery packs. Infrared thermal

imaging lends itself to such an electro-thermal analysis much more than the use of other discrete temperature measurement devices. For example, use of thermocouples limits the spatial resolution as thermocouples have their own thermal mass, thus, the response would suffer from artefacts.

This example shows the case for a simple prismatic battery geometry, which is relatively thin in one dimension and can show areas of high heat generation. However, for more complex geometries, by rotating the sample and reconstructing the amplitude and phase response it will be possible to locate the source of heating effects in 3 dimensions. Combined with a knowledge of the internal structure of a battery using X-ray computed tomography [130], a correlative metrology approach would be capable of pinpointing the sources of failure (that result in heat generation) in cells.

7 Electrothermal Impedance Spectroscopy

7.1 Review of the Electrothermal Impedance Technique

Electrothermal impedance spectroscopy (ETIS) is a technique similar to the widely used electrochemical impedance spectroscopy (EIS). Rather than measuring the current/voltage response as performed while conducting EIS, ETIS analyzes the time (t) domain thermal response of a system to current/voltage perturbations. In implementing this technique the current drawn from a battery is modulated periodically with the thermal response being measured. The input (i) and response signals (r) are given by:

$$i(t) = a + b\sin(ct + d)$$

(44) ETIS input signal

$$r(t) = e + f\sin(gt + h)$$

(45) ETIS response signal

After obtaining the input and response curves, a transfer function may be developed by transforming the time domain signals using the Laplace transform shown below:

$$F(s) = L[f(t)] = \int_0^\infty e^{-st}f(t)dt$$

(46) Laplace Transform equation

With the thermal transfer function (Z_{th}) given by Equation 47:

$$Z_{th}(s) = \frac{L[i(t)]}{L[r(t)]} = \frac{I(s)}{R(s)} = \frac{a_0 s^0 + a_1 s^1 + \cdots a_n s^n}{b_0 s^0 + b_1 s^1 + \cdots b_n s^n}$$

(47) General thermal transfer function

Having obtained the transfer function the Laplace variable, *s*, can be replaced by a response parameter for a given frequency, *f*:

$$s = 2\pi j f$$

(48) Laplace variable

Once the Laplace variable has been substituted the final thermal transfer function for a given frequency is obtained in complex form. The amplitude ratio (AR) of the respective signals and phase shift ($\Delta\varphi$) associated with the physical characteristics of the system, namely thermal conductivity and heat capacity, can be calculated as shown:

$$AR = \frac{|a_0 s^0 + a_1 s^1 + \cdots a_n s^n|}{|b_0 s^0 + b_1 s^1 + \cdots b_n s^n|}$$

(49) Amplitude ratio of a general thermal transfer function

$$\Delta\varphi = \arctan\left[\frac{a_0 s^0 + a_1 s^1 + \cdots a_n s^n}{b_0 s^0 + b_1 s^1 + \cdots b_n s^n}\right]$$

(50) Phase shift of a general thermal transfer function

Having calculated the amplitude ratio and phase shift for a single frequency, the experiment can be repeated for a range of frequencies and a Bode plot, a common method of displaying results in control theory, can be produced.

Following the construction of a Bode plot, thermal equivalent circuits can be developed to calculate the thermal conductivity and heat capacity of the system in question. These circuits are similar to those used when conducting EIS; however, in place of the conventional electrical properties, thermal properties are used.

Electrothermal impedance spectroscopy has been described in the literature by a small number of authors. Schmidt et al. [208] reported ETIS using thermocouples to measure the response of the surface temperature of a Li-ion pouch cell to fluctuations in power; however, the use of discrete thermocouples limits spatial resolution and the thermocouples themselves have a thermal response time-constant which must be taken into account. Fleckenstein et al. [210] have similarly used ETIS to investigate $LiFePO_4$ cells using a series of cells and thermocouples resulting in a specific heat capacity being calculated to within 5% of the results obtained using a calorimeter. Despite these studies, the spatially variant nature of the technique has to date not been investigated elsewhere; whilst the frequency ranges investigated has also been inhibited by the use of thermocouples.

7.2   Experimental Methods

Experiments were conducted using a single 18650 Li-NMC cell (ICR18650S3, 2200 mAh, LG Chem Ltd., Seoul, South Korea) which

was fully charged to 4.2 V prior to discharging by constant current charging to 4.2 V and a subsequent constant voltage charge until the current tapered to 3% of the initial applied current using an electrochemical test station (Maccor 4300, Maccor Inc, Oklahoma, USA) at the manufacturer's recommended charge rate of 0.5C. Once more the battery was coated in matt black paint in order to ensure uniform emissivity across the battery and minimise reflections. The battery was subsequently discharged using a sinusoidal discharge wave with an amplitude of 1.1 A (0.5C) generated using a waveform generator (33500B, Agilent Technologies, Santa Clara, USA) controlling a load (PLZ664WA, Kikisui Electronics Corp., Yokohama, Japan) as shown in Figure 61.
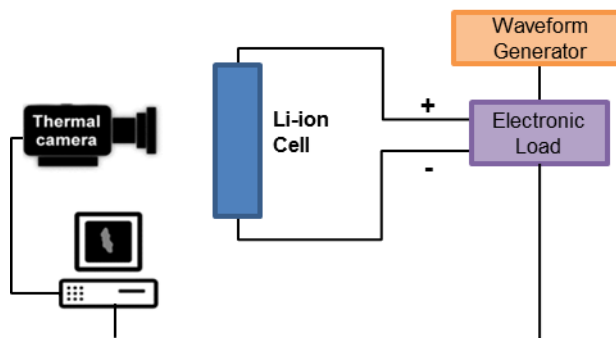
Figure 61 Schematic of the experimental configuration used throughout the experiments indicating the connection between the waverform generator which controlled the sinusoidal discharge current generated using the electronic load

The discharge was offset by a current of 1.1 A in order to ensure a continuous periodic current signal with which to treat the results, this results in a mean discharge rate of 0.5C, ensuring the temperature variation across the cell is minimal. The frequency of oscillation was varied between 100 µHz and 20 mHz resulting with sequences being

recorded using the thermal camera for at least 40 minutes. Current, voltage and power were recorded using a GPIB output from the load unit.

7.3 Results

Due to the 'closed' nature of batteries and when compared to the 'open system' of fuel cells it was observed that small deviations in the voltage occurred during the duration of the experiment. Whilst this is unavoidable working at a discharge current which is not zero, the deviations in voltage were less than 10% of the initial discharge voltage. Prior to analysis, the first 20 minutes of thermal imaging was disregarded in order to ensure a steady state heating cycle was observed, this was further confirmed by investigating the amplitudes of neighbouring sine waves to ensure significant differences were not observed. Further corroboration of a constant heat generation rate was obtained through modelling a dimensionless quantity known as the 'thermal power factor'. This quantity is defined as the ratio between the actual heat generated (Q_{act}) and that which would be generated at a constant discharge current ($Q_{i_{rms}}$) equivalent to the amplitude of the sinusoidal discharge:

$$TPF = \frac{Q_{act}}{Q_{i_{rms}}}$$

(51) Thermal power factor calculation

172

The results of this calculation for a period of 2π are shown in Figure 62 with the extent of offset corresponding to the amplitude of the sinusoidal discharge current (i.e. for a 2 A sinusoidal discharge a 50% offset corresponds to a 1 A offset from a 0 A root mean square (RMS) discharge). Through further modelling it was observed that the behaviour of all frequencies was equivalent when the period investigated corresponded to the frequency.
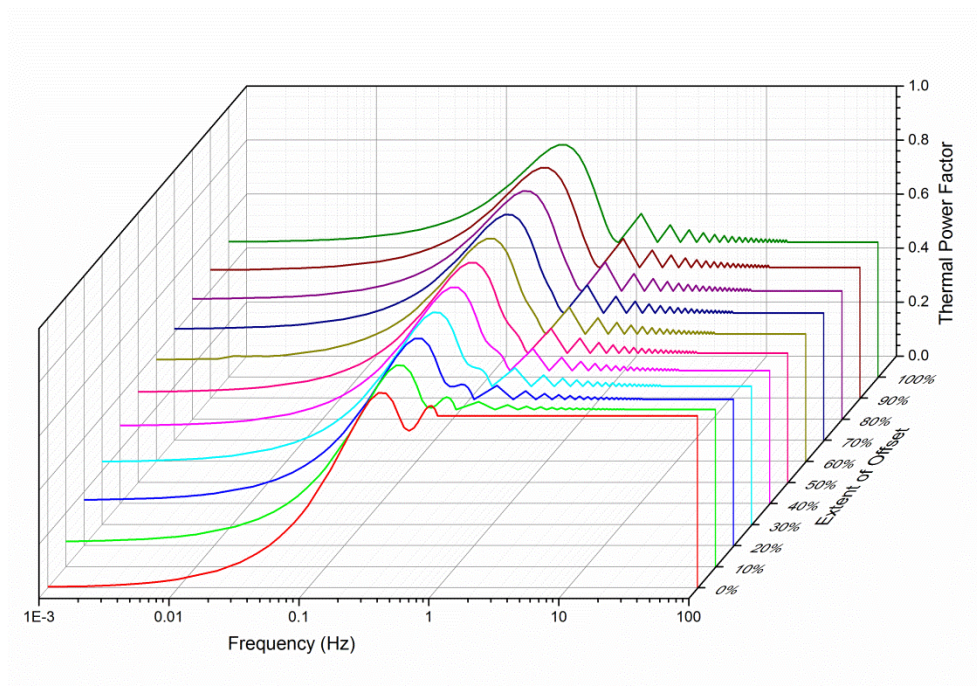
Figure 62 - Effect of offset on the thermal power factor for a period of 2π.

It is clear from Figure 62 than for a 0% offset the thermal power factor varies significantly until the time period corresponding to a single wave is reached at which point the thermal power factor remains constant. However, as an offset from a RMS discharge of 0 A is imposed, the behaviour results in a damped oscillation up to approximately 10 periods at which point a constant thermal power

factor is observed. As such, in order to obtain comparable results, it was imperative to obtain a sufficient number of cycles to account for this behaviour.

Post treatment of the signals was conducted using MATLAB (Mathworks, Natick, Massachusetts), in which both current and thermal response signals were fitted using the curve fitting '*cftool*'. Fitting was performed to ensure the form of the signal and minimise the risk of noise related errors which could skew the results significantly. In all cases the R^2 value; a measure of the 'goodness of fit', was in excess of 0.9.

The effect of location upon the analysis was investigated due to the findings highlighted in Chapter 4. Once more it was found that the longitudinal spatial location of analysis had an impact upon the results obtained. It was noted that the sine waves were 'damped' laterally along the battery. At high frequencies it was observed that the amplitude ratio at both terminals of the battery was higher than that found at the centre of the cell, indicating heat generation from both terminals due to contact resistance; this exceeded the thermal generation due to battery operation observed at the central region of the cell. At lower frequencies (<10 mHz) however, it was observed that the amplitude ratio decreased along the cell from the positive to negative terminal. This is due to the fact that at lower frequencies

the high amplitude region of the discharge current (approximately 1C) has an increased period of time with which to offset the effect of heat loss to ambient, resulting in a larger temperature rise prior to passing into the low amplitude region (approximately C/6) of the discharge wave. The results are shown graphically in Figure 63(b).
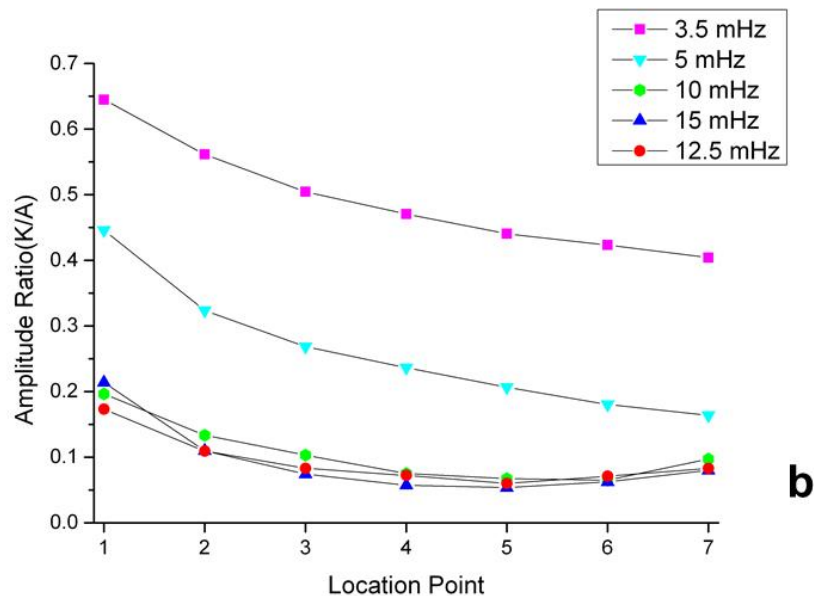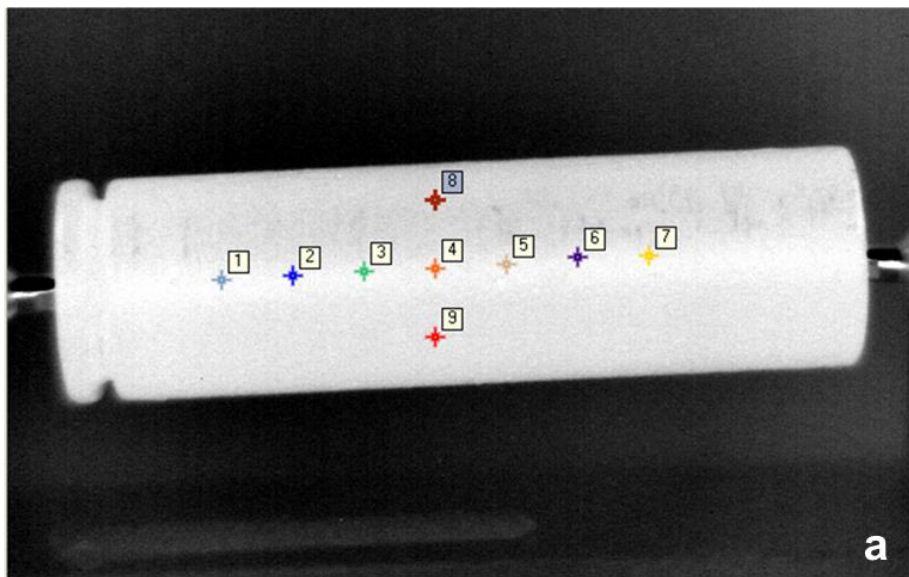
Figure 63 - (a) Location of measurement points used for analysis on Li-ion battery. (b) The effect of the measurement location on the amplitude ratio obtained after analysis.

The effect of the location along the radial surface of the cell is shown in Table 6. Measurements were performed at points 8 and 9 as highlighted in Figure 63(a). It is evident that the radial surface location has a significantly smaller effect upon the magnitude of the result with the results for all frequencies analysed mirroring these results.

Table 6 - Effect of measurement location along the battery casing 'surface hoop circle' with locations as shown in Figure 63(a).

Frequency (mHz)	Amplitude Ratio of Point 8 (K/A)	Amplitude Ratio of Point 9 (K/A)
3.5	0.464	0.464
5	0.242	0.231
10	0.080	0.079
12.5	0.069	0.065
15	0.049	0.055

Having investigated the effect of location upon the results the effect of frequency was considered. The results were obtained by taking an average thermal response over the body of the battery. Due to the experimental set-up it was not possible to ensure the same location was identifiable in all instances, therefore the average response was obtained to maximise the comparability of results. The results are shown as a Bode plot in Figure 64.

The phase shift shown in Figure 64 also shows a general trend to decrease with increasing frequency. At low frequencies the phase is seen to tend towards 0°, whilst as the frequency increases the frequency tends towards 90°. In this instance, analogies can be

176

made towards commonly used electrochemical impedance spectroscopy, in which a pure capacitor results in a phase angle of -90° with a pure resistor resulting in a phase angle of 0°. Drawing this analogy the behaviour at high frequencies is equivalent to that of a thermal capacitor i.e. one which absorbs heat readily, whilst at low frequencies the behaviour of the system is analogous to a thermal resistor.
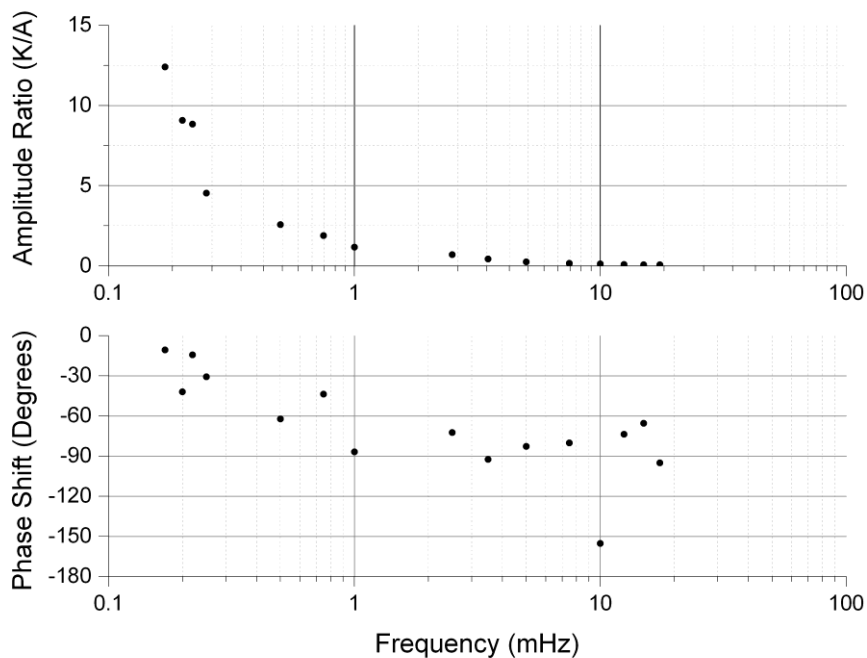
Figure 64 - Bode plot of frequency responses while conducting ETIS on Li-ion cell.

It was not possible to obtain sufficiently low frequencies to observe a stable amplitude ratio or phase shift in this region; however, given the similarities to EIS it is expected that both the amplitude ratio and phase shift would reach a constant level. Were it possible to obtain this region it would be possible to construct a full thermal equivalent circuit model yielding access to parameters such as the system heat

capacity, the thermal resistance and in turn conductivity. This would facilitate swift and accurate experimentally derived parameters which could subsequently be used in computational experiments.

In addition to the electrothermal impedance spectrum obtained in this experiment, the heating effect of low frequency oscillations in Li-ion systems were observed. As low frequencies enable the thermal wave to closely follow the discharge loading, significant heating effects were observed as the frequency decreased, manifesting in high amplitude ratios between the discharge stimulus and thermal response. In essence the effect of low frequency waves is more pronounced as the bulk temperature of the cell is reduced during low magnitude discharges (during the initial and final stages of the sinusoidal discharge), resulting in a reduction in the quantity of thermal energy required to raise the temperature, due to a smaller deviation of the cell from ambient. At high frequencies the bulk temperature is more stable, and higher, resulting in less of an impact at higher temperatures as ambient heat loss must be compensated for to a higher extent. This is illustrated graphically in Figure 65 which shows the fitted thermal response to an identical electrical discharge stimulus at four frequencies.
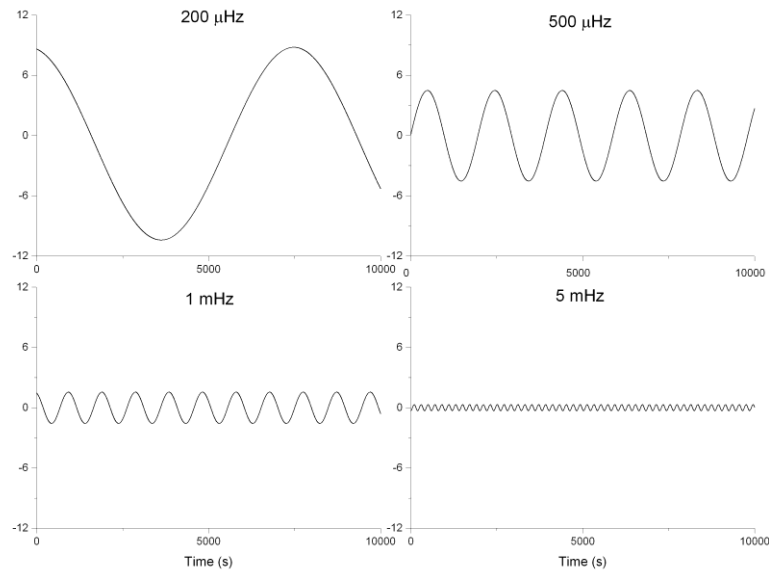
Figure 65 - Amplitude of fitted thermal response signal for the same discharge stimulus at varying frequencies normalized to a mean of 0⁰C for comparison.

It is clear that very low frequency oscillations (<0.5 mHz) of even a small amplitude can cause large thermal effects which may be detrimental not only to the cell, particularly if it is being operated in a high temperature environment or with a high discharge rate for instance. This must be taken into account when Li-ion systems are incorporated into systems where the discharge current may oscillate and as such may require more significant cooling than would be expected were this effect not taken into account.

7.4   Conclusions

The electrothermal response of a Li-ion battery was examined using electrothermal impedance spectroscopy showing an increased

179

amplitude ratio between the heating stimulus, in this case a sinusoidal DC discharge of the cell at lower frequencies. Analogies were drawn between the phase behaviour of the system and that which would be expected of a conventional electrochemical system analysed using electrochemical impedance spectroscopy.

Spatial differences were observed along the length of the cell due to the construction of the battery (which is detailed in Section 4.4.1) with a dampening of the response signal seen from the metallic safety end towards the middle of the cell. The response was then observed to increase slightly along the length of the battery as the effect of the negative terminal was noted. Radial differences along the surface hoop circle of the cell were not observed to be significantly different to those seen in the centre of the battery indicating a one-dimensional deviation in the system parallel to the bulk direction of flow of electrons.

It was also noted that low frequency oscillations manifest themselves in significantly higher amplitude ratios than frequencies in excess of 1 Hz. This effect may result in an increased necessity for system cooling should the cell be exposed to such a discharge profile – particularly in large stacks where cells in the centre may be affected by surrounding devices. By initially examining sample cells using the technique described in this chapter and fully understanding the

variations which inherently occur due to the structure of the cell it is possible to inform the placement of low cost thermocouples on the surface of the cell; in turn, providing a cheap and effective diagnostic tool for Li-ion cells.

8 Conclusions

This thesis has highlighted a number of key studies pertaining to thermal imaging of electrochemical devices. The work has demonstrated the applicability of thermal imaging in examining electrochemical devices – namely high temperature solid oxide fuel cells and Li-ion batteries.

The use of complimentary techniques have also been discussed throughout the thesis. Chapter three examines the effect of external safety mechanisms in this case a positive temperature coefficient type device on the surface temperature distribution of Li-ion cells. Using X-ray microtomography to elucidate the structure of both the safety device and the other external structures at the positive terminal it is seen that at discharge rates in excess of 1C a bias towards higher temperatures occurs towards the positive terminal. Electrochemical impedance spectroscopy conducted over the relevant temperature range confirmed that this bias is not due to the activation of the PTC element and therefore unavoidable under such operating conditions.

Chapter four describes an experiment which utilised sequential thermal imaging and X-ray diffraction to examine the effect of one dimensional temperature distributions within solid oxide fuel cell anodes at operationally relevant temperatures. The distributions which mirrored those seen as a result of hydrocarbon reformation on

the surface of cells were seen to cause significantly non-unifrom contractions in the Ni lattice parameters in the direction of the thermal gradient. These results were obtained using a novel furnace design described in the chapter and further highlighted through the use of finite element analysis.

Chapter five describes the first reported use of lock-in thermography to investigate defects in Li-ion cells. This advanced thermal imaging was shown to be effective in identifying regions of gas formation by contrasting a damaged and fresh cell. The technique was modified to examine its efficacy as an in-situ measurement as described in Chapter six which highlights a similar mathematical method to obtain thermal transfer functions. These transfer functions which are analogous to the transfer functions obtained using electrochemical impedance spectroscopy are also shown to be spatially variant highlighting the importance for a battery monitoring system to be designed with *a priori* knowledge of the behaviour of individual cells and indeed a larger pack.

9 Future Work

This thesis has highlighted a number of key studies pertaining to thermal imaging of electrochemical devices. This area, while nascent, is rapidly expanding as evident by the increasing quantity of articles utilising thermal imaging techniques to gain insights for both operational and modelling purposes. It is clear that thermal imaging can be used in both a 'passive', single frame mode; however, the most significant insights can be gleaned in examining the transient operation of devices.

To date, the use of transient imaging to validate models has been limited; as such, an opportunity presents itself to produce rigorous and fully validated models for both steady and un-steady state conditions. These models would provide the most accurate representation of electrochemical systems to date and simplify the design and operation of systems. In addition, the use of thermal techniques such as lock-in thermography has received very little attention. These advanced thermal imaging techniques enable extremely small variations in temperature to be detected, thus providing opportunities to identify areas of low electrochemical activity, cracks, pinholes and water formation in fuel cell systems; while batteries can be examined for localised current generation and gas formation. Additionally, through the use of advanced thermal

imaging techniques, bulk thermal properties can be identified, which can aid model development.

The use of thermal imaging in a correlative manner has also been examined in this thesis. It is this area which provides the greatest opportunity to understand the systems under examination in a truly holistic manner. By incorporating complimentary techniques such as Raman spectroscopy, FTIR and X-ray microtomography into experiments, active processes can be understood in significantly greater depth and indeed synchronous process can be decoupled. Synchrotron radiation has also been shown to be a useful tool to be used in conjunction with thermal imaging. Recent *in-situ* and *in-operando* experiments have revealed structural deformations in SOFCs and the process of Li-ion battery failure; however, there are significant opportunities to expand on this work. X-ray techniques such as XRD and μCT enable high resolution microstructural information to be obtained, which can be used to generate physical models of systems, while the use of thermal imaging provides the boundary conditions for these models, once more enabling the development of detailed and validated computational models to describe the behaviour of systems at a previously unattainable level of detail.

Expansion of the experiments detailed in Chapter 3 detailing the investigation of stress within SOFC anodes is considered to be a

promising area of future study. As these results are profoundly different to those expected; and as such have the potential to alter modelling strategies, it is suggested that this work could be performed using a similar experimental methodology with alterations to enable improvement and expansion of the results. It is suggested that the temperatures examined could be elevated through additional insulation of the furnace in conjunction with increasing the inlet temperature of the forming gas. This will reduce the heat duty on the cartridge heaters and result in more stable and robust operation.

In addition by enabling a controlled ambient temperature in the furnace it would be possible to modify the magnitude of the gradient in a more facile manner – this will allow the effect of thermal gradients pertaining to localised heterogeneous electrochemical reactions to be examined. The effect of external constraints on the sample is also of interest. In the experiment detailed within the work the sample was an unconstrained 10 × 10 mm half-cell. Whilst this provides a good approximation to the behaviour of a similar full cell due to the close match in coefficient of thermal expansion between the cathode and electrolyte in SOFC systems applying external constraints will more closely mirror the operating conditions of cells. The effect of constraining materials could also be investigated to investigate whether metallic and ceramic interconnecting materials will result in different strain distributions. Ultimately the ideal experiment would consist of an operating SOFC cell which could be

operated under a range of fuels. Whilst this would be a challenging experiment to conduct it is feasible to investigate the effects of heating rates to and from operating temperatures, external constraints and operation of the system under internal reforming conditions. It is also possible that this experiment could be operated under a dual imaging configuration – enabling the thermal gradients at the anode and cathode to be imaged. This would decouple thermal processes at both anode (reforming, electrochemical processes and Ohmic heating) and cathode (electrochemical processes and Ohmic heating), whilst also examining the conduction between the layers. In addition to examining the complex thermal mechanisms within the SOFC cell the lattice strain could be measured in both layers, and indeed in the electrolyte *in situ* enabling the stress distribution throughout the system to be examined in full.

Dynamic thermal imaging techniques may also be applied to SOFCs *in operando*. Lock-in thermography is a technique which may be extremely promising for the identifying and monitoring crack propagation and formation on the surface of and within cells. By exploiting the improved thermal resolution afforded by LIT it will be possible to observe the multiple stages of cell failure using an accelerated stress protocol. This work will be further aided by exploiting the high spatial resolution of thermal imaging systems; by optimising the geometric experimental set-up it will be possible to achieve a spatial resolution of *ca.* 50 µm. This resolution coupled

with a thermal resolution of < 5 mK would be sufficient to identify even the smallest cracks which will affect the macroscale performance of the cell. Sequential electrothermal impedance spectroscopy can be performed using this experimental configuration. By tailoring the stimulation perturbations to a level suitable for ETIS it will be possible to obtain bulk thermal transport properties using a protocol equivalent to the equivalent circuit analysis routinely performed when using electrochemical impedance spectroscopy.

A key requirement for this analysis is to ensure the perturbations are small compared to the steady state value, therefore this analysis is significantly easier in fuel cell systems (where a constant reactant flow is present) than in Li-ion cells. The experiments detailed above can be performed in a number of experimental configurations – initially it is suggested that open cathode experiments are performed; however, with modifications to the cell housing, including an optical window which is water resistant, it will also be possible to access the anode. The extent of exposed electrode will be a key factor in these experiments and should be informed by the in-plane conductivity of the respective electrodes. In order to gain optical access the current collecting mesh will need to be modified; however, should the mesh coverage be insufficient the phenomena observed will not be representative of those present during normal cell operation.

Concerns over the safety of Li-ion systems has recently garnered international attention with high profile failures of the technology resulting in the grounding of the Boeing 787 fleet and numerous high profile failures of automotive batteries . Whilst these events are rare, as cells are pushed towards more demanding operating conditions it is imperative that batteries are investigated with these increasingly challenging performance requirements in mind. In doing so, current cell designs and diagnostic strategies will need to be examined and modified, with novel diagnostic techniques developed to target failure modes. Whilst safety concerns are paramount in the design of cells the incorporation of unmerited safety devices significantly hampers both gravimetric and volumetric power densities of systems; as such, effective, compact thermal management strategies are a key concern when designing systems.

The aging of Li-ion cells is a further aspect which has the potential to severely hinder the wide-scale adoption of electric vehicles (EVs). Whilst the understanding of aging mechanisms is improving research into the effect of these mechanisms on thermal management and performance of technologically relevant cells and packs has typically been limited. In combining a range of experimental methods, observed effects can be decoupled and root cause analysis performed.

It is believed that battery failure is nucleated from microscopic heterogeneities in cells, which then spread throughout the cell. While this effect can cause catastrophic cell failure, it is more likely to degrade performance with time. Failures in a single cell may also propagate across an entire battery pack resulting in failure of the system. To investigate these phenomena in a controlled environment, it is possible to induce a number of relevant defects within cells to enable the effects of these defects to be fully described; informing both the monitoring and safety strategies required within Li-ion systems. In addition to examining the effects of failure, the causes may be investigated by examining cells at various stages within their life cycle. By combining these approaches the causes and effects can be decoupled enabling both aging and failure to be monitored using similar experimental methods in commercial systems in a similar manner to that described in Figure 66.

Lock-in thermography could be used to investigate cells with these induced defect conditions, including selectively depleted anodes and cathodes which will enable the identification of cell parameters for modelling purposes. Both new and aged cells could be investigated to assess the impact of cell degradation on the lock-in technique, with gas generation being a key parameter of interest in these cells. By investigating cells with known defects, characteristic thermal profiles and responses resulting from these faults can be obtained via 2-D temperature maps over a wide frequency range (0.001–10

Hz). By varying the frequency of investigation it is also possible to examine the through-plane response resulting in measurements resolved in all three spatial dimensions. Performing concurrent EIS would enable quantification of the defects electrochemically, whilst *ex situ* CT of the cells could provide both qualitative and quantitative information regarding the changes in the internal micro and macrostructure of the cell.
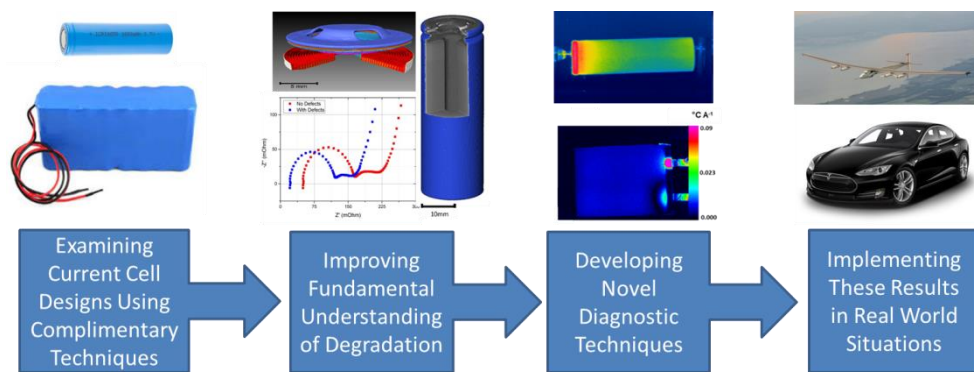
Figure 66 - Proposed mechanism for future direction of Li-ion battery research arising from this work.

Similar to the proposed experiments detailed for SOFCs, the development of LIT has expanded the scope for advanced electrothermal impedance spectroscopy which can determine the state-of-health (SOH) and performance of Li-ion cells *in operando*. Using the thermal profiles obtained via LIT, areas of interest on the surface of the cell can be identified according to the thermal processes and responses that occur within the respective regions. By investigating the response of cells and packs at various points through their life cycles the SOH of the cell can be identified using a

single frequency measurement; in so doing an *in situ* diagnostic of Li-ion cells can be performed *in operando*. Key spatially resolved regions can then be targeted with thermocouples enabling the development of an industrially relevant diagnostic for use in aerospace and automotive applications. To ensure the efficacy of the technique this can be conducted over a range of ambient temperatures relevant to the sectors discussed.

The performance of cells and packs under transient loads can also be further investigated using correlative metrology with a key focus on thermal imaging. Throughout their lifetime, Li-ion battery packs go through extensive rapid charge and discharge processes; by investigating these transients in both the frequency and temporal domains it would be possible to identify the uncertainty in temperature associated with these changes in state-of-charge (SOC). While both the charging and discharging processes will generate heating at the terminals due to Joule heating, the reactions themselves are endothermic during charging (and exothermic during discharge) which can result in a complex temperature profile across the cell. These reactions, which could be investigated using a number of calorimetric techniques, can be quantified enabling improved understanding of the heating mechanisms and thermodynamics within Li-ion cells. In addition, CT can be used to ascribe internal features of the component cells to the thermal gradients and transients observed.

10 List of Acronyms Used

Chapter 1

PEMFC	Polymer electrolyte membrane fuel cell
SOFC	Solid oxide fuel cell
CHP	Combined heat and power
LIB	Lithium ion battery
PAFC	Phosphoric acid fuel cell
AFC	Alkaline fuel cell
MCFC	Molten carbonate fuel cell
HOR	Hydrogen oxidation reaction
ORR	Oxygen reduction reaction
TPB	Triple phase boundary
MEA	Membrane electrode assembly
YSZ	Yttria stabilised zirconia
GDC	Gadolinium doped ceria
IR	Infrared
NIR	Near infrared
CCD	Charged coupled device
NETD	Noise equivalent temperature difference
NEP	Noise equivalent power
PCM	Phase change material
QC	Quality control
PTC	Positive temperature coefficient
FTIR	Fourier transform infrared
LIT	Lock in thermography
CT	Computed tomography
SOH	State of health

Chapter 3

PMMA	Poly(methyl methacrylate)
EIS	Electrochemical impedance spectroscopy

AC	Alternating current
XRD	X-ray diffraction
µCT	Micro-computed tomography
FIB	Focussed ion beam
SEM	Scanning electron microscopy

Chapter 4

EV	Electric vehicles
HEV	Hybrid electric vehicles
OCV	Open circuit voltage

Chapter 5

CTE	Coefficient of thermal expansion
FEA	Finite element analysis
JEEP	Joint engineering, environmental, and processing
PID	Proportional–integral–derivative
SE	Secondary electron

Chapter 6

NDT	Non-destructive testing
FFT	Fast Fourier transform
DAQ	Digital acquisition

Chapter 7

ETIS	Electro-thermal impedance spectroscopy
RMS	Root mean squared
DC	Direct Current

11 Nomenclature

Chapter 1

Symbol	Standard Unit	Description
E	V	Voltage of fuel cell
E_{OCV}	V	Open circuit voltage
E^0	V	Thermodynamic voltage
R	J mol^{-1} K^{-1}	Universal gas constant
T	K	Temperature
$\dot{n}_e$	-	Number of electrons
F	C mol^{-1}	Faraday constant
$a_{products}^{v_i}$	-	Activity of products
$a_{reactants}^{v_i}$	-	Activity of reactants
η_{act}	V	Activation overpotential
η_{ohmic}	V	Ohmic overpotential
η_{conc}	V	Concentration overpotential
α_{rct}	-	Reaction charge transfer coefficient
i	A	Electric current
i_0	A cm^{-1}	Current exchange density
R_{ohm}	Ω	Ohmic resistance
$\tau_{electrolyte}$	m	Thickness of electrolyte
$\sigma_{electrolyte}$	S cm^{-1}	Conductivity of electrolyte
R_{const}	Ω	Constant resistance
l_a	m	Anode thickness
$D_{a(eff)}$	m^2 s^{-1}	Effective diffusivity of anode
p_{H_2}	Pa	Partial pressure of hydrogen
p_{H_2O}	Pa	Partial pressure of water

p_c	Pa	Partial pressure at the cathode
δ_{O_2}	$m^2\,s^{-1}$	Apparent diffusivity of oxygen
p_{O_2}	Pa	Partial pressure of oxygen
Q_{tot}	J	Total heat generated during electrochemical reaction
Q_{rev}	J	Reversible heat generated during electrochemical reaction
Q_{irrev}	J	Irreversible heat generated during electrochemical reaction
$\dot{n}_A$	mol	Number of moles of reactant A
ΔS	$J\,K^{-1}$	Entropy of system
ΔG	$J\,K^{-1}\,mol^{-1}$	Gibbs free energy of system
ΔH	J	Enthalpy of system
E_{op}	V	Operating voltage of electrochemical system
M_v	$W\,m^{-2}$	Radiant flux emitted per unit surface area of blackbody
h	J s	Planck's constant
λ	M	Wavelength of incident radiation
c	$m\,s^{-1}$	Speed of light in a vacuum
k	$J\,K^{-1}$	Boltzman constant
λ_{max}	m	Peak wavelength of incident radiation
T	K	Temperature

J_{Tot}	W	Total radiance
J_A	W	Absorbed radiance
J_R	W	Reflected radiance
J_T	W	Transmitted radiance
α	-	Absorbtivity
ρ	-	Reflectivity
τ	-	Transmittivity
ε	-	Emissivity
ΔE	J	Cutoff energy
ν_{cutoff}	Hz	Cutoff frequency of incident radiation
λ_{cutoff}	µm	Cutoff wavelength of incident radiation
$Z_{radiation}$	W s^{-1} m^{-2}	Quantum flux incident on detector
$\Phi_{radiation}$	s^{-1} m^{-2}	Flux of incident photons on detector
$I_{detector}$	A	Quantum detector current due to incident radiation
C_1	-	Constant
η	%	Quantum efficiency of detector
R_λ^I	A	Wavelength dependent responsivity of detector
NEP_λ	W	Wavelength dependent noise emitted power
E_{photon}	J	Energy of incident photon
Δf	µm	Bandwidth of infrared radiation
$NETD$	W	Noise equivalent temperature distribution
Φ_{det}	W m^{-2}	Radiation incident on detector
τ_{atm}	-	Atmospheric transmitivitty

Symbol	Standard Unit	Description
Φ_{obj}	W	Radiation emitted by object
Φ_{back}	W	Radiation emitted by background objects
Φ_{atm}	W	Radiation emitted by atmosphere

Chapter 3

Symbol	Standard Unit	Description
$\varepsilon_{apparent}$	-	Apparent emissivity
ε_{wall}	-	Emissivity of cavity wall
s	m^2	Surface area of cavity
S_0	m^2	Spherical surface area
Z	Ω	Transfer function response
E	V	Time dependent voltage
I	A	Time dependent current
E_0	V	Magnitude of voltage
I_0	A	Magnitude of current
j	-	Imaginary unit
ω	Hz	Frequency
t	s	Time
ϕ	°	Phase shift
n	-	Integer
λ	m	Wavelength of incident X-rays
d	m	Lattice spacing
θ	°	Angle of incidence of lattice planes

Chapter 4

Symbol	Standard Unit	Description
$\varepsilon_{thermal}$	$m\ m^{-1}$	Thermal strain

Symbol	Standard Unit	Description
L	Å	Lattice parameter length
L_0	Å	Stress free lattice parameter length
$\sigma_{thermal}$	MPa	Thermal stress
E	N m^{-2}	Young's Modulus
Q	J	Heat generated
i	A	Current
R	Ω	Ohmic resistance
ΔT	°C	Differential temperature
C_p	J kg^{-1} K^{-1}	Specific heat capacity
ρ	kg m^{-3}	Material density
dV	m^{-3}	Differential volume
α	m °C^{-1}	Coefficient of thermal expansion

Chapter 5

Symbol	Standard Unit	Description
μ	m	Thermal diffusive length
κ		Thermal conductivity
ρ	kg m^{-3}	Material density
C_p	J kg^{-1} K^{-1}	Specific heat capacity
f	Hz	Frequency of stimulation
A	A	Amplitude of Fourier response
S_n	A	Magnitude of signal at given location
ϕ	°	Phase of Fourier function
$F(u)$	°C	Response signal in Fourier form
$R(u)$	°C	Real component of response signal
$I(u)$	°C	Imaginary component of

		response signal
α	m^2 s^{-1}	Thermal diffusivity

Chapter 6

Symbol	Standard Unit	Description
$i(t)$	A	Input function (time domain)
$a, b, \dots, g$	-	Constants
$r(t)$	°C	Response function (time domain)
$F(s)$	°C A^{-1}	General Laplace domain function
$L[f(t)]$	-	Laplace operator
$Z_{th}(s)$	°C A^{-1}	Transfer function (Laplace domain)
$I(s)$	A	Input function (Laplace domain)
$R(s)$	°C	Response function (Laplace domain)
a_n, b_n	-	Coefficients associated with Laplace transform
$s^0, s^1, \dots s^n$	-	nth order Laplace variables
s	-	Laplace variable
j	-	Imaginary unit
AR	°C A^{-1}	Amplitude ratio
$\Delta\varphi$	°	Phase shift

12 References

1. Mekhilef, S., R. Saidur, and A. Safari, *Comparative study of different fuel cell technologies.* Renewable and Sustainable Energy Reviews, 2012. **16**(1): p. 981-989.

2. Chan, S.H., K.A. Khor, and Z.T. Xia, *A complete polarization model of a solid oxide fuel cell and its sensitivity to the change of cell component thickness.* Journal of Power Sources, 2001. **93**(1-2): p. 130-140.

3. Huijsmans, J.P.P., F.P.F. van Berkel, and G.M. Christie, *Intermediate temperature SOFC – a promise for the 21st century.* Journal of Power Sources, 1998. **71**(1–2): p. 107-110.

4. Kharton, V.V., F.M.B. Marques, and A. Atkinson, *Transport properties of solid oxide electrolyte ceramics: a brief review.* Solid State Ionics, 2004. **174**(1–4): p. 135-149.

5. Spotnitz, R. and J. Franklin, *Abuse behavior of high-power, lithium-ion cells.* Journal of Power Sources, 2003. **113**(1): p. 81-100.

6. Aiken, C.P., et al., *An Apparatus for the Study of In Situ Gas Evolution in Li-Ion Pouch Cells.* Journal of The Electrochemical Society, 2014. **161**(10): p. A1548-A1554.

7. Hammami, A., N. Raymond, and M. Armand, *Lithium-ion batteries: Runaway risk of forming toxic compounds.* Nature, 2003. **424**(6949): p. 635-636.

8. Wang, Q., et al., *Thermal Behavior of Lithiated Graphite with Electrolyte in Lithium-Ion Batteries.* Journal of The Electrochemical Society, 2006. **153**(2): p. A329-A333.

9. Golubkov, A.W., et al., *Thermal-runaway experiments on consumer Li-ion batteries with metal-oxide and olivin-type cathodes.* RSC Advances, 2014. **4**(7): p. 3633-3642.

10. Tobishima, S.-i. and J.-i. Yamaki, *A consideration of lithium cell safety.* Journal of Power Sources, 1999. **81–82**(0): p. 882-886.

11. von Sacken, U., et al., *Comparative thermal stability of carbon intercalation anodes and lithium metal anodes for rechargeable lithium batteries.* Journal of Power Sources, 1995. **54**(2): p. 240-245.

12. O'Hayre, R., et al., *Fuel Cell Fundamentals.* 2 ed. 2006: John Wiley & Sons.

13. O'Hayre, R., D.M. Barnett, and F.B. Prinz, *The triple phase boundary - A mathematical model and experimental*

investigations for fuel cells. Journal of the Electrochemical Society, 2005. **152**(2): p. A439-A444.

14. Chan, S.H. and Z.T. Xia, *Polarization effects in electrolyte/electrode-supported solid oxide fuel cells.* Journal of Applied Electrochemistry, 2002. **32**(3): p. 339-347.

15. Zhang, J. and SpringerLink, *PEM fuel cell electrocatalysts and catalyst layers [Electronic book] : fundamentals and applications.* 2008, London: Springer. 1 online resource (xxi, 1137 p.).

16. Mench, M.M., *Performance Characterization of Fuel Cell Systems*, in *Fuel Cell Engines.* 2008, John Wiley & Sons, Inc. p. 121-190.

17. Costamagna, P., et al., *Electrochemical model of the integrated planar solid oxide fuel cell (IP-SOFC).* Chemical Engineering Journal, 2004. **102**(1): p. 61-69.

18. Leah, R.T., N.P. Brandon, and P. Aguiar, *Modelling of cells, stacks and systems based around metal-supported planar IT-SOFC cells with CGO electrolytes operating at 500-600 degrees C.* Journal of Power Sources, 2005. **145**(2): p. 336-352.

19. Yamamoto, O., et al., *Electrical conductivity of stabilized zirconia with ytterbia and scandia.* Solid State Ionics, 1995. **79**(0): p. 137-142.

20. Virkar, A.V., et al., *The role of electrode microstructure on activation and concentration polarizations in solid oxide fuel cells.* Solid State Ionics, 2000. **131**(1–2): p. 189-198.

21. Shearing, P.R., et al., *Analysis of triple phase contact in Ni-YSZ microstructures using non-destructive X-ray tomography with synchrotron radiation.* Electrochemistry Communications, 2010. **12**(8): p. 1021-1024.

22. Shearing, P.R., et al., *Using Synchrotron X-Ray Nano-CT to Characterize SOFC Electrode Microstructures in Three-Dimensions at Operating Temperature.* Electrochemical and Solid State Letters, 2011. **14**(10): p. B117-B120.

23. Larminie, J. and A. Dicks, *Fuel Cell Systems Explained.* 2 ed. 2003: John Wiley & Sons.

24. Cheng, X., et al., *A review of PEM hydrogen fuel cell contamination: Impacts, mechanisms, and mitigation.* Journal of Power Sources, 2007. **165**(2): p. 739-756.

25. Zhang, J., et al., *High temperature PEM fuel cells.* Journal of Power Sources, 2006. **160**(2): p. 872-891.

26. Li, Q., et al., *High temperature proton exchange membranes based on polybenzimidazoles for fuel cells.* Progress in Polymer Science, 2009. **34**(5): p. 449-477.

27. Energy, U.D.o., *Multi-Year Reseach, Development and Demonstration Plan*, U.D.o. Energy, Editor. 2012.

28. Brett, D.J.L., et al., *Intermediate temperature solid oxide fuel cells.* Chemical Society Revies, 2008(37): p. 1568-1578.

29. Brett, D.J.L., et al., *Methanol as a direct fuel in intermediate temperature (500-600 degrees C) solid oxide fuel cells with copper based anodes.* Chemical Engineering Science, 2005. **60**(21): p. 5649-5662.

30. Verbraeken, M., *Advanced Supporting Anodes for Solid Oxide Fuel Cells.* 2005, University of Twente: Twente.

31. Shao, Z.P. and S.M. Haile, *A high-performance cathode for the next generation of solid-oxide fuel cells.* Nature, 2004. **431**(7005): p. 170-173.

32. Zhu, W.Z. and S.C. Deevi, *Development of interconnect materials for solid oxide fuel cells.* Materials Science and Engineering a-Structural Materials Properties Microstructure and Processing, 2003. **348**(1-2): p. 227-243.

33. Atkins, P., et al., *Inorganic Chemistry.* 4 ed. 2006, Oxford: Oxford University Press.

34. Zeng, Z. and K. Natesan, *Corrosion of metallic interconnects for SOFC in fuel gases.* Solid State Ionics, 2004. **167**(1–2): p. 9-16.

35. Fontana, S., et al., *Metallic interconnects for SOFC: Characterisation of corrosion resistance and conductivity evaluation at operating temperature of differently coated alloys.* Journal of Power Sources, 2007. **171**(2): p. 652-662.

36. Armand, M. and J.M. Tarascon, *Building better batteries.* Nature, 2008. **451**(7179): p. 652-657.

37. Lu, L., et al., *A review on the key issues for lithium-ion battery management in electric vehicles.* Journal of Power Sources, 2013. **226**(0): p. 272-288.

38. Scrosati, B., J. Hassoun, and Y.-K. Sun, *Lithium-ion batteries. A look into the future.* Energy & Environmental Science, 2011. **4**(9): p. 3287-3295.

39. NTSB, *Interim Factual Report DCA13IA037.* 2013.

40. Beauregard, G.P., *Report of Investigation: Hybrids Plus Plug in Hybrid Electric Vehicle.* 2008, U.S. Department of Energy: Idaho National Laboratory.

41. Bandhauer, T.M., S. Garimella, and T.F. Fuller, *A Critical Review of Thermal Issues in Lithium-Ion Batteries.* Journal of the Electrochemical Society, 2011. **158**(3): p. R1-R25.

42. Bazinski, S.J. and X. Wang, *The Influence of Cell Temperature on the Entropic Coefficient of a Lithium Iron Phosphate (LFP) Pouch Cell.* Journal of The Electrochemical Society, 2014. **161**(1): p. A168-A175.

43. Srinivasan, V. and C.Y. Wang, *Analysis of Electrochemical and Thermal Behavior of Li-Ion Cells.* Journal of The Electrochemical Society, 2003. **150**(1): p. A98-A106.

44. Li, Z., et al., *Examining temporal and spatial variations of internal temperature in large-format laminated battery with embedded thermocouples.* Journal of Power Sources, 2013. **241**(0): p. 536-553.

45. Forgez, C., et al., *Thermal modeling of a cylindrical LiFePO4/graphite lithium-ion battery.* Journal of Power Sources, 2010. **195**(9): p. 2961-2968.

46. Richardson, R.R., P.T. Ireland, and D.A. Howey, *Battery internal temperature estimation by combined impedance and surface temperature measurement.* Journal of Power Sources, 2014. **265**(0): p. 254-261.

47. Schmidt, J.P., et al., *Measurement of the internal cell temperature via impedance: Evaluation and application of a new method.* Journal of Power Sources, 2013. **243**(0): p. 110-117.

48. Nieto, N., et al., *Novel thermal management system design methodology for power lithium-ion battery.* Journal of Power Sources, 2014. **272**(0): p. 291-302.

49. Mills, A. and S. Al-Hallaj, *Simulation of passive thermal management system for lithium-ion battery packs.* Journal of Power Sources, 2005. **141**(2): p. 307-315.

50. Ju, H., H. Meng, and C.-Y. Wang, *A single-phase, non-isothermal model for PEM fuel cells.* International Journal of Heat and Mass Transfer, 2005. **48**(7): p. 1303-1315.

51. Vollmer, M. and K.P. Mollmann, *Infrared Thermal Imaging.* 2010: Wiley-VCH.

52. Damm, D.L. and A.G. Fedorov, *Radiation heat transfer in SOFC materials and components.* Journal of Power Sources, 2005. **143**(1–2): p. 158-165.

53. Breitenstein, O. and M. Langenkamp, *Lock-in thermography: Basics and Use for Functional Diagnostics of Electronic Components.* 1 ed. 2003: Springer.

54. Elder, T. and J. Strong, *The infrared transmission of atmospheric windows.* Journal of the Franklin Institute, 1953. **255**(3): p. 189-208.

55. Wood, R.A., C.J. Han, and P.W. Kruse. *Integrated uncooled infrared detector imaging arrays.* in *Solid-State Sensor and Actuator Workshop, 1992. 5th Technical Digest., IEEE.* 1992.

56. Pomfret, M.B., et al., *Thermal imaging of solid oxide fuel cell anode processes.* Journal of Power Sources, 2010. **195**(1): p. 257-262.

57. Saito, T., et al., *A new technique of radiation thermometry using a consumer digital camcorder: Observations of red glow at Aso volcano, Japan.* Earth Planets Space, 2005. **57**: p. e5-e8.

58. Owrutsky, J.C., et al., *Long wavelength video detection of fire in ship compartments.* Fire Safety Journal, 2006. **41**(4): p. 315-320.

59. Almasri, M., X. Bai, and J. Castracane, *Amorphous silicon two-color microbolometer for uncooled IR detection.* Sensors Journal, IEEE, 2006. **6**(2): p. 293-300.

60. Rogalski, A., *Infrared detectors: an overview.* Infrared Physics & Technology, 2002. **43**(3–5): p. 187-210.

61. Laveigne, J., et al., *LWIR NUC using an uncooled microbolometer camera.* Proceedings of the SPIE, Volume 7663, 2010.

62. Maldague, X., *Theory and Practice of Infrared Technology for Nondestructive Testing,* 2001: John Wiley & Sons.

63. Wood, R.A., *Use of vanadium oxide in microbolometer sensors.* 1995, Google Patents.

64. Syllaios, A.J., et al., *Amorphous Silicon Microbolometer Technology.* MRS Online Proceedings Library, 2000. **609**: p. null-null.

65. Rogalski, A., *Recent progress in infrared detector technologies.* Infrared Physics & Technology, 2011. **54**(3): p. 136-154.

66. Eilers, H., *Fabrication, optical transmittance, and hardness of IR-transparent ceramics made from nanophase yttria.* Journal of the European Ceramic Society, 2007. **27**(16): p. 4711-4717.

67. Pazol, B.G., et al., *Development of Sapphire Windows for Use in High-Quality IR Imaging Systems.* Proceedings of SPIE, 1992. **1760**: p. 55-65.

68. Severson, H. and M. Assadi, *Analysis of Residual and Operational Thermal Stresses in a Planar SOFC.* Journal of Fuel Cell Science and Technology, 2013. **10**(6): p. 061001.

69. Al Hallaj, S., J. Prakash, and J.R. Selman, *Characterization of commercial Li-ion batteries using electrochemical–calorimetric measurements.* Journal of Power Sources, 2000. **87**(1–2): p. 186-194.

70. Chen, Y. and J.W. Evans, *Thermal analysis of lithium polymer electrolyte batteries by a two dimensional model—thermal behaviour and design optimization.* Electrochimica Acta, 1994. **39**(4): p. 517-526.

71. Nelson, P., et al., *Modeling thermal management of lithium-ion PNGV batteries.* Journal of Power Sources, 2002. **110**(2): p. 349-356.

72. Mohammadian, S.K. and Y. Zhang, *Thermal management optimization of an air-cooled Li-ion battery module using pin-fin heat sinks for hybrid electric vehicles.* Journal of Power Sources, 2015. **273**: p. 431-439.

73. Park, H., *A design of air flow configuration for cooling lithium ion battery in hybrid electric vehicles.* Journal of Power Sources, 2013. **239**: p. 30-36.

74. Mahamud, R. and C. Park, *Reciprocating air flow for Li-ion battery thermal management to improve temperature uniformity.* Journal of Power Sources, 2011. **196**(13): p. 5685-5696.

75. Hinton, M.L. and D.D. Rivers, *Method and apparatus for cooling and positioning prismatic battery cells*. 2004, Google Patents.

76. Wegner, B., *Prismatic battery made of multiple individual cells*. 2009, Google Patents.

77. Buck, D.S., R.N. Fattig, and B.J. Silk, *Battery pack with integral cooling and bussing devices*. 2009, Google Patents.

78. Mohammadian, S.K., Y.-L. He, and Y. Zhang, *Internal cooling of a lithium-ion battery using electrolyte as coolant through microchannels embedded inside the electrodes.* Journal of Power Sources, 2015. **293**: p. 458-466.

79. Sabbah, R., et al., *Active (air-cooled) vs. passive (phase change material) thermal management of high power lithium-ion packs: Limitation of temperature rise and uniformity of temperature distribution.* Journal of Power Sources, 2008. **182**(2): p. 630-638.

80. Khateeb, S.A., et al., *Design and simulation of a lithium-ion battery with a phase change material thermal management*

system for an electric scooter. Journal of Power Sources, 2004. **128**(2): p. 292-307.

81.	Khateeb, S.A., et al., *Thermal management of Li-ion battery with phase change material for electric scooters: experimental validation.* Journal of Power Sources, 2005. **142**(1–2): p. 345-353.

82.	Kizilel, R., et al., *An alternative cooling system to enhance the safety of Li-ion battery packs.* Journal of Power Sources, 2009. **194**(2): p. 1105-1112.

83.	Karimi, G. and X. Li, *Thermal management of lithium-ion batteries for electric vehicles.* International Journal of Energy Research, 2013. **37**(1): p. 13-24.

84.	Obeisun, O.A., et al., *Study of water accumulation dynamics in the channels of an open-cathode fuel cell through electro-thermal characterisation and droplet visualisation.* International Journal of Hydrogen Energy.

85.	Wu, J., et al., *A review of PEM fuel cell durability: Degradation mechanisms and mitigation strategies.* Journal of Power Sources, 2008. **184**(1): p. 104-119.

86.	Huang, B.T., et al., *Experimental investigation of pinhole effect on MEA/cell aging in PEMFC.* International Journal of Hydrogen Energy, 2013. **38**(1): p. 543-550.

87.	Jao, T.-C., et al., *Diagnosis of PTFE-Nafion MEA degradation modes by an accelerated degradation technique.* International Journal of Energy Research, 2011. **35**(14): p. 1274-1283.

88.	Zhang, S., et al., *A review of accelerated stress tests of MEA durability in PEM fuel cells.* International Journal of Hydrogen Energy, 2009. **34**(1): p. 388-404.

89.	Cappadonia, M., et al., *Conductance of Nafion 117 membranes as a function of temperature and water content.* Solid State Ionics, 1995. **77**: p. 65-69.

90.	Meyer, Q., et al., *Optimisation of air cooled, open-cathode fuel cells: Current of lowest resistance and electro-thermal performance mapping.* Journal of Power Sources, 2015. **291**: p. 261-269.

91.	Schmitz, A., et al., *Planar self-breathing fuel cells.* Journal of Power Sources, 2003. **118**(1–2): p. 162-171.

92.	Jeong, S.U., et al., *Effects of cathode open area and relative humidity on the performance of air-breathing polymer electrolyte membrane fuel cells.* Journal of Power Sources, 2006. **158**(1): p. 348-353.

93.	Bussayajarn, N., et al., *Planar air breathing PEMFC with self-humidifying MEA and open cathode geometry design for*

portable applications. International Journal of Hydrogen Energy, 2009. **34**(18): p. 7761-7767.

94. Meyer, Q., et al., *System-level electro-thermal optimisation of air-cooled open-cathode polymer electrolyte fuel cells: Air blower parasitic load and schemes for dynamic operation.* International Journal of Hydrogen Energy.

95. O'Hayre, R., et al., *Engineering model of a passive planar air breathing fuel cell cathode.* Journal of Power Sources, 2007. **167**(1): p. 118-129.

96. Su, A., et al., *Studies on flooding in PEM fuel cell cathode channels.* International Journal of Hydrogen Energy, 2006. **31**(8): p. 1031-1039.

97. Hussaini, I.S. and C.-Y. Wang, *Visualization and quantification of cathode channel flooding in PEM fuel cells.* Journal of Power Sources, 2009. **187**(2): p. 444-451.

98. Qi, Z. and A. Kaufman, *Improvement of water management by a microporous sublayer for PEM fuel cells.* Journal of Power Sources, 2002. **109**(1): p. 38-46.

99. Obeisun, O.A., et al., *Advanced Diagnostics Applied to a Self-Breathing Fuel Cell.* ECS Transactions, 2014. **61**(27): p. 249-258.

100. Martins, L.S., et al., *The experimental validation of a simplified PEMFC simulation model for design and optimization purposes.* Applied Thermal Engineering, 2009. **29**(14–15): p. 3036-3048.

101. Matian, M., A.J. Marquis, and N.P. Brandon, *Application of thermal imaging to validate a heat transfer model for polymer electrolyte fuel cells.* International Journal of Hydrogen Energy, 2010. **35**(22): p. 12308-12316.

102. Dedigama, I., et al., *In situ diagnostic techniques for characterisation of polymer electrolyte membrane water electrolysers – Flow visualisation and electrochemical impedance spectroscopy.* International Journal of Hydrogen Energy, 2014. **39**(9): p. 4468-4482.

103. Hakenjos, A. and C. Hebling, *Spatially resolved measurement of PEM fuel cells.* Journal of Power Sources, 2005. **145**(2): p. 307-311.

104. Shimoi, R., et al., *Visualization of the Membrane Temperature Field of a Polymer Electrolyte Fuel Cell.* Journal of Energy Resources Technology, 2004. **126**(4): p. 258-261.

105. Guo, H., et al., *Temperature distribution on anodic surface of membrane electrode assembly in proton exchange membrane*

fuel cell with interdigitated flow bed. Journal of Power Sources, 2015. **273**: p. 775-783.

106. Daino, M.M., et al., *Through-Plane Water Transport Visualization in a PEMFC by Visible and Infrared Imaging.* Electrochemical and Solid-State Letters, 2011. **14**(6): p. B51-B54.

107. Kim, U.S., C.B. Shin, and C.S. Kim, *Modeling for the scale-up of a lithium-ion polymer battery.* Journal of Power Sources, 2009. **189**(1): p. 841-846.

108. Kim, U.S., C.B. Shin, and C.S. Kim, *Effect of electrode configuration on the thermal behavior of a lithium-polymer battery.* Journal of Power Sources, 2008. **180**(2): p. 909-916.

109. Wang, Z.J., Z.Q. Li, and Q. Liu, *Infrared Thermography Non-destructive Evaluation of Lithium-ion Battery.* International Symposium on Photoelectronic Detection and Imaging 2011: Advances in Infrared Imaging and Applications, 2011. **8193**.

110. Waldmann, T., et al., *Influence of Cell Design on Temperatures and Temperature Gradients in Lithium-Ion Cells: An In Operando Study.* Journal of The Electrochemical Society, 2015. **162**(6): p. A921-A927.

111. Pesaran, A.A., A. Vlahinos, and S.D. Burch, *Thermal performance of EV and HEV battery modules and packs.* 1997: National Renewable Energy Laboratory.

112. Keyser, M.A., et al., *Thermal evaluation and performance of high-power lithium-ion cells.* 1999: National Renewable Energy Laboratory.

113. Bharathan, D., et al. *Improving battery design with electro-thermal modeling.* in *Vehicle Power and Propulsion, 2005 IEEE Conference.* 2005.

114. Noorkami, M., et al., *Effect of temperature uncertainty on polymer electrolyte fuel cell performance.* International Journal of Hydrogen Energy, 2014. **39**(3): p. 1439–1448.

115. Robinson, J.B., et al., *Detection of Internal Defects in Lithium-Ion Batteries Using Lock-in Thermography.* ECS Electrochemistry Letters, 2015. **4**(9): p. A106-A109.

116. Engebretsen, E., et al., *Electro-thermal impedance spectroscopy applied to an open-cathode polymer electrolyte fuel cell.* Journal of Power Sources, 2015. **In Review**.

117. Pomfret, M.B., D.A. Steinhurst, and J.C. Owrutsky, *Methanol and Ethanol Fuels in Solid Oxide Fuel Cells: A Thermal Imaging Study of Carbon Deposition.* Energy & Fuels, 2011. **25**(6): p. 2633-2642.

118. Pomfret, M.B., D.A. Steinhurst, and J.C. Owrutsky, *Ni/YSZ solid oxide fuel cell anodes operating on humidified ethanol fuel feeds: An optical study.* Journal of Power Sources, 2013. **233**: p. 331-340.

119. Pomfret, M.B., D.A. Steinhurst, and J.C. Owrutsky, *Thermal Imaging of Solid Oxide Fuel Cell Anode Degradation with Dry and Wet Ethanol Fuel Flows.* ECS Transactions, 2011. **35**(1): p. 1563-1570.

120. Pomfret, M.B., D.A. Steinhurst, and J.C. Owrutsky, *Methanol as an Oxygenated SOFC Fuel: An In Situ Optical Analysis of the Fuel Utilization Chemical Mechanism.* ECS Transactions, 2013. **57**(1): p. 2903-2912.

121. Brett, D.J.L., et al., *Application of infrared thermal imaging to the study of pellet solid oxide fuel cells.* Journal of Power Sources, 2007. **166**(1): p. 112-119.

122. Schöttl, S. and D.J.L. Brett, *Applications of Thermal Imaging in Solid Oxide Fuel Cell Research*, in *Engineering and Process Control Department* 2006, Engineering and Process Control Department, National Physical Laboratory.

123. Cumming, D.J. and R.H. Elder, *Thermal imaging of solid oxide cells operating under electrolysis conditions.* Journal of Power Sources, 2015. **280**: p. 387-392.

124. Cumming, D.J., et al., *In-Situ Monitoring of Solid Oxide Electrolysis Cells.* ECS Transactions, 2013. **58**(2): p. 207-216.

125. Hunt, I.A., et al., *Lithium sulfur battery nail penetration test under load.* Journal of Energy Storage, 2015. **2**(0): p. 25-29.

126. Hatchard, T.D., S. Trussler, and J.R. Dahn, *Building a "smart nail" for penetration tests on Li-ion cells.* Journal of Power Sources, 2014. **247**(0): p. 821-823.

127. Doh, C.-H., et al., *Thermal and electrochemical behaviour of C/LixCoO2 cell during safety test.* Journal of Power Sources, 2008. **175**(2): p. 881-885.

128. Kim, U.S., et al., *Modeling the Thermal Behaviors of a Lithium-Ion Battery during Constant-Power Discharge and Charge Operations.* Journal of The Electrochemical Society, 2013. **160**(6): p. A990-A995.

129. Duan, J., et al., *Screening defective lithium ion batteries of 0 V open-circuit voltage by a high current charge process in combination with in situ infrared thermal imaging technology.* Journal of Solid State Electrochemistry, 2012. **16**(2): p. 597-602.

130. Robinson, J.B., et al., *Non-uniform temperature distribution in Li-ion batteries during discharge – A combined thermal*

imaging, X-ray micro-tomography and electrochemical impedance approach. Journal of Power Sources, 2014. **252**: p. 51-57.

131. Finegan, D.P., et al., *In-operando high-speed tomography of lithium-ion batteries during thermal runaway.* Nat Commun, 2015. **6**.

132. Robinson, J.B., et al., *A novel high-temperature furnace for combined in situ synchrotron X-ray diffraction and infrared thermal imaging to investigate the effects of thermal gradients upon the structure of ceramic materials.* Journal of Synchrotron Radiation, 2014. **21**(5).

133. Robinson, J.B., et al., *Thermal Gradients in Solid Oxide Fuel Cell Anodes: X-Ray Diffraction, Thermal Imaging and Model Prediction.* ECS Transactions, 2015. **68**(1): p. 1053-1067.

134. Kirtley, J.D., et al., *In situ optical studies of methane and simulated biogas oxidation on high temperature solid oxide fuel cell anodes.* Physical Chemistry Chemical Physics, 2014. **16**(1): p. 227-236.

135. Eigenbrodt, B.C., et al., *Direct, In Situ Optical Studies of Ni−YSZ Anodes in Solid Oxide Fuel Cells Operating with Methanol and Methane.* The Journal of Physical Chemistry C, 2011. **115**(6): p. 2895-2903.

136. Willmott, P., *Imaging Techniques*, in *An Introduction to Synchrotron Radiation.* 2011, John Wiley & Sons, Ltd. p. 303-337.

137. Winter, M. and R.J. Brodd, *What Are Batteries, Fuel Cells, and Supercapacitors?* Chemical Reviews, 2004. **104**(10): p. 4245-4270.

138. Qiu, X., et al., *Method for Producing Assembled Battery and Assembled Battery.*

139. Venugopal, G., *Characterization of thermal cut-off mechanisms in prismatic lithium-ion batteries.* Journal of Power Sources, 2001. **101**(2): p. 231-237.

140. Pesaran, A.A., G.H. Kim, and K. Smith, *Lithium Mobile Power: Advances in Lithium Battery Technologies for Mobile Applications* 2008, Knowledge Press: Boston.

141. Jhu, C.-Y., et al., *Thermal runaway potential of LiCoO2 and Li(Ni1/3Co1/3Mn1/3)O2 batteries determined with adiabatic calorimetry methodology.* Applied Energy, 2012. **100**: p. 127-131.

142. Ji, Y., Y.C. Zhang, and C.Y. Wang, *Li-Ion Cell Operation at Low Temperatures.* Journal of the Electrochemical Society, 2013. **160**(4): p. A636-A649.

143. Ye, Y., et al., *Electro-thermal modeling and experimental validation for lithium ion battery.* Journal of Power Sources, 2012. **199**(0): p. 227-238.

144. Troxler, Y., et al., *The effect of thermal gradients on the performance of lithium-ion batteries.* Journal of Power Sources, (0).

145. Jiang, F., P. Peng, and Y. Sun, *Thermal analyses of LiFePO4/graphite battery discharge processes.* Journal of Power Sources, 2013. **243**(0): p. 181-194.

146. Yi, J., et al., *Three-Dimensional Thermal Modeling of a Lithium-Ion Battery Considering the Combined Effects of the Electrical and Thermal Contact Resistances between Current Collecting Tab and Lead Wire.* Journal of the Electrochemical Society, 2013. **160**(3): p. A437-A443.

147. Shearing, P.R., et al., *Characterization of the 3-dimensional microstructure of a graphite negative electrode from a Li-ion battery.* Electrochemistry Communications, 2010. **12**(3): p. 374-377.

148. Yufit, V., et al., *Investigation of lithium-ion polymer battery cell failure using X-ray computed tomography.* Electrochemistry Communications, 2011. **13**(6): p. 608-610.

149. Shearing, P.R., et al., *Multi Length Scale Microstructural Investigations of a Commercially Available Li-Ion Battery Electrode.* Journal of the Electrochemical Society, 2012. **159**(7): p. A1023-A1027.

150. Balakrishnan, P.G., R. Ramesh, and T.P. Kumar, *Safety mechanisms in lithium-ion batteries.* Journal of Power Sources, 2006. **155**(2): p. 401-414.

151. Forgez, C., et al., *Thermal modeling of a cylindrical LiFePO4/graphite lithium-ion battery.* Journal of Power Sources, 2010. **195**(9): p. 2961-2968.

152. Zhang, S.S., K. Xu, and T.R. Jow, *Electrochemical impedance study on the low temperature of Li-ion batteries.* Electrochimica Acta, 2004. **49**(7): p. 1057-1061.

153. Nagasubramanian, G., *Two- and three-electrode impedance studies on 18650 Li-ion cells.* Journal of Power Sources, 2000. **87**(1-2): p. 226-229.

154. Zhong, H., et al., *Safe positive temperature coefficient composite cathode for lithium ion battery.* Journal of Power Sources, 2012. **216**: p. 273-280.

155. Mori, M., et al., *Thermal Expansion of Nickel-Zirconia Anodes in Solid Oxide Fuel Cells during Fabrication and Operation.*

Journal of The Electrochemical Society, 1998. **145**(4): p. 1374-1381.

156. Biswas, M., C.S. Kumbhar, and D.S. Gowtam, *Characterization of Nanocrystalline Yttria-Stabilized Zirconia: An In Situ HTXRD Study.* ISRN Nanotechnology, 2011. **2011**.

157. Aruna, S.T., M. Muthuraman, and K.C. Patil, *Synthesis and properties of Ni-YSZ cermet: anode material for solid oxide fuel cells.* Solid State Ionics, 1998. **111**(1–2): p. 45-51.

158. Apfel, H., et al., *Thermal start-up behaviour and thermal management of SOFC's.* Journal of Power Sources, 2006. **154**(2): p. 370-378.

159. Clague, R., A.J. Marquis, and N.P. Brandon, *Finite element and analytical stress analysis of a solid oxide fuel cell.* Journal of Power Sources, 2012. **210**: p. 224-232.

160. Sørensen, B.F., *Thermally Induced Delamination of Symmetrically Graded Multilayers.* Journal of the American Ceramic Society, 2002. **85**(4): p. 858-864.

161. Kumar, A.N. and B.F. Sørensen, *Fracture energy and crack growth in surface treated Yttria stabilized Zirconia for SOFC applications.* Materials Science and Engineering: A, 2002. **333**(1–2): p. 380-389.

162. Nakajo, A., et al., *Simulation of thermal stresses in anode-supported solid oxide fuel cell stacks. Part I: Probability of failure of the cells.* Journal of Power Sources, 2009. **193**(1): p. 203-215.

163. Aguiar, P., C.S. Adjiman, and N.P. Brandon, *Anode-supported intermediate temperature direct internal reforming solid oxide fuel cell. I: model-based steady-state performance.* Journal of Power Sources, 2004. **138**(1–2): p. 120-136.

164. Achenbach, E., *Three-dimensional and time-dependent simulation of a planar solid oxide fuel cell stack.* Journal of Power Sources, 1994. **49**(1–3): p. 333-348.

165. Khaleel, M.A., et al., *A finite element analysis modeling tool for solid oxide fuel cell development: coupled electrochemistry, thermal and flow analysis in MARC®.* Journal of Power Sources, 2004. **130**(1–2): p. 136-148.

166. Morel, B., et al., *Temperature and performance variations along single chamber solid oxide fuel cells.* Journal of Power Sources, 2009. **186**(1): p. 89-95.

167. Leone, P., et al., *Analysis of the thermal field of a seal-less planar solid oxide fuel cell.* Journal of Power Sources, 2012. **204**(0): p. 100-105.

168. Lin, C.K., et al., *Thermal stress analysis of a planar SOFC stack.* Journal of Power Sources, 2007. **164**(1): p. 238-251.

169. Liu, L., G.Y. Kim, and A. Chandra, *Modeling of thermal stresses and lifetime prediction of planar solid oxide fuel cell under thermal cycling conditions.* Journal of Power Sources, 2010. **195**(8): p. 2310-2318.

170. Selimovic, A., et al., *Steady state and transient thermal stress analysis in planar solid oxide fuel cells.* Journal of Power Sources, 2005. **145**(2): p. 463-469.

171. Zhu, W.Z. and S.C. Deevi, *A review on the status of anode materials for solid oxide fuel cells.* Materials Science and Engineering: A, 2003. **362**(1–2): p. 228-239.

172. Majumdar, S., T. Claar, and B. Flandermeyer, *Stress and Fracture Behavior of Monolithic Fuel Cell Tapes.* Journal of the American Ceramic Society, 1986. **69**(8): p. 628-633.

173. Waldbillig, D., A. Wood, and D.G. Ivey, *Thermal analysis of the cyclic reduction and oxidation behaviour of SOFC anodes.* Solid State Ionics, 2005. **176**(9–10): p. 847-859.

174. Sun, B., R.A. Rudkin, and A. Atkinson, *Effect of Thermal Cycling on Residual Stress and Curvature of Anode-Supported SOFCs.* Fuel Cells, 2009. **9**(6): p. 805-813.

175. Villanova, J., et al., *Determination of global and local residual stresses in SOFC by X-ray diffraction.* Nuclear Instruments & Methods in Physics Research Section B-Beam Interactions with Materials and Atoms, 2010. **268**(3-4): p. 282-286.

176. Ishihara, S., et al., *Evaluation of thermal stresses induced in anisotropic material during thermal shock.* Journal of Thermal Stresses, 2002. **25**(7): p. 647-661.

177. Qian, G., T. Nakamura, and C.C. Berndt, *Effects of thermal gradient and residual stresses on thermal barrier coating fracture.* Mechanics of Materials, 1998. **27**(2): p. 91-110.

178. Hutchinson, J.W. and A.G. Evans, *On the delamination of thermal barrier coatings in a thermal gradient.* Surface and Coatings Technology, 2002. **149**(2–3): p. 179-184.

179. Kokini, K., B.D. Choules, and Y.R. Takeuchi, *Thermal fracture mechanisms in ceramic thermal barrier coatings.* Journal of Thermal Spray Technology, 1997. **6**(1): p. 43-49.

180. Villanova, J., et al., *Multiscale measurements of residual strains in a stabilized zirconia layer.* Journal of Applied Crystallography, 2012. **45**: p. 926-935.

181. Sumi, H., et al., *Changes of internal stress in solid-oxide fuel cell during red-ox cycle evaluated by in situ measurement with*

synchrotron radiation. Journal of Fuel Cell Science and Technology, 2006. **3**(1): p. 68-74.

182. Tanaka, K., et al., *In-situ synchrotron measurement of internal stresses in solid-oxide fuel cell during red-ox cycle.* Materials Science Forum, 2008. **571-572**: p. 339-344.

183. Villanova, J., et al., *Multi-scale 3D imaging of absorbing porous materials for solid oxide fuel cells.* Journal of Materials Science, 2014. **49**(16): p. 5626-5634.

184. Wolf, S., N.A. Canas, and K.A. Friedrich, *In Situ X-Ray Diffraction and Stress Analysis of Solid Oxide Fuel Cells.* Fuel Cells, 2013. **13**(3): p. 404-409.

185. Clague, R., et al., *Stress analysis of solid oxide fuel cell anode microstructure reconstructed from focused ion beam tomography.* Journal of Power Sources, 2011. **196**(21): p. 9018-9021.

186. Li, B., et al., *A compact design of a temperature gradient furnace for synchrotron microradiography.* Measurement Science & Technology, 2006. **17**(7): p. 1883-1887.

187. Siddiqui, S.F., et al., *Synchrotron X-ray measurement techniques for thermal barrier coated cylindrical samples under thermal gradients.* Review of Scientific Instruments, 2013. **84**(8): p. 083904.

188. Korsunsky, A.M., et al., *Polycrystal deformation analysis by high energy synchrotron X-ray diffraction on the I12 JEEP beamline at Diamond Light Source.* Materials Letters, 2010. **64**(15): p. 1724-1727.

189. Drakopoulos, M., et al., *I12: the Joint Engineering, Environment and Processing (JEEP) beamline at Diamond Light Source.* J Synchrotron Radiat, 2015. **22**(Pt 3): p. 828-38.

190. Suh, I.-H., H. Ohta, and W. Y., *High-temperature thermal expansion of six metallic elements measured by dilatation method and X-ray diffraction.* Journal of Materials Science, 1988. **23**(2).

191. Pihlatie, M., A. Kaiser, and M. Mogensen, *Mechanical properties of NiO/Ni–YSZ composites depending on temperature, porosity and redox cycling.* Journal of the European Ceramic Society, 2009. **29**(9): p. 1657-1664.

192. *Current Density Distribution in a Solid Oxide Fuel Cell*, in *Solved with COMSOL Multiphysics 5.0.* 2016. p. 1-32.

193. Janardhanan, V.M. and O. Deutschmann, *Numerical study of mass and heat transport in solid-oxide fuel cells running on humidified methane.* Chemical Engineering Science, 2007. **62**(18–20): p. 5473-5486.

194. Yu, J.H., et al., *Microstructural effects on the electrical and mechanical properties of Ni–YSZ cermet for SOFC anode.* Journal of Power Sources, 2007. **163**(2): p. 926-932.

195. Radovic, M. and E. Lara-Curzio, *Mechanical properties of tape cast nickel-based anode materials for solid oxide fuel cells before and after reduction in hydrogen.* Acta Materialia, 2004. **52**(20): p. 5747-5756.

196. Busse, G., D. Wu, and W. Karpen, *Thermal wave imaging with phase sensitive modulated thermography.* Journal of Applied Physics, 1992. **71**.

197. Rosencwaig, A. and A. Gersho, *Theory of the photoacoustic effect with solids.* Journal of Applied Physics, 1976. **47**(1): p. 64-69.

198. Breitenstein, O. and M. Langenkamp, *Lock-In Contact Thermography Investigation of Lateral Electronic Inhomogeneities in Semiconductor Devices.* Sensors and Actuators A, 1998. **71**: p. 46-50.

199. Maldague, X. and S. Marinetti, *Pulse phase infrared thermography.* Journal of Applied Physics, 1996. **79**(5): p. 2694-2698.

200. Breitenstein, O., et al., *Microscopic lock-in thermography investigation of leakage sites in integrated circuits.* Review of Scientific Instruments, 2000. **71**(11): p. 4155-4160.

201. Breitenstein, O., J.P. Rakotoniaina, and M.H.A. Rifai, *Quantitative evaluation of shunts in solar cells by lock-in thermography.* Progress in Photovoltaics: Research and Applications, 2003. **11**(8): p. 515-526.

202. Somasundaram, K., E. Birgersson, and A.S. Mujumdar, *Thermal–electrochemical model for passive thermal management of a spiral-wound lithium-ion battery.* Journal of Power Sources, 2012. **203**(0): p. 84-96.

203. Wu, D. and G. Busse, *Lock-in thermography for nondestructive evaluation of materials.* Revue Générale de Thermique, 1998. **37**(8): p. 693-703.

204. Meola, C., et al., *Non-destructive evaluation of aerospace materials with lock-in thermography.* Engineering Failure Analysis, 2006. **13**(3): p. 380-388.

205. Rakotoniaina, J.P., O. Breitenstein, and M. Langenkamp, *Localization of weak heat sources in electronic devices using highly sensitive lock-in thermography.* Materials Science and Engineering: B, 2002. **91–92**(0): p. 481-485.

206. Breitenstein, O., et al., *Shunts due to laser scribing of solar cells evaluated by highly sensitive lock-in thermography.* Solar Energy Materials and Solar Cells, 2001. **65**(1–4): p. 55-62.

207. Sakagami, T. and S. Kubo, *Applications of pulse heating thermography and lock-in thermography to quantitative nondestructive evaluations.* Infrared Physics & Technology, 2002. **43**(3–5): p. 211-218.

208. Schmidt, J.P., et al., *Investigation of the thermal properties of a Li-ion pouch-cell by electrothermal impedance spectroscopy.* Journal of Power Sources, 2011. **196**(19): p. 8140-8146.

209. Mikolajczak C., K.M., White K., Long R.T.,, *Lithium-Ion Batteries Hazard and Use Assesment.* 2011, The Fire Protection Research Foundation: Massachusetts, USA.

210. Fleckenstein, M., et al., *Thermal Impedance Spectroscopy - A method for the thermal characterization of high power battery cells.* Journal of Power Sources, 2013. **223**: p. 259-267.